Quarterly Technical Report

Solid State Research

1989:1

Lincoln Laboratory

MASSACHUSETTS INSTITUTE OF TECHNOLOGY

LEXINGTON, MASSACHUSETTS

MASSACHUSETTS INSTITUTE OF TECHNOLOGY
LINCOLN LABORATORY

SOLID STATE RESEARCH

QUARTERLY TECHNICAL REPORT

1 NOVEMBER 1988 — 31 JANUARY 1989

ISSUED 18 JULY 1989

LEXINGTON   MASSACHUSETTS

This technical report has been reviewed and is approved for publication.

FOR THE COMMANDER

Hugh L. Southall

Hugh L. Southall, Lt. Col., USAF
Chief, ESD Lincoln Laboratory Project Office

ABSTRACT

This report covers in detail the research work of the Solid State Division at Lincoln Laboratory for the period 1 November 1988 through 31 January 1989. The topics covered are Electrooptical Devices, Quantum Electronics, Materials Research, Submicrometer Technology, Microelectronics, and Analog Device Technology. Funding is provided primarily by the Air Force, with additional support provided by the Army, DARPA, Navy, SDIO, NASA, and DOE.

TABLE OF CONTENTS

LIST OF ILLUSTRATIONS

LIST OF TABLES

INTRODUCTION

1. ELECTROOPTICAL DEVICES

Calculations reveal that, for a fixed input RF power, the maximum response of a lumped-element bandpass electrooptic modulator of the Mach-Zehnder type is limited by the modulator series resistance, not the electrode length (although the response-bandwidth product is increased by using longer electrodes). Experimental devices using transformer coupling show much higher response at the design frequencies than baseband devices, in accordance with theory.

The deposition uniformity in an atmospheric pressure OMVPE chimney reactor, with a sidearm to accommodate susceptor rotation and mechanized substrate loading, was characterized by mapping the thickness uniformity of InP deposited on 5-cm-diam. GaAs substrates. Susceptor rotation improved the thickness uniformity by approximately a factor of 7, with the thickness variation held to less than 3 percent across 4 cm under typical growth conditions.

Interdigitated-electrode p-type $Hg_{0.812}Cd_{0.188}Te$ photoconductors demonstrated 1-GHz bandwidths and heterodyne NEPs better than 8×10^{-19} W/Hz at a local-oscillator power of only 20 μW from a 24.9-μm PbSnSe diode laser. These results are in good agreement with calculations and indicate that, with only modest detector and local-oscillator improvements, sensitivities within a factor of 10 of the $h\nu\Delta f$ limit should be possible.

2. QUANTUM ELECTRONICS

Nd:YAG microchip lasers were piezoelectrically tuned continuously over a 600-MHz range. Tuning rates up to 25 MHz were used, and enhancement of the tuning response due to acoustic resonances was observed.

In a $Ti:Al_2O_3$ laser designed with a large gain region to avoid damage, the output power increases by at least a factor of 4 on cooling from 300 to 77 K. This result is important for mode locking and for long-pulse pumping of high-average-power $Ti:Al_2O_3$ lasers.

Measurements of fluorescence emission spectra, lifetime, absorption, and pump-induced loss were made on $Ti:YAlO_3$ single crystals grown using the unseeded heat-exchanger method. The pump-induced loss is attributed to charge transfer from the 3d excited state of Ti^{3+} to energy levels of unidentified defects.

Gain narrowing in amplified spontaneous emission was analyzed for several emission line shapes. For high peak gain, the narrowing is determined primarily by the curvature of the gain peak.

Optical absorption in $KNbO_3$ from a commercial vendor was measured in the near-infrared and visible. The strength of the absorption is high enough to lower second-harmonic-generation efficiency through phase mismatch induced by the change in refractive index with temperature.

3. MATERIALS RESEARCH

Large-area GaAs/AlGaAs multilayer structures grown by organometallic vapor phase epitaxy were used for the fabrication of high-performance broad-area GRIN-SCH SQW diode lasers with emission wavelengths that fall within the most strongly absorbing pump band of Nd:YAG. The operating characteristics of diode lasers from the same wafer exhibit a high degree of uniformity, and the wafer-to-wafer reproducibility is excellent for devices fabricated from structures grown under the same nominal conditions.

Thermal imaging with silicide Schottky-barrier detector arrays was extended for the first time into the long-wavelength infrared spectral band (8 to 14 μm). High-quality imagery with a minimum resolvable temperature of ~0.3 K was obtained by operation at 50 K of monolithically integrated 128×128-element arrays consisting of IrSi detectors with a cutoff wavelength of ~9.4 μm and surface-channel CCD readout circuitry.

4. SUBMICROMETER TECHNOLOGY

Amorphous carbon films to be used as 193-nm-imaging or planarizing layers were plasma-deposited under various conditions. The sensitivity to 193-nm radiation and the resistance of the films to oxygen reactive-ion etching could be tailored by varying the deposition conditions.

Laser cutting and laser direct-writing of doped polysilicon were used to make design modifications to fully fabricated digital CMOS integrated circuits. Several circuits were modified, shortening the chip design process by several months in each instance.

5. MICROELECTRONICS

Two-dimensional device simulations of Si PBTs indicated that new doping profiles should result in greatly improved high-frequency, high-voltage operation. A device structure with high emitter and low collector doping results in a factor-of-2 improvement in the f_T-breakdown-voltage product compared with a uniformly doped device.

A unique measurement system was developed to characterize the large-signal performance of transistors in the 33- to 50-GHz frequency band. The system, which uses an active load-pull concept to electronically vary the output load impedance of a transistor and measure its associated output power, efficiency, and gain, has been applied to the characterization of GaAs permeable-base transistors.

Bias stress testing of Al-gate MOS structures at 300°C revealed a negative bias-temperature instability (NBTI) in the capacitance-voltage characteristics for oxides grown in a new cantilever-based furnace bank. Linear modeling techniques were used to efficiently find (in just 19 experiments) the values of the process variables that minimized NBTI, resulting in the latter's reduction by a factor of 3, and to indicate directions for further improvements.

6. ANALOG DEVICE TECHNOLOGY

Thin superconducting films of $YBa_2Cu_3O_x$ were patterned by standard photolithographic techniques using both positive and negative photoresists, followed by ion milling in an Ar^+ beam. As a result of this process, the transition temperature of these patterned lines (with widths in the range of 10 to 100 μm) was lowered by 5 to 10 K.

Further measurements of residual noise in superconductive niobium stripline resonators as a function of loaded Q revealed that their $1/f$ noise is higher than that of acoustic resonators at the same frequency. The phase noise of oscillators stabilized with these niobium resonators was measured and agrees with the Leeson feedback model within ± 3 dB.

A second generation of a four-channel, 128-sample, 64-tap analog-ternary correlator was designed, fabricated, and tested. The dynamic range was measured to be 60 dB at a sample rate of 40 Ms/s, the nonlinearity reduced to below 0.4 percent for a full-scale input, and the output offset reduced to $\leqslant$40 mV (which is $\leqslant$2 percent of the output range).

REPORTS ON SOLID STATE RESEARCH

1 November 1988 Through 31 January 1989

PUBLISHED REPORTS

Journal Articles

JA No.

6075	Semiconductor Integrated Optic Devices	F.J. Leonberger* J.P. Donnelly	In *Guided-Wave Opto-electronics*, Springer Series in Electronics and Photonics, Vol. 26, T. Tamir, Ed. (Springer-Verlag, New York, 1988)
6083	RF Surface Resistance of Y-Ba-Cu-O Thin Films	M.S. DiIorio* A.C. Anderson B-Y. Tsaur	Phys. Rev. B **38**, 7019 (1988)
6095	Short-Channel Effect in Fully Depleted SOI MOSFET's	K.K. Young	IEEE Trans. Electron Devices **ED-36**, 399 (1989)
6100A	Oscillators Using Magnetostatic-Wave Active Tapped Delay Lines	C.L. Chen A. Chu* L.J. Mahoney W.E. Courtney R.A. Murphy J.C. Sethares*	IEEE Trans. Microwave Theory Tech. **MTT-37**, 239 (1989)
6123	Growth of Beam Perturbations by Stimulated Light by Light Scattering in the Atmosphere	P.L. Kelley J.-P.E. Taran*	Appl. Opt. **27**, 4787 (1988)
6149	Effect of Finite Lower Level Lifetime on Q-Switched Lasers	T.Y. Fan	IEEE J. Quantum Electron. **QE-24**, 2345 (1988)
6158	IrSi Schottky-Barrier Infrared Detectors with 10-μm Cutoff Wavelength	B-Y. Tsaur M.M. Weeks* R. Trubiano* P.W. Pellegrini* T-R. Yew*	IEEE Electron Device Lett. **EDL-9**, 650 (1988)

---

* Author not at Lincoln Laboratory.

---

* Author not at Lincoln Laboratory.

*   *   *   *   *

UNPUBLISHED REPORTS

Journal Articles

---

* Author not at Lincoln Laboratory.

Meeting Speeches*

---

* Titles of Meeting Speeches are listed for information only. No copies are available for distribution.

† Author not at Lincoln Laboratory.

7965	Analog Nonvolatile Memory for Neural Network Implementations	J.P. Sage R.S. Withers K.E. Thompson	174th Meeting, The Electrochemical Society, Chicago, Illinois, 9-14 October 1988
8012	Fabrication of Microlenses in InP and GaP by Mass Transport	Z.L. Liau V. Diadiuk J.N. Walpole D.E. Mull	
8023	ArF Laser Induced Growth of Transparent Conductive SnO_2	R.R. Kunz M. Rothschild D.J. Ehrlich	
8035	An *In Situ* Study of UV Photo-chemistry of Adsorbed and Gaseous $TiCl_4$ FTIR Spectroscopy	P.V. Purohit M. Rothschild D.J. Ehrlich	
8036	Plasma-Activated Ion Beam Reactive Sputtering of NbN Thin Films	D.J. Lichtenwalner A.C. Anderson D.A. Rudman*	Fall 1988 Materials Research Society Symposium, Boston, 28 November — 1 December 1988
8059	Some Applications of Ion Beams in III-V Compound Semi-conductor Device Fabrication	J.P. Donnelly K.K. Anderson J.D. Woodhouse W.D. Goodhue D. Yap M.C. Gaidis C.A. Wang	
8151A	Subboundary-Free Silicon-on-Insulator Thin Films by Zone-Melting Recrystallization with Enhanced Radiative Heating	C.K. Chen J.S. Im	
8017A	Analog Signal Processing with Superconductive Devices	R.S. Withers	Sigma XI, The Scientific Research Society, Hanscom Air Force Base, Bedford, Massachusetts, 22 December 1988
8017B	Analog Signal Processing with Superconductive Devices	R.W. Ralston	SERI Conference on the Science and Technology of Thin Film Superconductors, Colorado Springs, Colorado, 15 November 1988

* Author not at Lincoln Laboratory.

* Author not at Lincoln Laboratory.

MS No.

8178	High-Temperature Furnaces for Crystal Growth	R.E. Fahey	Fundamentals of Vacuum Technology, Boston, 9-10 November 1988
8185	Progress in Diode Pumped Solid State Lasers	T.Y. Fan	Seminar, IEEE Lasers and Electro-Optics Society, Boston Chapter, GTE Laboratories, Waltham, Massachusetts, 12 January 1989
8216	Integrated Optical Modulators for Analog Links	L.M. Johnson G.E. Betts	Military Fiber Optics Conference, Los Angeles, California, 7 December 1988
8244	OMVPE Growth of AlGaAs Using an ATM Filter	C.A. Wang	Gas Purification Symposium, Boston, 1 December 1988
8245	Microwave Semiconductor Device Research at Lincoln Laboratory	R.A. Murphy	Seminar, University of Massachusetts, Amherst, 30 November 1988
8256	Research on InP Devices at Lincoln Laboratory	A.R. Calawa C.L. Chen J.D. Woodhouse S.C. Palmateer G.W. Iseler S.H. Groves W.E. Courtney J.P. Donnelly	Office of Naval Research Workshop on InP Devices, LaJolla, California, 25-26 January 1989
8286	CCD Imager Development at Lincoln Laboratory	B.E. Burke	Seminar, Jet Propulsion Laboratory, Pasadena, California, 19 January 1989

ORGANIZATION

SOLID STATE DIVISION

A.L. McWhorter, *Head*
I. Melngailis, *Associate Head*
E. Stern, *Associate Head*
J.F. Goodwin, *Assistant*

N.L. DeMeo, Jr., *Associate Staff*

SUBMICROMETER TECHNOLOGY

D.J. Ehrlich, *Leader*
D.C. Shaver, *Assistant Leader*

Astolfi, D.K.	Kunz, R.R.
Black, J.G.	Lyszczarz, T.M.
Dennis, C.L.	Maki, P.A.
Doran, S.P.	Melngailis, J.†
Efremow, N.N., Jr.	Pang, S.W.
Forte, A.R.	Rooks, M.J.
Gajar, S.A.*	Rothschild, M.
Geis, M.W.	Sedlacek, J.H.C.
Hartney, M.A.	Uttaro, R.S.
Horn, M.W.	Young, K.K.

QUANTUM ELECTRONICS

A. Mooradian, *Leader*
P.L. Kelley, *Associate Leader*
A. Sanchez-Rubio, *Assistant Leader*

Aggarwal, R.L.	Lacovara, P.
Barch, W.E.	Le, H.Q.
Belanger, L.J.	Menyuk, N.†
Daneu, V.	Ochoa, J.R.
DeFeo, W.E.	Schulz, P.A.
Fan, T.Y.	Seppala, J.P.
Hancock, R.C.	Sharfin, W.F.
Henion, S.R.	Sullivan, D.J.
Hotaling, T.C.	Tapper, R.S.
Jeys, T.H.	Wall, K.F.
Korn, J.A.	Zayhowski, J.J.

ELECTRONIC MATERIALS

A.J. Strauss, *Leader*
B-Y. Tsaur, *Associate Leader*
H.J. Zeiger, *Senior Staff*

Anderson, C.H., Jr.	Eglash, S.J.	Mastromattei, E.L.
Button, M.J.	Fahey, R.E.	Mattia, J.P.
Chen, C.K.	Finn, M.C.	Nitishin, P.M.
Choi, H.K.	Im, J.S.*	Pantano, J.V.
Clark, H.R., Jr.	Iseler, G.W.	Tracy, D.M.
Connors, M.K.	Kolesar, D.F.	Turner, G.W.
Delaney, E.J.	Krohn, L., Jr.	Wang, C.A.

---

* Research Assistant
† Part Time

xxv

APPLIED PHYSICS

R.C. Williamson, *Leader*
D.L. Spears, *Assistant Leader*
R.H. Rediker, *Senior Staff*

Aull, B.F.
Bailey, R.J.
Betts, G.E.
Bossi, D.E.*
Corcoran, C.J.*
Cox, C.H., III
Diadiuk, V.
Donnelly, J.P.
Ferrante, G.A.
Groves, S.H.
Harman, T.C.
Hovey, D.L.
Johnson, L.M.
Liau, Z.L.
Lind, T.A.

Missaggia, L.J.
Mull, D.E.
O'Donnell, F.J.
Palmacci, S.T.
Palmateer, S.C.
Pang, L.Y.*
Rauschenbach, K.
Reeder, R.E.
Roussell, H.V.
Shiple, S.D.*
Tsang, D.Z.
Walpole, J.N.
Woodhouse, J.D.
Yee, A.C.

ANALOG DEVICE TECHNOLOGY

R.W. Ralston, *Leader*
R.S. Withers, *Associate Leader*
R.M. Lerner, *Senior Staff†*

Anderson, A.C.
Arsenault, D.R.
Bhushan, M.
Boisvert, R.R.
Brogan, W.T.
Connelly, D.J.*
Denneno, A.P.
Fitch, G.L.
Green, J.B.
Hamm, J.M.
Holtham, J.H.

Lattes, A.L.
Lichtenwalner, D.J.*
Macedo, E.M., Jr.
Munroe, S.C.
Oates, D.E.
Sage, J.P.
Seidel, M.N.*
Slattery, R.L.
Thompson, K.E.
Yu-Jahnes, L-S.*

MICROELECTRONICS

R.A. Murphy, *Leader*
E.D. Savoye, *Associate Leader*
B.B. Kosicki, *Assistant Leader*
R.W. Chick, *Senior Staff*

Actis, R.
Bales, J.W.*
Bennett, P.C.
Bozler, C.O.
Brown, E.R.
Burke, B.E.
Calawa, A.R.
Chen, C.L.
Chiang, A.M.
Chuang, M.L.*
Clifton, B.J.
Daniels, P.J.
Doherty, C.L., Jr.
Dolat, V.S.
Durant, G.L.

Felton, B.J.
Gladden, D.B.‡
Goodhue, W.D.
Gray, R.V.
Gregory, J.A.
Hollis, M.A.
Huang, J.C.M.
Johnson, B.W.
Johnson, K.F.
LaFranchise, J.R.
Lincoln, G.A., Jr.
Mahoney, L.J.
Manfra, M.J.
Mathews, R.H.

McGonagle, W.H.
McIntosh, K.A.
Mountain, R.W.
Nichols, K.B.
Parker, C.D.
Pichler, H.H.
Rabe, S.
Rathman, D.D.
Reich, R.K.
Reinold, J.H., Jr.
Smith, F.W.*
Sollner, T.C.L.G.
Vera, A.
Wilde, R.E.

---

* Research Assistant
† Part Time
‡ Staff Associate

xxvi

1. ELECTROOPTICAL DEVICES

1.1 HIGH-SENSITIVITY LUMPED-ELEMENT BANDPASS MODULATORS IN LiNbO$_3$

We have theoretically investigated and experimentally demonstrated high-sensitivity electrooptic waveguide modulators for use in applications that do not require a dc response (for example, bandpass analog optical links). Most prior integrated-optical modulators have been designed for baseband applications, such as digital communication. The modulators developed here are conventional lithium niobate interferometric modulators[1] with a bandpass impedance-matching circuit that gives high response over a particular frequency band. This technique uses discrete circuit elements and treats the modulator electrodes as a lumped-element capacitor.[2] The maximum response of the impedance-matched modulator is found to be limited by the resistance in series with the electrode, not by the modulator length (as is the case for the usual baseband modulator).

In the Mach-Zehnder interferometric modulator, the electric field from the modulator electrodes produces an optical phase difference ϕ between the interferometer arms. The conversion between the voltage V applied to the modulator and the phase difference is characterized by V_π, where $\phi = \pi V / V_\pi$. For a fixed waveguide and electrode cross section, the voltage-length product $V_\pi L$ and the modulator capacitance per unit length C/L are constants independent of electrode length L. Therefore, we can define a length-independent switching charge

$$q_\pi \equiv CV_\pi = \left(\frac{C}{L}\right)(V_\pi L) \tag{1-1}$$

and express the phase difference by

$$\phi = \pi q / q_\pi \quad . \tag{1-2}$$

In the sinusoidal steady-state case, the charge and the phase difference vary with time as

$$q = q_B + \frac{i_m}{\omega} \sin \omega t \tag{1-3}$$

and

$$\phi = \frac{\pi}{2} + \phi_m \sin \omega t \quad , \tag{1-4}$$

where we have taken the dc bias value of ϕ to be $\pi/2$ for maximum ac response, and where $q_B = q_\pi/2$ is the dc bias charge on the electrodes. Note that expressing the charge in terms of the peak current i_m introduces an inverse frequency dependence. From this, we see that the phase modulation depth

$$\phi_m = \frac{\pi i_m}{\omega q_\pi} \tag{1-5}$$

1

depends upon the current through the modulator electrodes, but is otherwise independent of modulator length.

The modulator equivalent circuit can be approximated by a series RLC circuit; the series resistance and the modulator capacitance are of primary concern here. The equivalent series resistance R_m is given by a combination of electrode series resistance, contact resistance and resistance caused by acoustic-wave launching,[3] as well as any series resistance intentionally placed in the circuit to broaden the bandwidth. The maximum current possible for a particular input RF power P_s occurs when all of the input power is dissipated in the resistance R_m and is given by

$$i_m{}^2 = 2P_s/R_m. \tag{1-6}$$

The figure of merit for the response of the modulator, $K = \phi_m^2/P_s$, is the modulation depth squared per unit input power (generally from a 50-Ω source). In the above optimum case

$$K = \frac{2\pi^2}{\omega^2 R_m q_\pi^2} \quad , \tag{1-7}$$

which is the maximum K obtainable from a lumped-element interferometric modulator. Since our basic modulator parameter q_π is solely a function of cross-sectional geometry, K is independent of electrode length, except for any dependence that may occur in R_m. Note that the maximum response is inversely proportional to frequency squared. Generally, the impedance-matching circuit will also be frequency dependent. K will have the optimum value given in Equation (1-7) only at frequencies where all the input power is dissipated in R_m.

The specific impedance-matching circuit we used was a loosely coupled double-tuned transformer, as shown in Figure 1-1(a). The transformer secondary inductance and the modulator capacitance form a resonant circuit. With appropriate values for the coupling coefficient k and C_2, this transformer circuit meets the requirement of transferring all the input power from a 50-Ω source to the series resistance R_m at the resonant frequency ω_0. For comparison, Figure 1-1(b) shows the traditional resistive impedance match, which we refer to as the "baseband" match.

Figure 1-2 shows the calculated response of the transformer-coupled modulator for various modulator lengths. The series resistance R_m is constant here, but k and C_2 are adjusted to maintain an impedance match at 100 MHz. As expected from Equation (1-7), the response at 100 MHz is constant. The bandwidth increases as the length increases because the bandwidth B is inversely proportional to the Q of the secondary resonant circuit, which depends on the capacitance and therefore the length of the modulator. If the length is held constant, the bandwidth and peak response can be traded off by varying R_m, as in any resonant circuit. The response-bandwidth product

$$KB = \frac{2\pi C}{q_\pi^2} \tag{1-8}$$

2
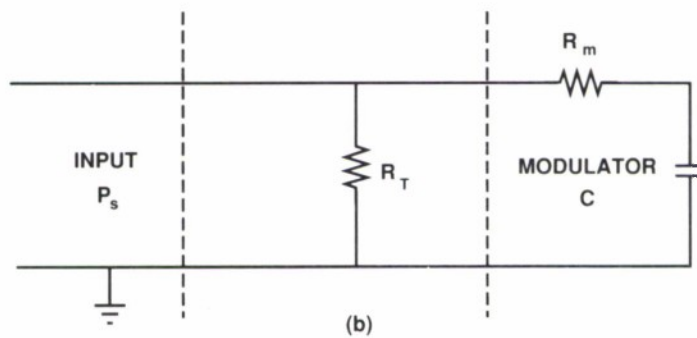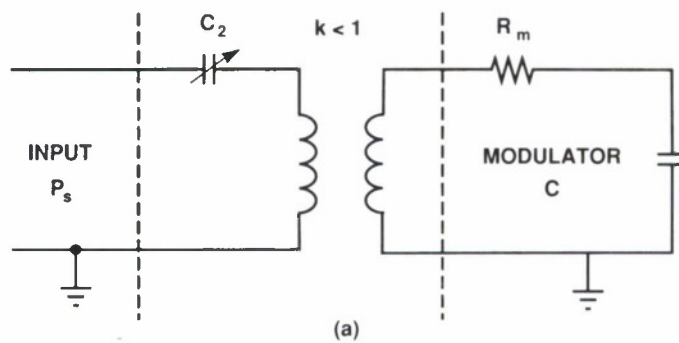
Figure 1-1.   *Waveguide modulator impedance-matching circuits using (a) transformer matching where k is the transformer coupling coefficient, and (b) baseband resistive matching, where R_T is equal to the characteristic impedance of the input. Typically $R_T = 50\ \Omega$ and usually $R_m \ll R_T$*

3
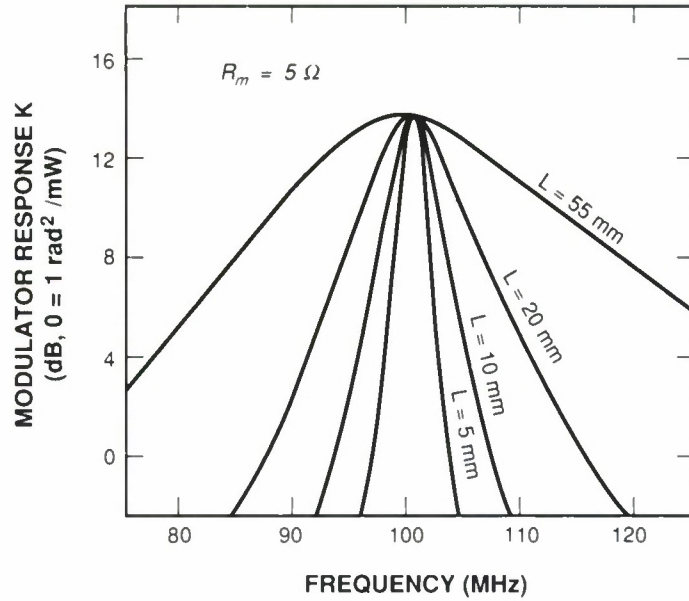
Figure 1-2. Theoretically calculated response of the transformer-matched modulator for various electrode lengths, using a capacitance per unit length of 0.6 pF/mm and a $V_\pi L$ product of 36 V-mm (so q_π = 21.6 pC). The series resistance is the same for all curves.

is independent of R_m and ω_o, but does depend on modulator length through the capacitance C. Therefore, while the peak modulator response is independent of electrode length, the bandwidth (and thus the response-bandwidth product) is improved by using longer electrodes. To design a transformer-coupled modulator, one would maximize the KB product by choosing the maximum length allowed by packaging or substrate constraints, then use R_m to trade off response and bandwidth as needed. The KB product of the transformer-coupled device is about twice as large as that of the baseband device. In applications where the required bandwidth is smaller than an octave, the transformer-coupled device can be designed to have a much higher peak response by using only the needed bandwidth.

Experimental devices were built on X-cut lithium niobate using Ti-indiffused waveguides for operation at the 1.3-μm optical wavelength. The interferometric modulators used in these tests had $V_\pi L$ products of 36 to 49 V-mm and a capacitance per unit length of 0.7 pF/mm; this resulted in switching charges q_π of 25 to 34 pC. Figure 1-3 shows the response of a 13.5-mm-long modulator with both transformer and baseband matching. The transformer match gives a response of $\sim$ 4 rad^2/mW, which is 15 dB higher than the baseband match at 150 MHz. This illustrates the large improvement in peak response that can be obtained from a device of limited length by using transformer coupling to trade off bandwidth for sensitivity. We also tested a 55-mm-long modulator with the transformer tuned to 31 MHz and achieved a peak response K of 30 rad^2/mW. This demonstrates the extremely high peak response obtainable at low frequencies. The response is equivalent to that of a 50-Ω baseband device with V_π of only 180 mV. Note

4
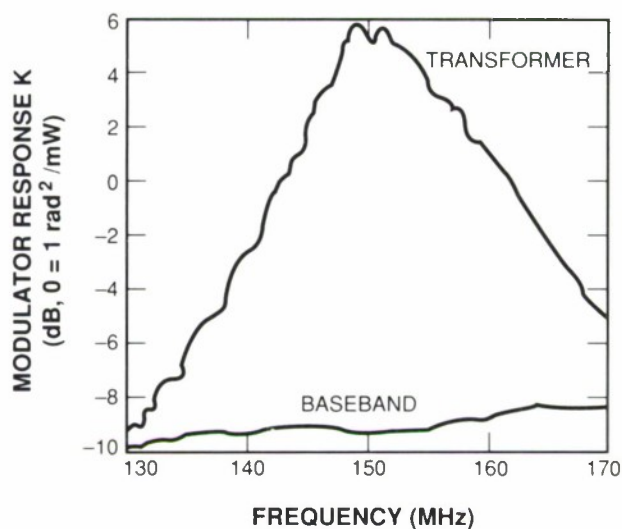
Figure 1-3. Frequency response of a 13.5-mm-long modulator using both transformer and baseband matching.

that the equivalent V_π is given by $(2\pi^2 R_T/K)^{1/2}$, where R_T is the characteristic impedance as shown in Figure 1-1(b). No series resistance was intentionally added to these experimental modulators; the response measured was the maximum we could obtain. The primary contribution to R_m at low frequencies, and thus the primary limitation on response, seems to be the launching of acoustic waves by the modulator electrodes.

We have shown the limits of lumped-element modulator performance with a bandpass drive circuit. Response and bandwidth can be traded off, and a large improvement over the response of a baseband device can be achieved if the bandwidth is substantially decreased. This technique is not restricted to the transformer circuit used here; other passive circuits can be designed for different shape passbands (although the peak response cannot be improved beyond the limit derived here).

<div align="right">

G.E. Betts   C.H. Cox, III

L.M. Johnson   K.G. Ray

</div>

1.2 LARGE-AREA UNIFORM DEPOSITION OF InP BY OMVPE

For most applications it is not sufficient for an organometallic vapor phase epitaxy (OMVPE) reactor to produce epitaxial layers with state-of-the-art purity and heterointerface abruptness; the layers must also have a thickness and doping uniformity of a few percent across large areas. Generally, to achieve uniform deposition, the thickness of the boundary layer at the substrate must be uniform so that the deposition rate is the same at all points on the wafer. Based on flow visualization and tracer gas studies of various OMVPE reactor geometries,[4,5] we

5

chose to use a parallel-flow reduced-cross-section chimney design, which has distinct advantages for the growth of InP compounds.[6] The small cross section allows atmospheric pressure operation, which is operationally simple and reduces hydride source usage compared with low-pressure growth.[7] Two consequences of the parallel-flow geometry are a boundary layer thickness that increases with distance from the leading edge of the susceptor and potential source depletion with distance, both giving rise to a decreased growth rate along the flow direction. We have used susceptor rotation to time-average these nonuniform growth rates and have achieved reproducible maximum thickness variations of < 3 percent across 4 cm under typical growth conditions.

Figure 1-4 shows a schematic of the chimney reactor which has a sidearm added for susceptor rotation and mechanized substrate loading.[6] The body of the reactor is constructed of high-aspect-ratio (depth/width ~8) rectangular fused silica tubing which permits growth on 5-cm-diam. wafers with relatively high average gas velocities (16 cm/s) at modest flow rates of ~7 slpm. A 5-cm-diam. wafer is held on a molybdenum susceptor with molybdenum clips and screws. Flow visualization studies and growth characterization have shown that under a wide variety of conditions, the flow in this reactor is free of vortices and convection cells, and that it is possible to select susceptor rotation rates that are high enough for growth averaging, but low enough not to disturb the laminar flow.[5]
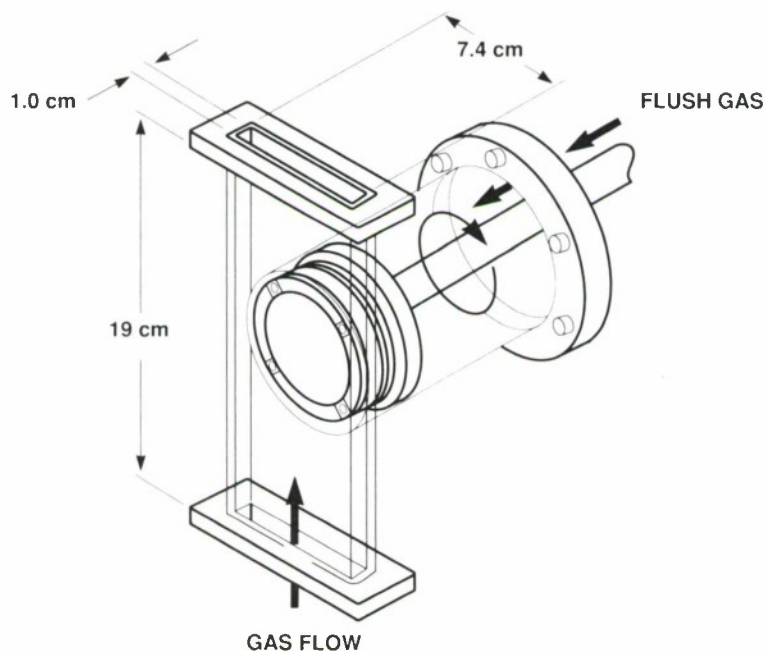
Figure 1-4. Schematic drawing of the sidearm chimney reactor.

A technique involving the growth of InP on 5-cm-diam. GaAs substrates has been used to evaluate deposition uniformity and has been previously described in detail.[6,8,9] This technique takes advantage of the low cost of GaAs substrates, compared with that of InP, and of the chemical etching differences between GaAs and InP. After epilayer growth, the wafer is patterned using photolithography and selective etching, and numerous InP layer thickness measurements are made using a surface profilometer. A previous study with a nonrotating susceptor[6] established the ranges of carrier gas flows and source concentrations that minimize leading-to-trailing-edge thickness variations. With an H_2 carrier gas at flow rates of 7 slpm and an H_2 sidearm flush of 1 slpm, a thickness variation of ~20 percent across 4 cm was obtained without susceptor rotation. Figure 1-5 shows the measured leading-to-trailing-edge thickness pattern along the central axis of the wafer. This same leading-to-trailing-edge pattern is observed for deposition away from the central axis. (Here, the leading edge of the circular susceptor is displaced downstream.)

Figures 1-6 and 1-7 show thickness uniformity data with susceptor rotation, and here, the maximum variations are typically only 3 percent across 4 cm. As can be seen in Figures 1-6(a-d), at an H_2 flow rate of 7 slpm the thickness uniformity is essentially independent of susceptor rotation from 3 to 120 rpm. This invariance of the deposition pattern to rotation rate is interpreted
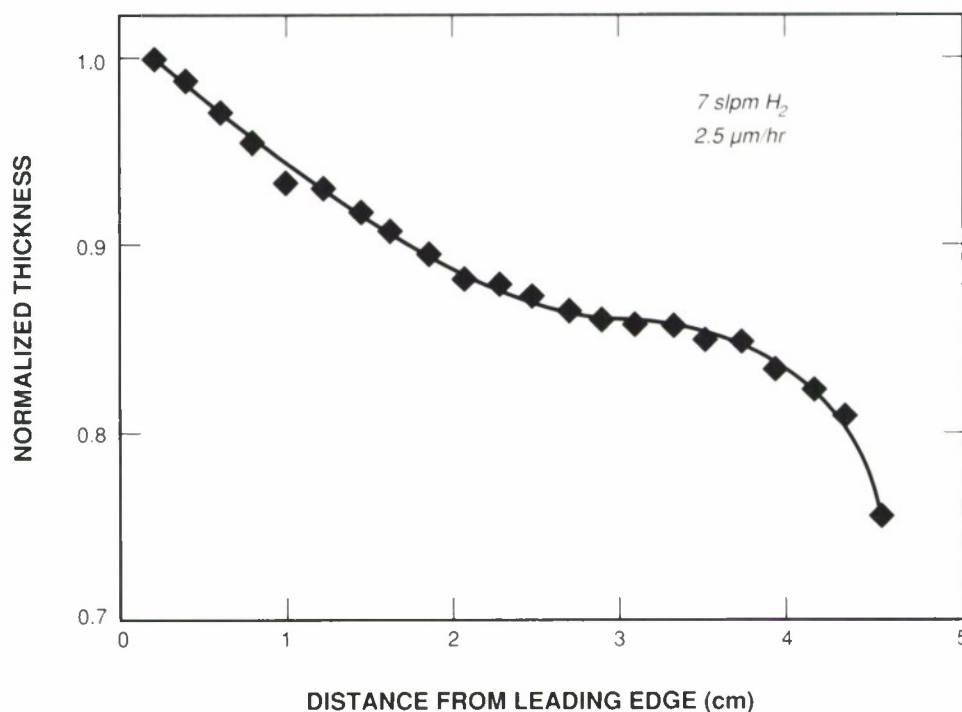
Figure 1-5. InP layer thickness vs position along the flow direction for 7-slpm total flow without susceptor rotation. The solid curve is a smooth curve drawn through the data. The wafer surface was recessed 0.64 mm below the susceptor face.

7
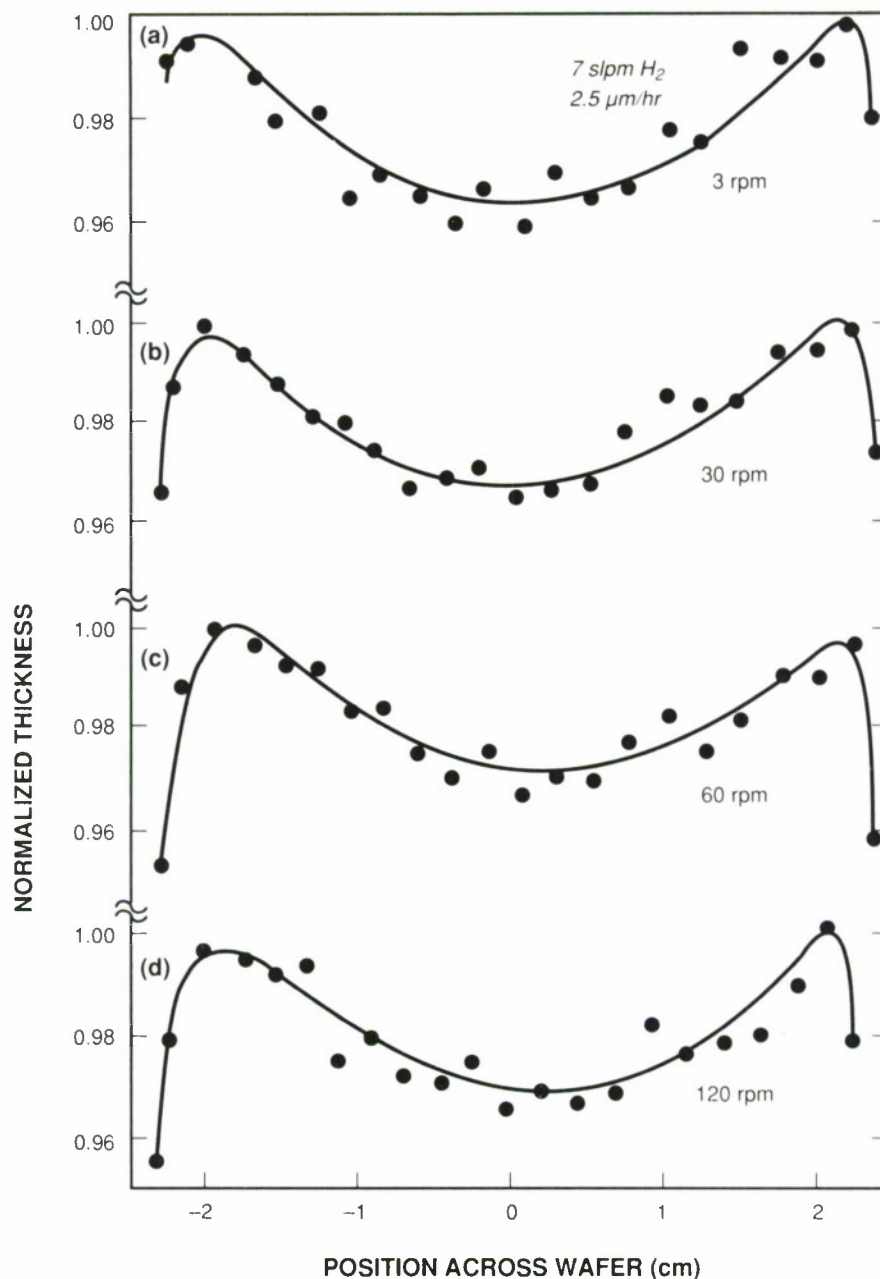
Figure 1-6.   In P layer thickness vs position across the 5-cm-diam. wafers for susceptor rotation rates of (a) 3 rpm, (b) 30 rpm, (c) 60 rpm and (d) 120 rpm. In all cases the wafer surfaces were recessed 0.64 mm below the susceptor surface. The solid curves are simply smooth curves drawn through the experimental data.

8
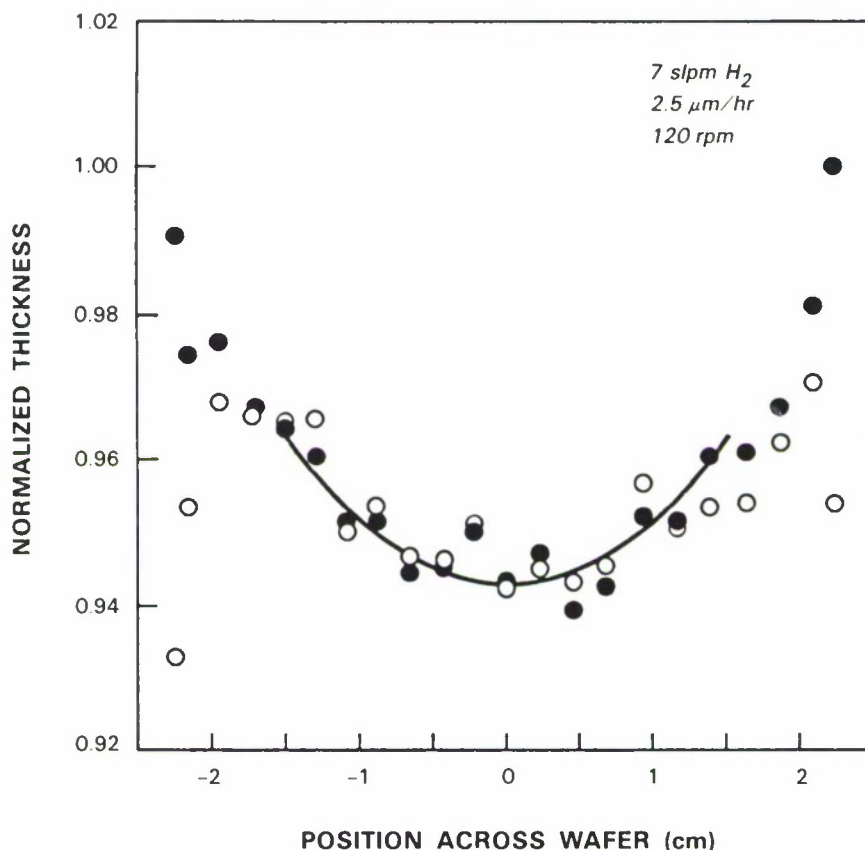
Figure 1-7. InP layer thickness vs position at a rotation rate of 120 rpm for wafer recesses of 0.64 mm (open circles) and 0.25 mm (solid circles). The solid curve is a circular average of the nonrotation growth data, as shown in Figure 1-5.

as corroborating the existence of a slow-rotation regime (observed in an earlier flow visualization study) where rotation does not disturb the gas flow when the tangential velocity of the susceptor is less than the average gas velocity through the growth tube. In a low-rotation-rate regime, where the thickness uniformity is independent of rotation rate, the deposition pattern with rotation should be predictable from a circular average of the nonrotation pattern. A circular average of the nonrotation curve from 1 to 4 cm (Figure 1- 5) produces the solid curve shown in Figure 1-7, which is seen to give a reasonable fit to the measured data in the central region of the substrate. The deposition rate near the edges of the wafer can be altered by adjusting the height of the wafer in the susceptor recess. Figure 1-7 shows the thickness profiles for a wafer normally 0.64 mm below the susceptor surface (open circles) and for a wafer 0.25 mm below the susceptor surface (closed circles). For the latter case, the thickness at the edges continues to increase in agreement with a circular average of the nonrotation data. In the former case, the thickness is observed to decrease near the edges. It was also found that shortening the original 3 mm overhang of the molybdenum clips to 1 mm reduced the layer thinning that occurs within a few millimeters of the wafer edges at low rotation rates.

9

Finally, it should be noted that if greater thickness uniformity is desired, it can be obtained at the expense of higher carrier gas flows and reduced growth efficiency. For example, at an H_2 flow of 14 slpm the nonuniformity is reduced to < 2 percent across a 4-cm diameter.

S.C. Palmateer   A. Napoleone
S.H. Groves   D.L. Hovey
J.W. Caunt

1.3 WIDEBAND INTERDIGITATED-ELECTRODE p-HgCdTe PHOTOMIXERS AT 25 μm

An essential component of far-infrared heterodyne radiometers being developed[10,11] for investigations of extraterrestrial molecular species (e.g., H_2) is a wideband photomixer. Photoconductors are very attractive for this application as they operate at much lower electric fields than photodiodes, which have limited wideband performance in the far infrared because of tunneling.[12] Even in the case of photoconductors, small electrode separations are necessary to minimize the electric field (and carrier velocity) needed to achieve good photoconductive gain at high frequencies. The interdigitated-electrode structure enables both small electrode separations and large enough active areas for efficient far-infrared detection. The structure's low resistance (varying inversely as the square of the number of electrodes) is offset in p-type HgCdTe by the low mobility of holes ($\mu_h \sim 600$ cm^2/V-s), which allows acceptable resistance values (> 50 Ω) to be obtained with hole concentrations in the 10^{15} cm^{-3} range. The long lifetime associated with this low carrier concentration does not limit the response time, as fast response can be obtained by applying sufficient bias to the photoconductor so that the high-mobility minority electrons ($\mu_e > 50,000$ cm^2/V-s) are swept out at the anode. Such minority-carrier sweepout also reduces recombination noise, leading to a heterodyne sensitivity limit close to the $h\nu\Delta f$ shot-noise limit of a photodiode. However, in p-type material sweepout constrains the photoconductive gain to <0.5, which results in the required local oscillator power P_{LO} being 4 times larger than that of an ideal photodiode. Detailed photomixer performance calculations,[11] which take into account free-carrier and intervalence-band absorption, show that NEPs $< 3 \times 10^{-20}$ W/Hz should be achievable with $P_{LO} < 100$ μW at wavelengths from 20 to 200 μm (except for the 65- to 92-μm reststrahlen region).

Long-wavelength photoconductors were made from p-type $Hg_{0.812}Cd_{0.188}Te$ material on which were evaporated gold electrodes in the form of six 4-μm-wide interleaved fingers with a 125-μm-diam. overlap region. The structure was epoxied to sapphire and thinned. Most of the device evaluation was carried out in a diode-laser heterodyne radiometer[12] consisting of a vacuum chamber with optics and a cooled pedestal where a PbSnSe diode laser local oscillator and the HgCdTe photomixer were mounted. At 18.5 K the photomixers were found to have resistance values in the range of 200 Ω at low bias, consistent with hole concentrations in the mid-10^{15} cm^{-3} range.

Figure 1-8 shows measured photocurrent vs bias for an incident diode laser power of about 50 μW. Above 370 mV, the photocurrent appears to saturate at a responsivity of about 6 A/W, which indicates sweepout and a dc quantum efficiency η of about 60 percent. Both the slope of curve before saturation and the magnitude of the bias voltage near photocurrent saturation are consistent with an effective ambipolar mobility of $\sim$60,000 cm^2/V-s and a zero-bias lifetime of $\sim$0.2 ns. At this power level the diode laser output was multimode, and strong excess RF noise[12,13] was detected from the photomixer when illuminated by the laser. At a much lower drive current, over 95 percent of the laser output was in a single mode at 24.9 μm and negligible excess RF noise was observed from the photomixer, i.e., the increase in RF noise from the photomixer was consistent with simple LO-induced generation-recombination noise for the 20-μW incident power. Under these conditions, the frequency spectrum of the LO-induced noise (shown in Figure 1-9) can be used to determine the bandwidth of the device. At a bias of 250 mV, the 3-dB bandwidth B was about 1 GHz, a value consistent with sweepout calculations.
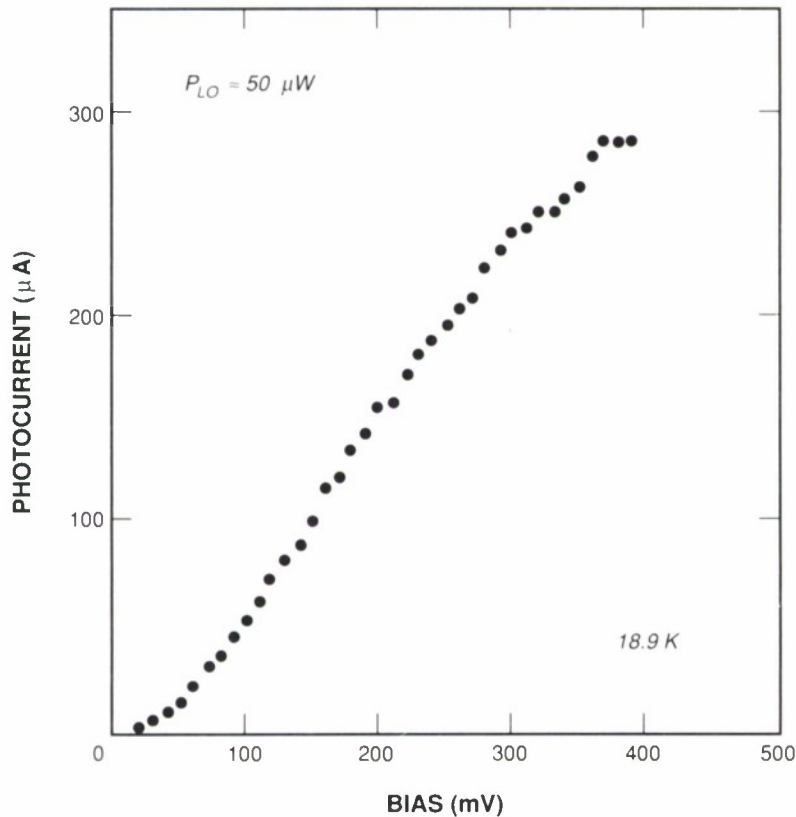
Figure 1-8.   *Response vs bias of interdigitated-electrode HgCdTe photoconductor at 25 μm.*
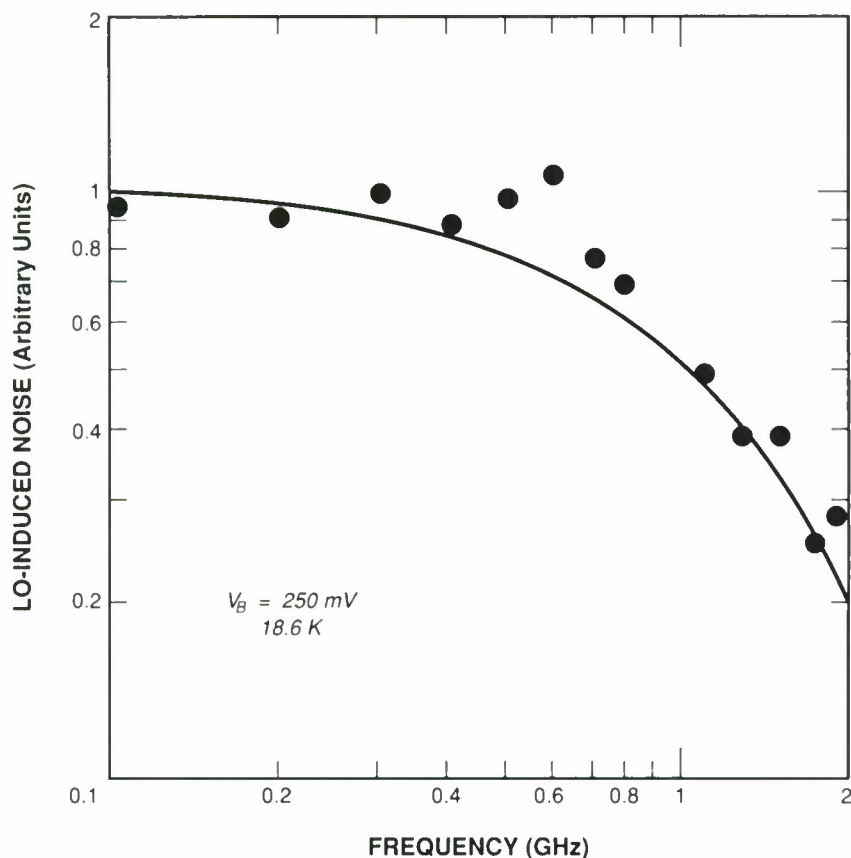
Figure 1-9.   Frequency spectrum of LO-induced noise for 25-μm HgCdTe photomixer.

Blackbody heterodyne measurements carried out with $P_{LO} = 20$ μW revealed a receiver sensitivity better than 8×10^{-19} W/Hz, which corresponds to an effective heterodyne quantum efficiency η_{EH} of about 1 percent. The ~60 times difference between η_{EH} and η was due to a combination of insufficient LO power and photomixer dark current noise. At 250 mV, dark current noise was about 3 times that of the preamplifier, whose noise temperature was 130 K. A good figure of merit for an LO-starved photomixer is the product $\eta_{EH}B/P_{LO}$. This initial unoptimized interdigitated-electrode device has a value >0.5 GHz/mW, which is significantly better than that of previous far-infrared photomixers[11] and comparable to the value for high-performance 10-μm photomixers.[14]

<div style="text-align: right">

D.L. Spears
S.T. Palmacci

</div>

REFERENCES

1. W.E. Martin, Appl. Phys. Lett. **26**, 562 (1975).

2. R.A. Becker, IEEE J. Quantum Electron. **QE-20**, 723 (1984).

3. R.L. Jungerman and C.A. Flory, Appl. Phys. Lett. **53**, 1477 (1988).

4. C.A. Wang, S.H. Groves, S.C. Palmateer, D.W. Weyburne, and R.A. Brown, J. Cryst. Growth **77**, 136 (1986).

5. S.C. Palmateer, S.H. Groves, C.A. Wang, D.W. Weyburne, and R.A. Brown, J. Cryst. Growth **83**, 202 (1987).

6. S.H Groves, S.C. Palmateer, J.W. Caunt, and D.L. Hovey, J. Cryst. Growth **93**, 242 (1988).

7. M. Razeghi, M.A. Poisson, J.P. Larivain, and J.P. Duchemin, J. Electron. Mater. **12**, 371 (1983).

8. Solid State Research Report, Lincoln Laboratory, MIT (1988:1), p. 15, DTIC AD-A201044.

9. S.C. Palmateer, S.H. Groves, J.W. Caunt, and D.L. Hovey, Electronics Materials Conference, Boulder, CO, June 1988.

10. T. Kostiuk and M.J. Mumma, Appl. Opt. **22**, 2644 (1983).

11. T. Kostiuk and D.L. Spears, Int. J. Infrared Millimeter Waves **8**, 1269 (1987).

12. D.L. Spears and R.E. Reeder, in *Digest of IEEE Int. Conf. of Infrared and Millimeter Waves* (1985), pp. 75-76.

13. R.T. Ku and D.L. Spears, Opt. Lett. **1**, 84 (1977).

14. D.L. Spears, Proc. SPIE **300**, 174 (1981).

2. QUANTUM ELECTRONICS

2.1 FREQUENCY MODULATED SINGLE-FREQUENCY Nd:YAG MICROCHIP LASERS

Single-frequency microchip lasers have recently been constructed and demonstrated using several different gain media.[1] The cavity length of these lasers is chosen small enough that the cavity mode spacing is comparable to, or greater than, the laser's gain bandwidth, so that only a single longitudinal mode will operate. The cavity length for single-frequency Nd:YAG microchip lasers operating at $1.06 \, \mu m$ is $< 750 \, \mu m$. For stoichiometric Nd compounds it is much shorter. Because of the extremely short cavity length l_0, a small change in length, δl, results in a relatively large frequency shift $\delta \nu$ away from the initial operating frequency ν_0:

$$\delta \nu = \nu_0 \, \delta l / l_0 \quad . \tag{2-1}$$

A 1.06-μm Nd:YAG microchip laser with a 750-μm cavity tunes at a rate of $400 \, \text{MHz/nm}$ of cavity length change.

By applying a transverse stress to the short-cavity lasers, their length can be changed enough to tune them over the entire gain bandwidth of the Nd:YAG.[2] In contrast to the results of Reference 2, the microchip lasers described above maintain single-frequency operation while being tuned continuously over the gain bandwidth either thermally or mechanically. To dynamically tune the 1.06-μm single-frequency Nd:YAG microchip lasers, dielectrically coated crystals were cut into 1×2-mm pieces and tight-fitted into U-shaped beryllium-copper holders adjacent to a PZT piezoelectric transducer, as shown in Figure 2-1. A voltage was applied to the transducer, which in turn applied stress to the Nd:YAG in a direction orthogonal to the laser cavity, changing the cavity length. The microchip lasers were pumped near their absorption peak at 809 nm using a Ti:Al_2O_3 laser. The frequency offset of a tunable laser from a fixed-frequency laser was measured by heterodyning.

Figure 2-2(a) shows the heterodyne spectrum of a microchip laser driven by a ± 20-V sine wave at $\sim 3 \, \text{kHz}$. The observed spectrum is in excellent agreement with calculations assuming that the output of the tunable laser varies linearly with applied voltage [Figure 2-2(b)]. Experimentally, the tuning response was measured to be $0.3 \, \text{MHz/V}$ for applied voltages between -1000 and +1000 V (the largest voltages used in these experiments), and was constant for modulation frequencies between dc and 80 kHz.

At modulation frequencies $> 80 \, \text{kHz}$, the tuning response of the microchip lasers is dominated by mechanical resonances of the microchip-transducer-holder system. At resonant frequencies between 80 kHz and 1.0 MHz the tuning was typically enhanced by a factor of 5.

At a modulation frequency of $\sim 1.1 \, \text{MHz}$ a very strong resonance was observed, which enhanced the tuning response by a factor of 44 to $13.2 \, \text{MHz/V}$. This resonance was identified as a fundamental acoustic resonance of the Nd:YAG crystal. Acoustic resonances of the Nd:YAG crystal were observed at frequencies up to 25 MHz. The heterodyne spectrum of a microchip

laser driven by a ±20-V sine wave at an acoustic resonance near 5 MHz is shown in Figure 2-3(a). There is excellent agreement with the calculated FM spectrum using a peak frequency deviation of 20.75 times the modulation frequency [Figure 2-3(b)].

The tuning capabilities of microchip lasers are unique. The microchip laser allows continuous, single-frequency tuning across the gain bandwidth of the gain medium at very high rates for application in fiber-optical gyros. With proper design of the piezoelectrically tunable, single-frequency microchip laser package it should be possible to improve both the frequency response and the amount of piezoelectric tuning obtainable.

J.J. Zayhowski   A. Mooradian
R.C. Hancock   C. Dill
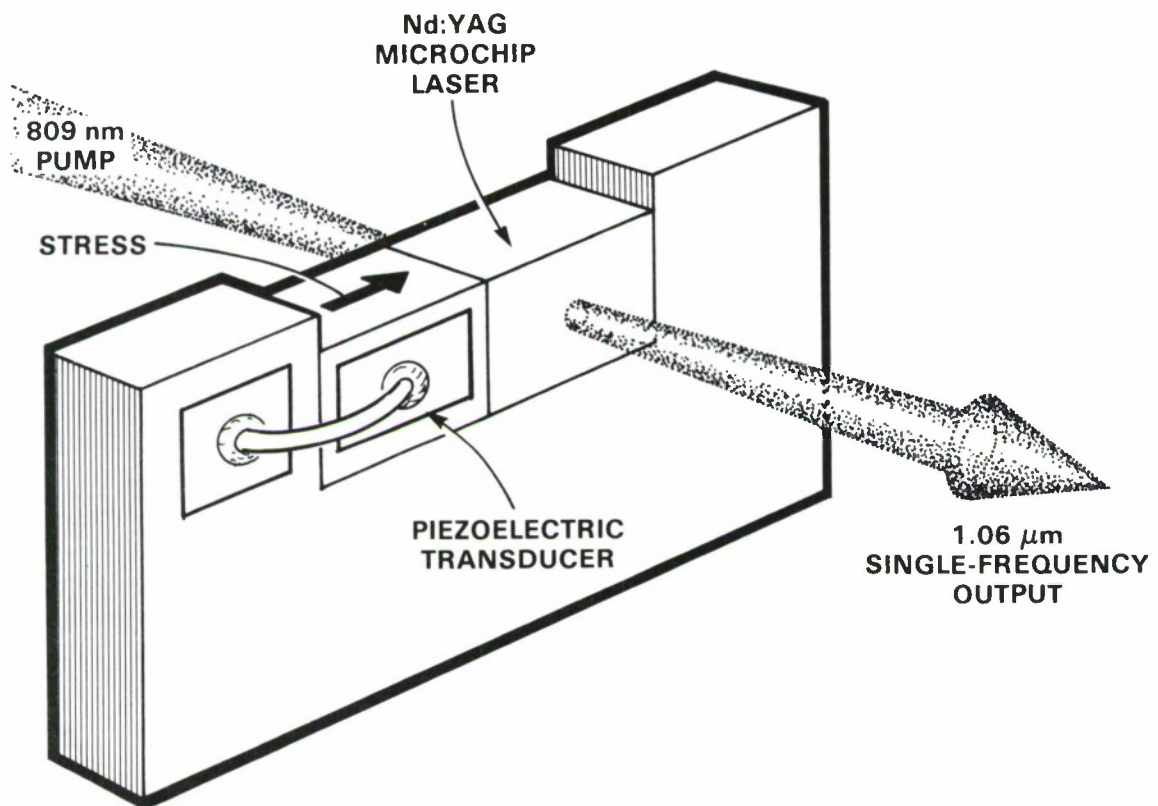
Figure 2-1.   Illustration of a piezoelectrically tunable single-frequency Nd:YAG microchip laser package. The actual size of the Nd:YAG crystal used in the experiments is 0.73 × 1.0 × 2.0 mm.
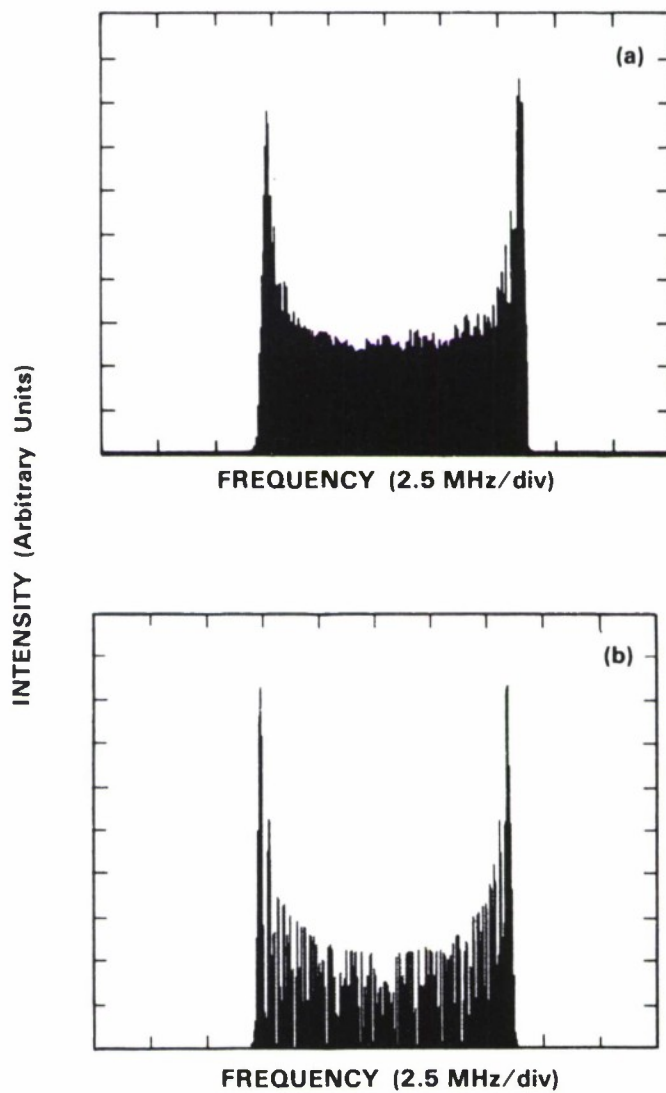
Figure 2-2. (a) Heterodyne spectrum of a piezoelectrically tuned single-frequency Nd:YAG microchip laser driven by a ±20-V sine wave at ~ 3 kHz. (b) Theoretical FM spectrum calculated for a peak frequency deviation of 160 times the modulation rate.
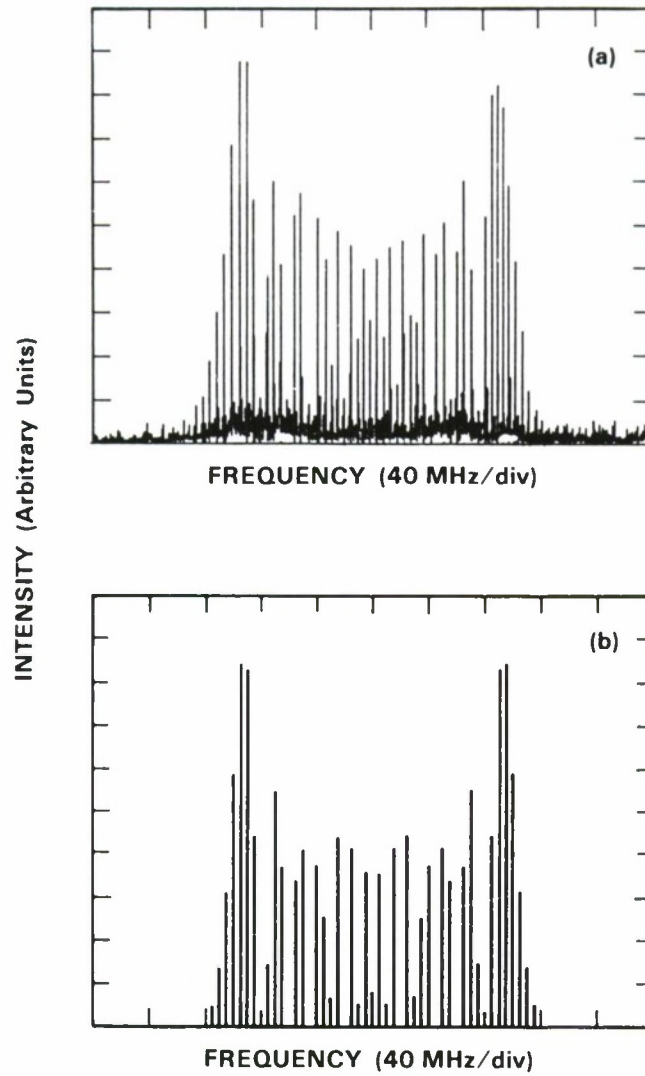
Figure 2-3. *(a) Heterodyne spectrum of a piezoelectrically tuned single-frequency Nd:YAG microchip laser driven by a ±20-V sine wave at an acoustic resonance near 5 MHz. (b) Theoretical FM spectrum calculated for a peak frequency deviation of 20.75 times the modulation rate.*

18

2.2 EFFICIENT, HIGH-AVERAGE-POWER, LIQUID-NITROGEN-COOLED Ti:Al$_2$O$_3$ LASER

A high-average-power, efficient, single-transverse-mode Ti:Al$_2$O$_3$ laser suitable both for mode-locked operation and for long-pulse, high-power pumping without damage to the laser crystal has been built using a large focal spot and liquid nitrogen cooling. A Ti:Al$_2$O$_3$ laser pumped by a 20-W argon-ion laser demonstrates a sevenfold increase in power on cooling from 300 to 77 K and has been mode-locked. This laser was also pumped by a 0.4-J, 150-μs-long pulse in which liquid nitrogen cooling increased output power by a factor of 4.

The achievement of efficient, high-average-power, single-transverse-mode solid state lasers is inhibited by pump-induced thermo-optical distortions.[3-5] These distortions are minimized by using small gain regions,[6] but high-power radiation focused onto small areas damages crystals. For example, a mode-locked laser with average power of 1 W and mode-locking frequency of 100 MHz generating 0.1-ps pulses has a peak intensity at a 20-μm beam waist radius of nearly 10^{10} W/cm^2, which is close to the damage threshold of Al$_2$O$_3$. Damage to the laser crystal can be avoided by designing the laser with a large spot size. The thermo-optical distortions inherent in high-power Ti:Al$_2$O$_3$ lasers with large spot sizes can be reduced by increasing the thermal conductivity.[7]

For Al$_2$O$_3$ the thermal conductivity increases from 0.33 W/cm-K at 300 K to 10 W/cm-K at 77 K (Reference 8), a factor of 30. Although the temperature dependence has not been measured in Ti:Al$_2$O$_3$, a substantial increase in thermal conductivity can be expected as the temperature is decreased.

The effects of cooling were observed for CW operation of a Ti:Al$_2$O$_3$ laser pumped by a 20-W argon-ion laser. A folded, three-mirror (R_1, R_2=25 cm; R_3=∞), astigmatically compensated cavity with a total length of 100 cm was used, similar to the cavity of Sanchez et al.[9] The pump beam radius at the crystal was ~ 65 μm. With 15 W of green light absorbed by the 42-cm-long crystal, the thermal heat load was 2×10^4 W/cm^3. The Ti:Al$_2$O$_3$ crystal was located in an evacuated, liquid nitrogen Dewar inside the laser cavity. Indium foil was used to obtain good thermal contact between the crystal and copper heat sink. Since the laser mirrors were outside the Dewar, low-loss Brewster-angled windows formed the 10^{-7}-Torr vacuum seal. A view port was used to aid in alignment.

The Ti:Al$_2$O$_3$ laser was adjusted at room temperature to a maximum output of 0.4 W. Upon cooling, the output rose to 1.9 W. With the crystal at 77 K the mirrors were readjusted to obtain an output power of 2.8 W. A 20-percent increase in output power is expected because the non-radiative rate decreases at lower temperatures.[10] However, the very large increase in output power with cooling is only consistent with a decrease in thermo-optical distortion upon cooling.

In our cavity the slope efficiency of 20 percent observed at 77 K is much larger than the slope efficiency observed at room temperature, but is no greater than has been obtained at room temperature in other cavities.[11] Thus, the liquid nitrogen cooling alleviates thermal effects in the present cavity, but is unlikely to substantially improve operation of a cavity that is optimized for room-temperature operation.

If the dn/dT term in the equation for the focal length of the thermal lens[5] is assumed to be the major contribution, the focal length for the operating conditions described above is 2.1 cm at 300 K and 65 cm at 77 K. Although the theoretical assumption that the focal length of the lens is much longer than the crystal length is not valid for 300 K, these focal lengths are a qualitative indication of the strength of the thermo-optic effects. A simple thermal lens in the cavity can be easily compensated by changing the mirror separation to improve the laser performance. However, other thermo-optic effects such as astigmatism and spherical aberration cannot be compensated in this way. Hence, cooling or cavity parameter changes are necessary to obtain efficient high-power, single-transverse-mode operation.

Mode-locked output of the liquid-nitrogen-cooled Ti:Al$_2$O$_3$ laser has also been obtained using second harmonic mode locking.[12] With 15 W pump power, the laser generated 36-ps pulses at a repetition rate of 125 MHz with 0.8 W average power. The mode locking was accomplished with a 125-MHz standing-wave acousto-optic modulator and a cavity length of 120 cm.

In addition, the same laser was used in pulsed operation with minor modifications. An amplified, mode-locked Nd:YAG was frequency doubled in LiIO$_3$ to pump the Ti:Al$_2$O$_3$ laser. The output of the pump at 532 nm consisted of 150-ms train of 100-ps pulses every 10 ns, repeated at a 10-Hz rate, and had an average power of 4 W. The crystal was moved away from the pump focus to avoid damage, resulting in a 200-μm beam radius.
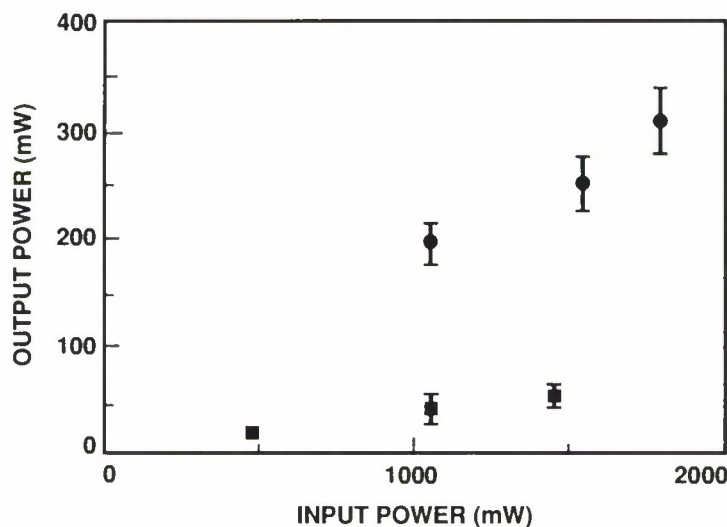
Figure 2-4. Laser output power improvement with cooling. When operated with liquid nitrogen cooling (circles), the average output power vs input power characteristics are improved by a factor of 4 compared with room-temperature operation (squares). The Ti:Al$_2$O$_3$ laser was operating at 809 nm.

Figure 2-4 shows the output power vs input power for cooled and uncooled operation of the pulsed laser. As in the CW case, the laser was adjusted for maximum output under uncooled conditions and then cooled. The cooling increased the output by a factor of 4. On the basis of a simple model,[9] the slope efficiency shown in Figure 2-4 should be independent of nonradiative relaxation rates. Once again, the cooling reduces thermo-optic distortion and thereby increases efficiency.

<div align="right">
S.R. Henion
P.A. Schulz
</div>

2.3 SPECTROSCOPY OF Ti:YAlO$_3$

There is considerable interest in YAlO$_3$ doped with Ti^{3+} ions as a material for tunable solid state lasers because Ti:YAlO$_3$ has a fluorescence emission band extending from $\sim$ 550 to 800 nm. However, there is only one report[13] of lasing in Ti:YAlO$_3$. Failure to obtain lasing has been attributed either to a broad parasitic absorption band or to pump-induced absorption. We report here on the spectroscopic characterization of Ti:YAlO$_3$ crystals that have no detectable parasitic absorption. We have not been able to achieve lasing in these crystals. We attribute this failure to pump-induced excited-state absorption, presumably arising from charge transfer to energy levels of defects.

The fluorescence spectrum and lifetime of Ti:YAlO$_3$ were measured for a single-crystal sample from a polycrystalline ingot grown by the unseeded heat exchanger method (HEM)[14] from a melt containing 0.1 wt% Ti$_2$O$_3$. A 6.5-mm-long crystal grown by this method from a melt containing 0.3 wt% of Ti$_2$O$_3$ was used for measurements of absorption and pump-induced absorption. All measurements were made at room temperature.

For fluorescence emission measurements, the sample was pumped with 10-ns pulses of 532-nm radiation from a frequency-doubled Nd:YAG laser. The observed spectrum, not corrected for the spectral response of the spectrometer and photomultiplier tube, is shown in Figure 2-5. The emission peaks at 600 nm and extends from 540 to 800 nm.

The fluorescence lifetime was measured in the same setup by monitoring the signal at 620 nm, near the peak of the emission. The temporal decay of the emission is shown in Figure 2-6(a). The natural logarithm of the intensity I is plotted against time in Figure 2-6(b); a linear fit to the data yields a value of $11.4 \pm 0.5\ \mu s$ for the fluorescence lifetime of the excited state of Ti^{3+} in YAlO$_3$, in agreement with previously reported values.[15,16]

The unpolarized transmission spectrum measured for the other crystal is shown in Figure 2-7. The Ti^{3+} absorption band is clearly seen between 380 and 550 nm. From 600 to 800 nm the spectrum is relatively flat, indicating the absence of significant parasitic absorption. However, the maximum transmission is only 60 percent, although reflection losses at the two faces of the crystal account for only a 21-percent reduction in the transmission. We believe that the remaining 19-percent reduction is due to scattering losses resulting from twin planes or other defects.

<div align="center">
21
</div>
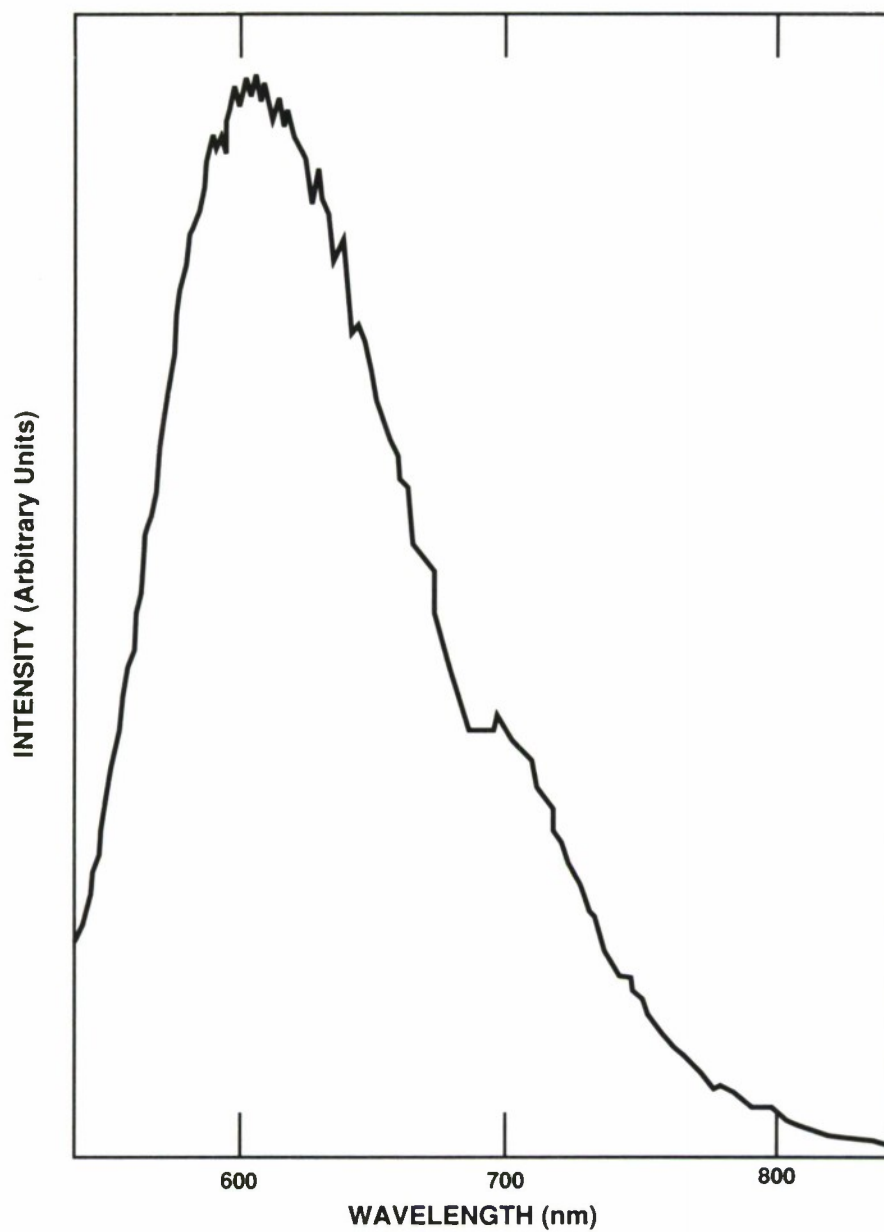
Figure 2-5. Room-temperature fluorescence emission spectrum of an unoriented Ti:YAlO₃ sample taken from an ingot grown with 0.1 wt% Ti₂O₃. The sample was pumped with 532-nm, 10-ns pulses from a frequency-doubled Nd:YAG laser. The spectrum was not corrected for the spectral response of the measurement system.
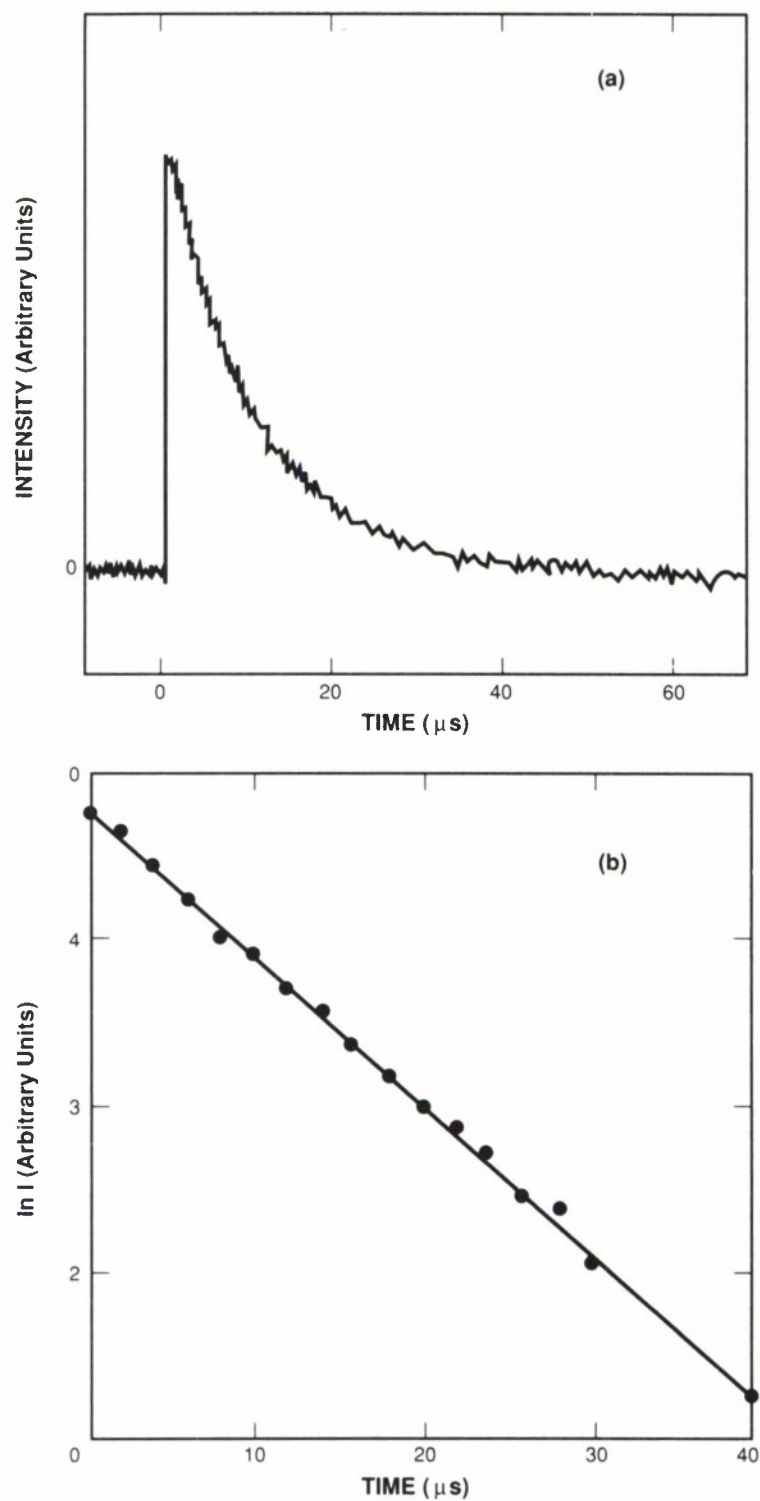
Figure 2-6. The temporal decay of the fluorescent intensity I at 620 nm for the sample of Figure 2-5: (a) I vs time and (b) ln I vs time. The straight line in (b) is a linear fit to the data shown as solid circles.
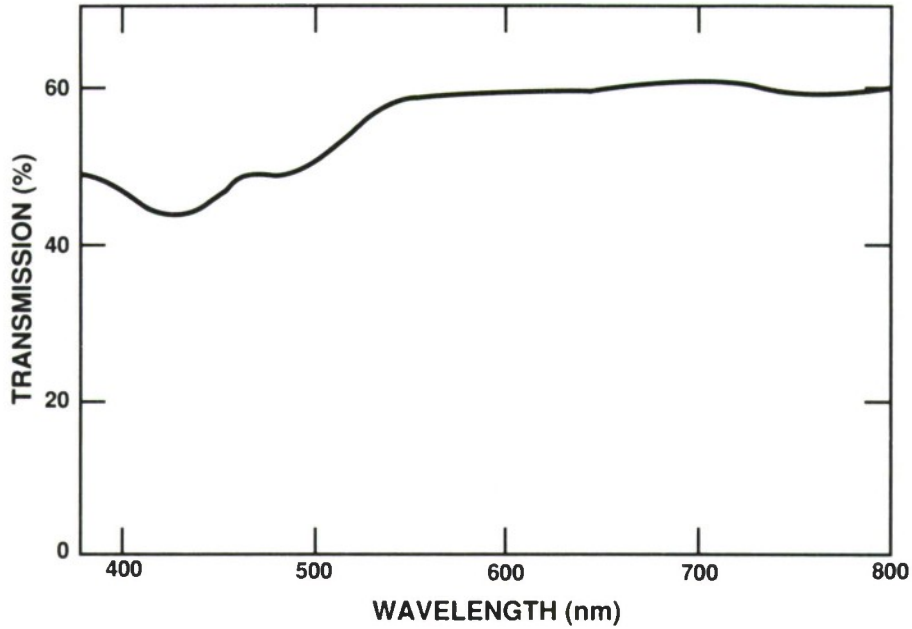
Figure 2-7. Room-temperature transmission spectrum of an unoriented, 6.5-mm-long Ti:YAlO$_3$ sample taken from an ingot grown with 0.3 wt% Ti$_2$O$_3$.

From the transmission spectrum of Figure 2-7 we deduce the peak absorption coefficient $\alpha_m \approx 0.5$ cm^{-1} at 430 nm and estimate an upper limit of 0.03 cm^{-1} for the parasitic absorption coefficient α_p, yielding a lower limit of 15 for the figure of merit defined as α_m/α_p. The figure of merit of previous crystals[13,15,16] ranges from about 1.5 to 3. It is evident that HEM-grown crystals are significantly improved.

The Ti^{3+} concentration in HEM-grown Ti:YAlO$_3$ can be deduced by dividing α_m by the absorption cross section σ_y which is estimated by comparison with that of Ti:Al$_2$O$_3$. The ratio of the absorption cross sections is given by

$$\frac{\sigma_y}{\sigma_s} = \left(\frac{\lambda_y}{\lambda_s}\right)^2 \left(\frac{\tau_s}{\tau_y}\right) \left(\frac{\Delta\nu_s}{\Delta\nu_y}\right) \left(\frac{n_s}{n_y}\right)^2 , \tag{2-2}$$

where λ is the vacuum wavelength for the absorption peak; τ is the lifetime of the excited state; $\Delta\nu$ is the full width at half-maximum of the absorption band; n is the index of refraction; and the subscripts y and s refer to Ti:YAlO$_3$ and Ti:Al$_2$O$_3$, respectively. From our measured values of λ, τ, and $\Delta\nu$ and the published values for n (Reference 17), we find $\sigma_y/\sigma_s = 0.15$. The reported[18] value of 9.3×10^{-20} cm^2 for σ_s then yields a value of 3.6×10^{19} cm^{-3} for the Ti^{3+} concentration in the sample whose absorption spectrum is shown in Figure 2-7. This concentration corresponds to 0.08 wt% of Ti$_2$O$_3$ if all the titanium ions are in the 3$^+$ charge state.

24

Gain measurements at 632.8 nm, using a signal beam from a He-Ne laser, were attempted on the crystal that was used for the transmission measurements. The crystal was pumped with 532-nm, 10-ns pulses from a frequency-doubled Nd:YAG laser. The signal and pump beams were nearly collinear and their polarizations were parallel. Instead of gain we observed a pump-induced loss.

Figure 2-8(a) shows the temporal behavior of the pump-induced absorption coefficient α_i for an incident fluence of 0.6 J/cm^2; t = 0 denotes the time at which the pump pulse was incident on the sample. Figure 2-8(b) is a plot of the natural logarithm of α_i vs time. The pump-induced absorption decays with a time constant of 12.7 $\pm$ 1.0 μs. The similarity between this time constant and the value of 11.4 μs measured for the fluorescence lifetime of Ti^{3+} in $YAlO_3$ leads us to conclude that the pump-induced absorption is due to transitions originating from the excited state of Ti^{3+}.

The term "excited-state absorption" is normally used to denote transitions from an excited state to still higher states of the same species. Transitions from the 3d excited state of Ti^{3+} to higher states within the Ti^{3+} manifold are unlikely because the 4p and 4f levels of the free ion are, respectively, 16 and 29 eV above the 3d ground state. Furthermore, the observation[13] of lasing for a 3.5-mm-long Ti:$YAlO_3$ crystal suggests that the pump-induced absorption in our crystal is not intrinsic to Ti:$YAlO_3$. Therefore, we attribute this absorption to charge transfer from the 3d excited state to energy levels of unidentified defects.

K.F. Wall   C.P. Khattak*
R.L. Aggarwal   F. Schmid*

2.4 ANALYSIS OF GAIN NARROWING IN AMPLIFIED SPONTANEOUS EMISSION

Gain narrowing for various fluorescence line shapes is analyzed. For large gains, if the fluorescence behavior is quadratic near the gain peak, it is shown that this initial curvature is narrowed because of the gain by a factor that is independent of the detailed line shape. The reduction in amplified fluorescence for a peaked, non-flat-top fluorescence profile compared with a square or flat-top fluorescence profile depends on additional characteristics of the line shape. For example, this reduction in amplified spontaneous emission (ASE) is greater for a Lorentzian than for a parabolic profile assuming equal fluorescence.

To show this we start with the results of Section 2.1 of the last report.[19] With reference to Equation 2-7 of that report and the symbols defined therein, we note that

$$G \equiv \frac{I_{out}c^2}{\Omega hn^2} = \int_0^\infty \{\exp\left[\gamma_0\sigma(\nu)/\sigma_0\right] - 1\}\nu^3 d\nu \tag{2-3}$$

---

* Crystal Systems Incorporated, Salem, Massachusetts.
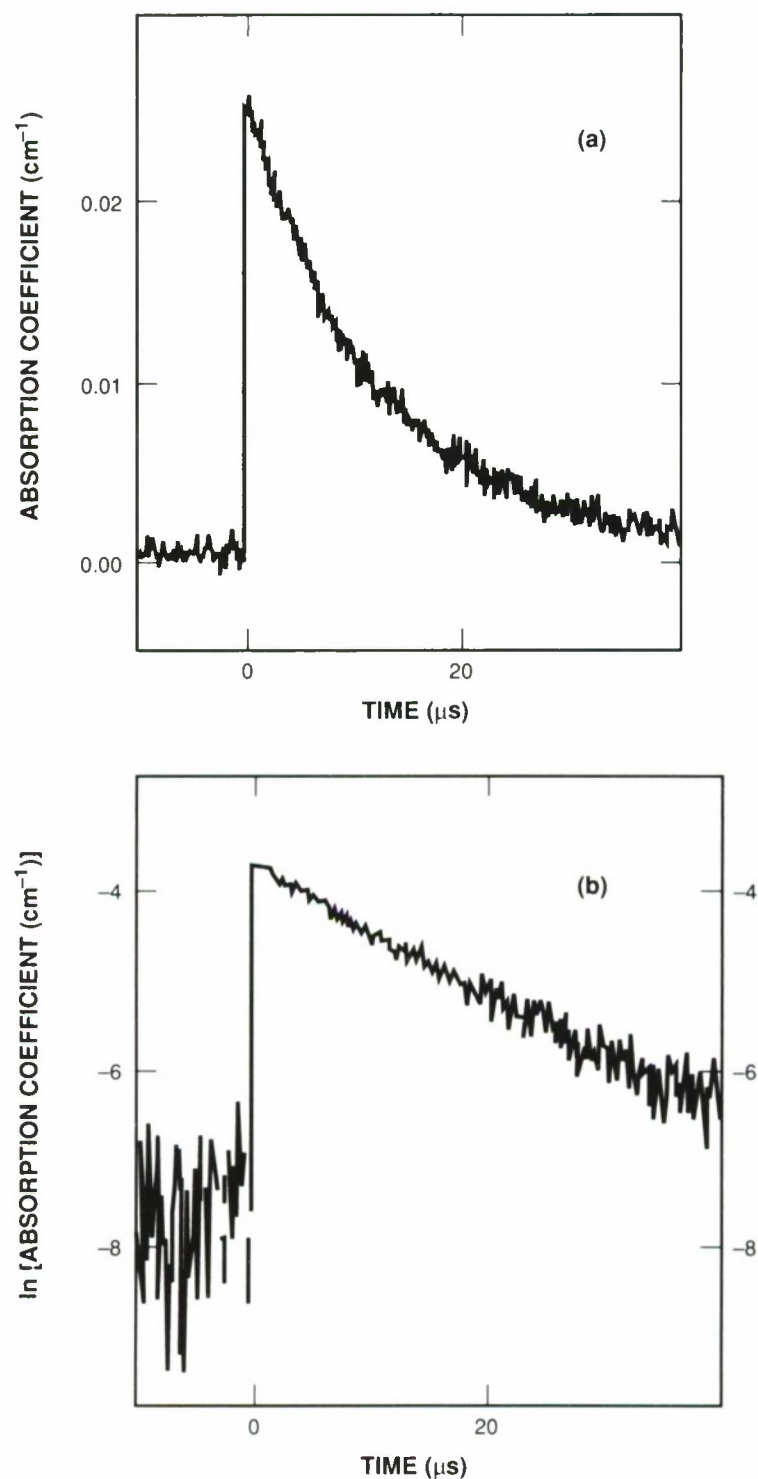
Figure 2-8.   Temporal decay of the pump-induced absorption coefficient α_i at 632.8 nm: (a) α_i vs time t and (b) the natural logarithm of α_i vs t. The pump fluence was 0.6 J/cm^2.

diverges (i.e., there is an ultraviolet catastrophy) if $\sigma(\nu)$ is Lorentzian. Removing ν^3 from inside the integral "solves" this difficulty. Other forms of $\sigma(\nu)$ can be found which do not diverge, for example, the triangular and parabolic distributions. Let us consider several distributions for the case where ν^3 is taken outside the integral, as follows:

$$G \approx \nu_0^3 H(\gamma_0) \quad , \tag{2-4}$$

where

$$H(\gamma_o) = \int_{-\infty}^{\infty} dx\{\exp[\gamma_0 h(x)] - 1\} \quad . \tag{2-5}$$

Here, $x = \nu-\nu_0$, $h(x) = \sigma(\nu)/\sigma_0$ and ν_0 is the peak gain frequency of the emission band. We have also extended the lower limit on the integral from $-\nu_0$ to $-\infty$, assuming the emission width is much smaller than the center frequency.

Table 2-1 gives expressions for $H(\gamma_0)$ for square, triangular, parabolic and Lorentzian distributions. Note that erf denotes the error function and I_n the modified Bessel function of order n. Approximations for $H(\gamma_0)$ are also given for the parabolic and Lorentzian distributions when γ_0 is large. The values of Γ for the various distributions are given when the fluorescence output is normalized; the ratio of the amplified fluorescence to the normal fluorescence is shown in the last column for each distribution in the case where γ_0 is large.

Several points can be made concerning these results:

(a) For large γ_0, the parabolic and Lorentzian distributions give nearly the same result assuming the curvature near the peak of the line is identical, i.e., $\Gamma_p = \Gamma_l$.

(b) The ASE for smoothly varying gain peaks, such as the parabolic and Lorentzian, is determined for large γ_0 by the curvature at the spontaneous peak and the value of γ_0.

(c) For equal spontaneous fluorescence output, the Lorentzian half-width is smaller than the parabolic half-width and the ASE is much more strongly reduced for the Lorentzian than the parabolic because of the extra narrowness of the Lorentzian.

It is apparent from the above that the ASE at high gain is readily calculated if the curvature of the spontaneous fluorescence peak is known, but that comparison of ASE with spontaneous output requires detailed knowledge of the line shape.

<div align="right">P.L. Kelley</div>

TABLE 2-1

Amplified Spontaneous Emission Factor, $H(\gamma_0)$, for Various Spontaneous Emission Distributions

	$h(x)$	$H(\gamma_0)$	Γ/Γ_s for Equal Fluorescence	$H(\gamma_0)/2\Gamma_s$ for Equal Fluorescence
Flat-Top	$1 \ , \ \|x\| < \Gamma_s$ $0 \ , \ \|x\| > \Gamma_s$	$2\Gamma_s(e^{\gamma_0} - 1)$	1	$e^{\gamma_0} - 1$
Triangular	$1 - \dfrac{\|x\|}{\Gamma_t} \ , \ \|x\| \leq \Gamma_t$ $0 \ , \ \|x\| \geq \Gamma_t$	$2\Gamma_t\left(\dfrac{1}{\gamma_0}e^{\gamma_0} - \dfrac{1}{\gamma_0} - 1\right)$	2	$2\left(\dfrac{1}{\gamma_0}e^{\gamma_0} - \dfrac{1}{\gamma_0} - 1\right)$
Parabolic	$1 - \dfrac{x^2}{\Gamma_p^2} \ , \ \|x\| \leq \Gamma_p$ $0 \ , \ \|x\| \geq \Gamma_p$	$\Gamma_p\left(\sqrt{\dfrac{\pi}{\gamma_0}}e^{\gamma_0}\mathrm{erf}(\gamma_0) - 2\right)$ $\approx \Gamma_p\left(\sqrt{\dfrac{\pi}{\gamma_0}}e^{\gamma_0} - \dfrac{1}{\gamma_0} - 2\right), \ \gamma_0 >> 1$	$\dfrac{3}{2}$	$\approx \dfrac{3}{4}\left(\sqrt{\dfrac{\pi}{\gamma_0}}e^{\gamma_0} - \dfrac{1}{\gamma_0} - 2\right)$ $\gamma_0 >> 1$
Lorentzian	$\dfrac{1}{1 + \dfrac{x^2}{\Gamma_l^2}}$	$\Gamma_l\pi\gamma_0 e^{\gamma_0/2}\left[I_0\left(\dfrac{\gamma_0}{2}\right) - I_1\left(\dfrac{\gamma_0}{2}\right)\right]$ $\approx \Gamma_l\sqrt{\dfrac{\pi}{\gamma_0}}e^{\gamma_0}\left(1 + \dfrac{3}{4\gamma_0}\right), \ \gamma_0 >> 1$	$\dfrac{2}{\pi}$	$\approx \sqrt{\dfrac{1}{\pi\gamma_0}}e^{\gamma_0}\left(1 + \dfrac{3}{4\gamma_0}\right)$ $\gamma_0 >> 1$

2.5 OPTICAL ABSORPTION IN KNbO₃

Optical absorption in $KNbO_3$ from one commercial vendor has been measured in the near-infrared and visible. The strength of the absorption is high enough to lower second harmonic generation (SHG) efficiency through phase mismatch induced by the change in index of refraction with temperature.

Our initial experiments using $KNbO_3$ for pulsed, high-average-power SHG indicated that absorption at both the fundamental and second harmonic limited the conversion efficiency. As the average power increased from a 1.06-μm Nd:YAG laser, the optimum phase-matching angle for critically phase-matched SHG changed. Also, the time dependence of the second harmonic output showed that during a pulse, absorption caused the temperature of the $KNbO_3$ to chirp through the phase-matching temperature. The phase-matching temperature bandwidth in $KNbO_3$ is relatively small compared with other nonlinear crystals such as $LiIO_3$ and $KTiOPO_4$ (KTP); thus, a similar level of optical absorption causes a more severe problem. Nonetheless, $KNbO_3$ is of great interest for SHG because of its relatively large nonlinearity.

We chose to use a laser calorimetry technique[20] to measure the absorption in $KNbO_3$. A schematic of the experiment is shown in Figure 2-9. A laser beam with constant average power was focused into a sample that was suspended by a thermocouple. The sample was in a small box to minimize air currents. The laser power through the sample and the temperature of the sample were monitored. Once the sample temperature reached steady state, the laser beam was turned off and the sample cooled to equilibrium with an exponential time dependence. The absorption α is given by

$$\alpha = \frac{\Delta T c_p m}{\tau L P_m \frac{1+R}{1-R}} \quad , \tag{2-6}$$

where ΔT is the difference between the steady-state temperature with the laser on and the equilibrium temperature, τ is the time constant of the temperature decrease, c_p is the heat capacity of the sample, m is its mass, P_m is the measured laser power, L is the path length of laser beam through the sample, and R is the Fresnel reflection of the sample.

Table 2-2 shows the results for a single sample of $KNbO_3$ from one vendor of this material for various wavelengths, polarization, and propagation directions. The absorption is in the same range as that recently measured for other nonlinear crystals[21] and lower than that previously measured in the visible for samples of this material from the same vendor.[22] A similar level of absorption in the near-infrared in $KNbO_3$ has been previously measured[23] in material grown by a different manufacturer. The source of the absorption in the visible is unclear but crystal growth studies indicate that the transmission spectrum is sensitive to growth conditions.[24] Low levels of impurities may cause the absorption especially near the band edge as in $BaTiO_3$ (Reference 25). It may be possible to reduce the absorption through improved crystal growth and higher purity material; the lowest-loss nonlinear crystals have an order of magnitude less absorption.[21]

The expected conversion efficiency for diode laser doubling is reduced because of phase mismatch caused by absorption. The reduction in conversion efficiency is dependent on a number of factors including the average power, crystal length, and thermal conductivity of $KNbO_3$.

T.Y. Fan
W.E. DeFeo
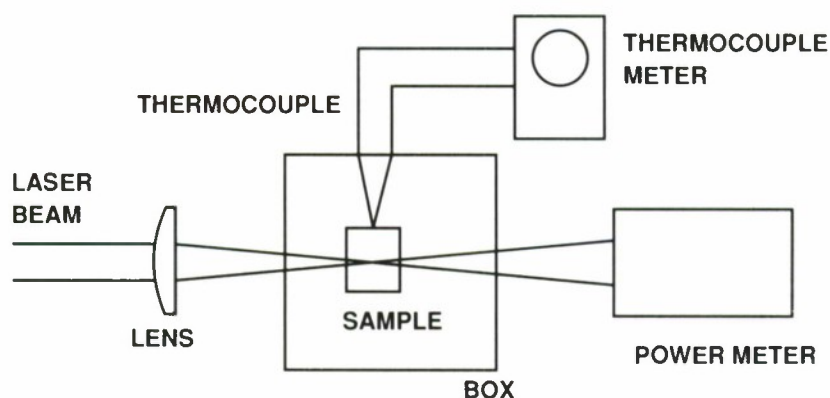
Figure 2-9. Schematic of optical absorption experiment.

TABLE 2-2				
Absorption Coefficients in $KNbO_3$				
WAVELENGTH (nm)	**k∥a***		**k∥b***	
	E∥c† (cm^{-1})	E∥b† (cm^{-1})	E∥c† (cm^{-1})	E∥a† (cm^{-1})
476.5	0.047	0.062	0.047	0.047
514.5	0.031	0.047	0.026	0.025
1064	0.0025	0.0018	0.0018	0.0016
1320	0.0029	0.0029	0.0032	0.0031

* Propagation Direction

† Polarization

REFERENCES

1. J.J. Zayhowski and A. Mooradian, Opt. Lett. **14**, 24 (1989).

2. A. Owyoung and P. Esherick, Opt. Lett. **12**, 999 (1987).

3. P.A. Schulz, IEEE J. Quantum Electron. **QE-24**, 1039 (1988).

4. S. DeSilvestri, P. Laporta, and V. Magni, IEEE J. Quantum Electron. **QE23**, 1999 (1987).

5. W. Koechner, in *Solid State Laser Engineering* (Springer-Verlag, New York, 1978), p. 359.

6. A. Sanchez, R.L. Aggarwal, A.J. Strauss, and R.E. Fahey, IEEE J. Quantum Electron. **QE-24**, 995 (1988).

7. P.F. Moulton, J. Opt. Soc. Am. B **3**, 125 (1986).

8. C. Kittel, in *Introduction to Solid State Physics*, 3rd edition (J. Wiley and Sons, New York, 1968), p. 192.

9. A. Sanchez, R.E. Fahey, A.J. Strauss, and R.L. Aggarwal, Opt. Lett. **11**, 363 (1986).

10. P. Albers, E. Stark, and G. Huber, J. Opt. Soc. Am. B **3**, 134 (1986).

11. A. Alfrey and T. Baer, Spectra-Physics (private communication) and Spectra-Physics Ti:Al_2O_3 laser product literature.

12. U. Keller, J.A. Valdmanis, M.C. Nuss, and A.M. Johnson, IEEE J. Quantum Electron. **QE-24**, 427 (1988).

13. J. Kvapil, M. Koselja, J. Kvapil, B. Perner, V. Skoda, J. Kubelka, K. Hamal, and V. Kubacek, Czech. J. Phys. B **38**, 237 (1988).

14. C.P. Khattak and F. Schmid, in *Advances in Optical Materials*, edited by S. Musikant, Proc. SPIE **505**, 4 (1984).

15. K.L. Schepler, in *Tunable Solid State Lasers II, Springer Series in Optical Sciences*, Vol. 52, edited by A.B. Budgor, L. Esterowitz, and L.G. DeShazer (Springer-Verlag, New York, 1986), p. 235.

16. P.F. Moulton, Final Report: An Investigation of Ti:$YAlO_3$ as a Tunable Laser Material, Contract No. N00014-85-C-0533, Schwartz Electro-Optics, Inc. (1987).

17. A.A. Kaminskii, *Laser Crystals* (Springer-Verlag, New York, 1981), p. 321.

18. R.L. Aggarwal, A. Sanchez, R.E. Fahey, and A.J. Strauss, Appl. Phys. Lett. **48**, 1345 (1986).

19. Solid State Research Report, Lincoln Laboratory, MIT (1988:4), pp 15-17.

20. D.C. Johnson, Appl. Opt. **12**, 2192 (1973).

21. D.J. Gettemy, W.C. Harker, G. Lindholm, and N.P. Barnes, IEEE J. Quantum Electron. **QE-24**, 2231 (1988).

22. M.D. Sciacca, S. B. thesis, Massachusetts Institute of Technology, 1987.

23. Y. Uematsu and T. Fukuda, Jpn. J. Appl. Phys. **12**, 841 (1973).

24. T. Fukuda and Y. Uematsu, Jpn. J. Appl. Phys. **11**, 163 (1972).

25. P.G. Schuremann, D.A. Temple, R.S. Hathcock, H.L. Tuller, H.P. Jenssen, D.R. Gabbe, and C. Warde, J. Opt. Soc. Am. B **5**, 1685 (1988).

3. MATERIALS RESEARCH

3.1 LARGE-AREA UNIFORM OMVPE GROWTH FOR GaAs/AlGaAs DIODE LASERS

High-power arrays of GaAs/AlGaAs diode lasers are under intensive development as sources for pumping Nd:YAG lasers. Graded-index separate-confinement heterostructure single-quantum-well (GRIN-SCH SQW) lasers are attractive for this application because of their low threshold current density and high differential quantum efficiency. At room temperature, the most strongly absorbing Nd:YAG pump band is located at 806 ± 2.5 nm. Because of the narrowness of this band, efficient pumping requires very close control of the diode laser emission wavelength and, therefore, of the properties of wafers used for diode fabrication. We have used large-area multi-layer structures grown by OMVPE for the fabrication of high-performance broad-area GRIN-SCH SQW diode lasers with emission wavelengths that fall within the Nd:YAG pump band. The operating characteristics of lasers from the same wafer exhibit a high degree of uniformity, and the wafer-to-wafer reproducibility is excellent for devices fabricated from structures grown under the same nominal conditions.

The laser structures were grown at 800°C on ~4 × 4-cm D-shaped substrates in a vertical rotating-disk reactor described previously.[1] The source materials were trimethylgallium, trimethylaluminum, 100-percent arsine, H_2Se (500 ppm in H_2), and diethylzinc or dimethylzinc (3000 ppm in H_2). Residual H_2O and O_2 were removed from the arsine by an active polymeric resin.[*] The reactor pressure was controlled at 0.2 atm, the total mass flow rate was 10 slpm, and the susceptor rotation rate was 500 rpm. For growth on 5-cm-diam. round substrates, these conditions yield epilayers with thickness uniformity of ±1 percent and uniformity in Al content of ±0.2 percent (Reference 1).

The basic GRIN-SCH SQW structure used in this study, as shown schematically in Figure 3-1, consists of a five-period n-GaAs/$Al_{0.6}Ga_{0.4}As$ (10 nm/10 nm) superlattice buffer layer (n = 2×10^{18} cm^{-3}), 1.8-μm-thick n-$Al_{0.6}Ga_{0.4}As$ cladding layer, 0.2-μm-thick undoped $Al_xGa_{1-x}As$ layer (linearly graded from x = 0.6 to 0.3), single undoped 10-nm-thick $Al_{0.07}Ga_{0.93}As$ active region, 0.2-μm-thick undoped $Al_xGa_{1-x}As$ layer (linearly graded from x = 0.3 to 0.6), 1.8-μm-thick p-$Al_{0.6}Ga_{0.4}As$ cladding layer, and 0.25-μm-thick p^+-GaAs contact layer (p = 8×10^{19} cm^{-3}). With increasing distance from the active layer, the n-doping levels in the cladding layers were linearly graded from ~ 0.5 to 1.5×10^{18} cm^{-3}, as determined by C-V measurements. Increasing the doping level in these layers significantly degraded the overall laser performance.

For laser fabrication, 100-μm-wide Cr/Au stripes on 400-μm centers were first defined on the p^+-GaAs surface by means of evaporation and photolithographic liftoff. The p^+ contact layer was etched away between the stripes to isolate them and reduce current spreading. The wafer was thinned to about 100 μm, and Au/Sn/Au was evaporated onto the n^+ substrate and subsequently

---

* Waferpure™, Millipore Corporation, Bedford, Massachusetts.
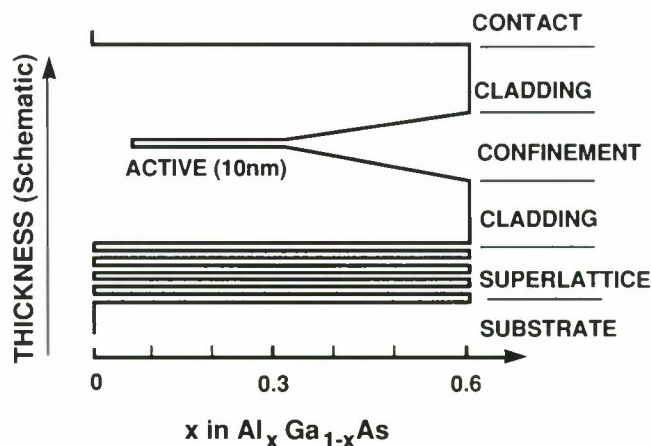
Figure 3-1.   Schematic diagram of GRIN-SCH SQW diode laser structure.

alloyed at 380°C. For uniformity evaluation, the wafer was divided into 14 sections and 500-μm-long bars were cleaved from each section. One bar from each section, mounted p-side up, was soldered to a copper block with indium. Individual lasers were probe-tested at room temperature under pulsed conditions, using 200-ns current pulses at 10 kHz. Output power was measured with a silicon photodiode. Curves of output power vs current were measured for at least 12 devices from each section to determine values of the threshold current density J_{th} and differential quantum efficiency η_d.

Figure 3-2 shows the distribution of J_{th} and η_d for 192 lasers. The mean value and standard deviation σ of J_{th} are 287.5 and 11.3 A cm^{-2}, respectively, giving a coefficient of variation $\sigma/J_{th,mean}$ of 0.039. The mean value and σ of η_d are 83.0 and 2.5 percent, respectively, for a coefficient of variation of 0.03. The highest value of η_d measured, 88 percent, is among the highest values reported in the literature. The highest degree of uniformity previously reported for OMVPE-grown GaAs/AlGaAs lasers was obtained by Druminski *et al.*[2] for double-heterostructure, oxide-defined, 3-μm-stripe lasers on a 4-cm^2 substrate. For the threshold current the mean value and coefficient of variation were 108 mA and 0.047, respectively, while the corresponding values for η_d were 16.8 percent and 0.18, respectively.

Figure 3-3 shows the distribution of emission wavelengths for 175 devices from the same wafer. The mean value and σ are 804.9 and 0.6 nm, respectively. For an active layer thickness of 10 nm, the calculated change in wavelength with thickness is 1 nm per monolayer. Thus the data indicate that over the whole wafer, the active layer is uniform in thickness to within a few monolayers. In initial experiments to investigate wafer-to-wafer reproducibility, the emission wavelength has also been measured for a few lasers from each of four subsequent wafers with the same nominal device structure. For all the devices from the five wafers, the wavelength variation is ±1.5 nm.

C.A. Wang   W.L. McGilvary
H.K. Choi   L.J. Missaggia
M.K. Connors   J.N. Walpole
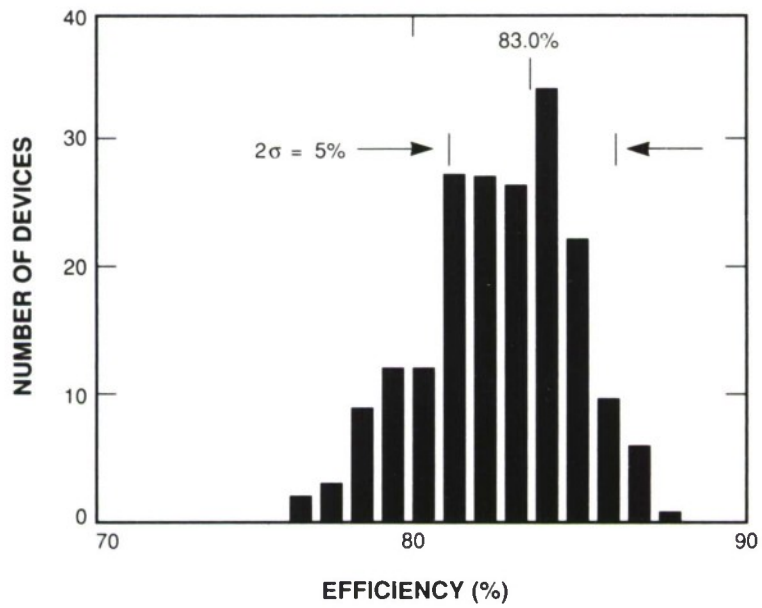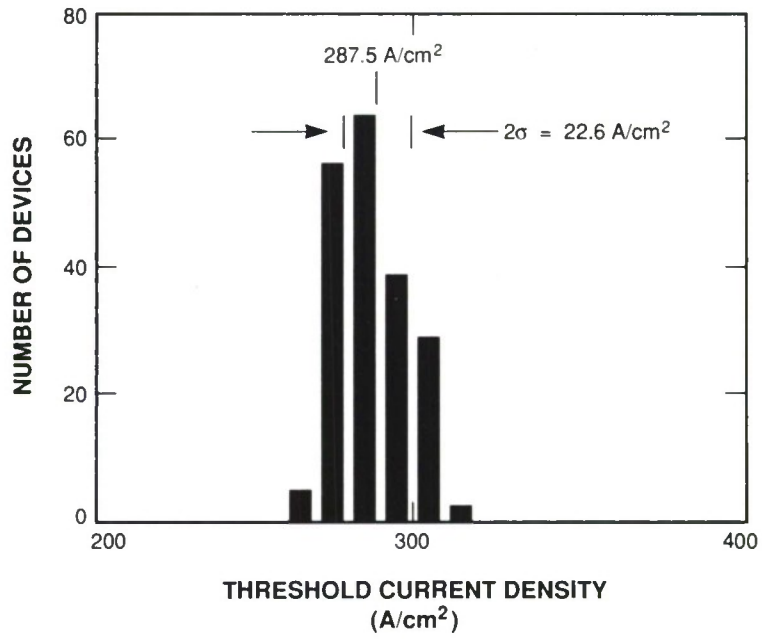
Figure 3-2. Distribution of threshold current density and differential quantum efficiency for 192 diode lasers.

35
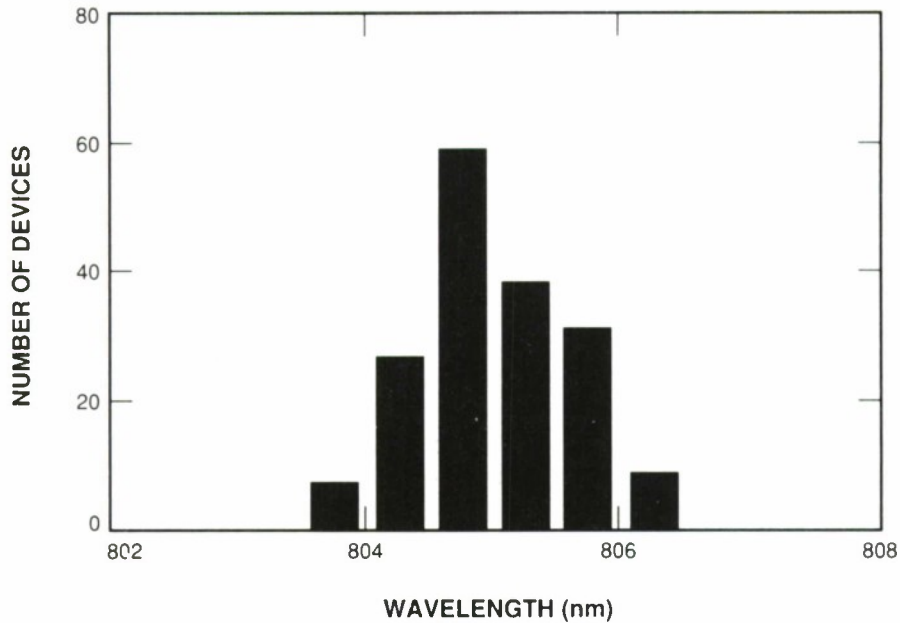
Figure 3-3.   Distribution of emission wavelength for 175 diode lasers.

3.2   128 × 128-ELEMENT IrSi SCHOTTKY-BARRIER FOCAL PLANE ARRAYS FOR LONG-WAVELENGTH INFRARED IMAGING

The operation of Schottky-barrier infrared detectors[3] is based on internal photoemission at the interface between a Si substrate and a thin silicide film. Imager arrays consisting of silicide detectors and the required readout circuitry are fabricated on Si wafers by standard integrated-circuit processing technology. The monolithic construction permits the manufacture of very large, extremely uniform arrays that operate in the staring mode. State-of-the-art Schottky-barrier arrays employ PtSi detectors,[4] which have a cutoff wavelength λ_c of ~ 6 μm, for imaging in the 3- to 5-μm wavelength band.

There is strong interest in extending the response of Schottky-barrier detectors and arrays into the long-wavelength infrared (LWIR) spectral band from 8 to 14 μm. Previous studies[5] have shown that IrSi detectors can have values of λ_c exceeding 6 μm. Improvements in processing techniques have recently led to reproducible fabrication of IrSi detectors with λ_c of ~ 10 μm (Reference 6). We report here fabrication and initial laboratory tests of 128 × 128-element focal plane arrays integrating IrSi detectors with $\lambda_c \sim 9.4$ μm and surface-channel CCD readout circuitry. In these tests thermal imaging with silicide arrays has been extended into the LWIR spectral band for the first time.

The IrSi imager arrays use the same architecture previously employed for PtSi arrays[7] that show excellent performance for thermal imaging in the 3- to 5-μm spectral band. Figure 3-4 is a schematic of a portion of the array. Each parallel CCD channel accepts charge packets from two

36
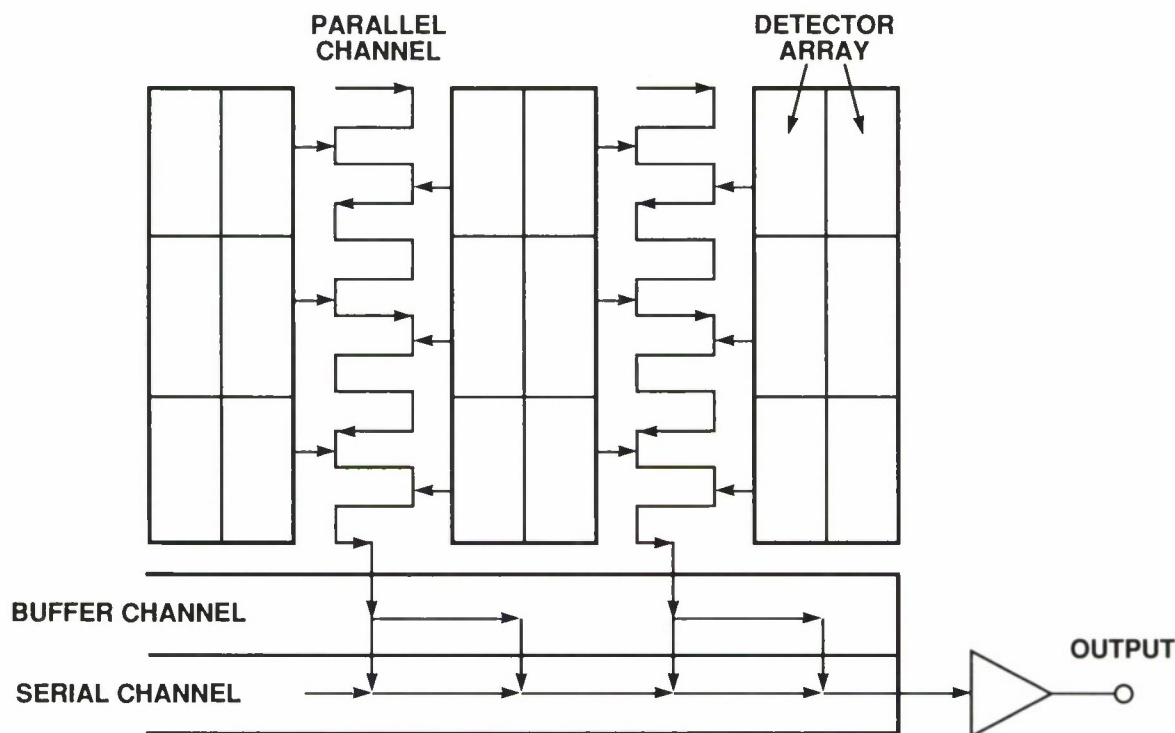
Figure 3-4. Schematic diagram of a portion of 128 × 128 IrSi array, showing column multiplexing of detector diodes in the parallel channel, subsequent demultiplexing in the buffer channel, and, finally, charge readout in the serial channel.

columns of IrSi detector diodes. The parallel CCDs are arranged in a four-phase meander configuration. The buffer channel is an extension of the parallel channel and is clocked with the same signals. Two charge packets are transferred into the buffer channel to reproduce the original row formation. The entire contents of the buffer channel (one row of detector charge) is then transferred into the serial channel, where it is transferred pixel by pixel to the output.

Figure 3-5 shows a schematic cross section of one pixel. Infrared radiation incident on the back side of the Si wafer is absorbed in the IrSi. The detector size is 29.5 × 48 μm and the pixel size is 52 × 52 μm, for a fill factor of 52 percent. This rather large fill factor is achieved by means of three unconventional design features.[7] First, the CCDs are surface-channel devices, which have higher charge storage capacity per unit area than conventional buried-channel CCDs. Second, using a meander configuration for the parallel channels eliminates extra clock bus lines and also allows readout of charge packets from two adjacent detector columns. Third, the field plate, which is part of an optical cavity structure[4] used for enhancing photon collection, is positively biased to suppress diode edge leakage,[8] thus eliminating the need for guard rings.

The CCD arrays were fabricated at Ford Aerospace by a double-polysilicon, single-metal process. The IrSi processing was carried out at Lincoln Laboratory by procedures reported previously.[6] Briefly, an Ir film 30 nm thick was deposited by electron-beam evaporation and IrSi

37
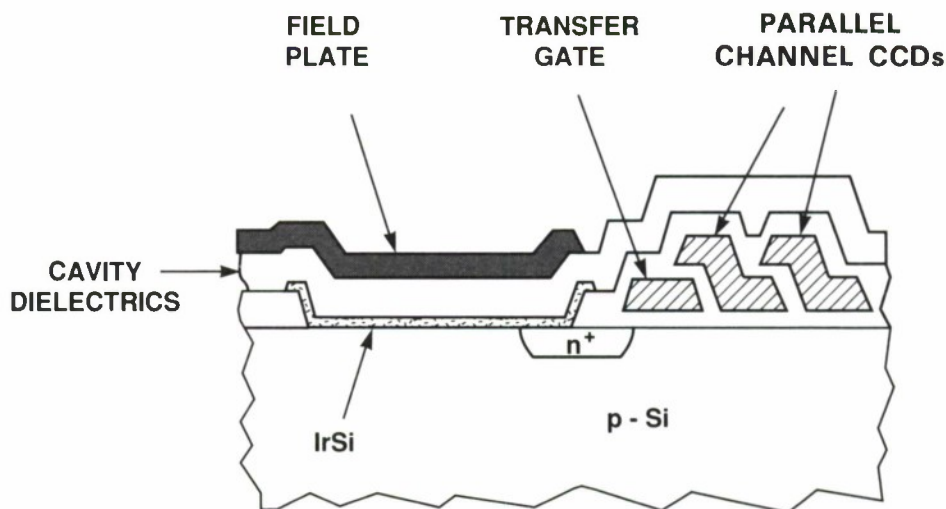
Figure 3-5. Schematic cross section of a single pixel of 128 × 128 IrSi array.

was formed by *in situ* vacuum annealing. Unreacted Ir outside the detector active area was subsequently removed by using a two-step reactive-ion-etching process.

The forward and reverse current-voltage characteristics have been measured between 40 and 100 K for large-area test detectors, $508 \times 508 \ \mu m^2$, that were fabricated on the same wafers as the imager arrays. These devices show ideal forward characteristics with near-unity diode factor. The reverse-current characteristics measured as a function of temperature follow the ideal thermionic-emission equation.[9] The Schottky-barrier height ψ has been determined by activation analysis[9] from the slope of plots of J/T^2 vs $1/T$, where J is reverse-current density and T is absolute temperature. A typical plot, based on the values of J measured at a reverse voltage of 1 V, is shown in Figure 3-6. The value of ψ obtained is 0.132 eV, corresponding to a cutoff wavelength of 9.4 μm.

A laboratory test system was used to evaluate performance of the 128 × 128 imager arrays. Each array was mounted on a leadless chip carrier and cooled to 50 K in a closed-cycle refrigeration system. Charge transfer efficiency of 0.9993 per gate was measured for the serial-channel CCDs operated at 0.5-MHz clock frequency with a "fat zero" (Reference 10) injection of 30 percent. This transfer efficiency is only slightly lower than the value of 0.9995 measured at room temperature. In contrast, conventional buried-channel CCDs usually suffer severe degradation in transfer efficiency at low temperatures because of carrier freezeout.[11]

Figures 3-7(a) and (b) are photographs of thermal images of a 10-K 4-bar test pattern and of human features, respectively, obtained with a standard one-point offset-type uniformity correction. The imager was operated at a frame rate of 30 Hz, with an f/1.6 cold shield and a 7.2-μm long-pass filter. The minimum resolvable temperature based on visual inspection of the 4-bar test pattern is about 0.3 K. The measured spatial nonuniformity of the uncorrected arrays for 298 K background is ~ 1.5 percent rms.
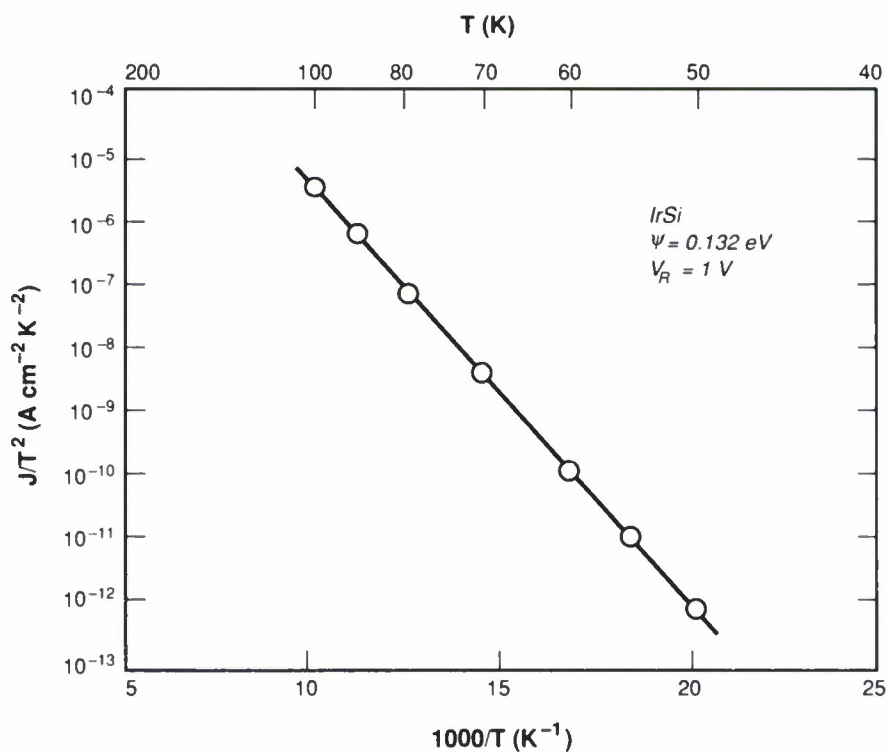
Figure 3-6. Plot of J/T^2 vs $1/T$ for IrSi detector operated at a reverse bias voltage of 1 V.
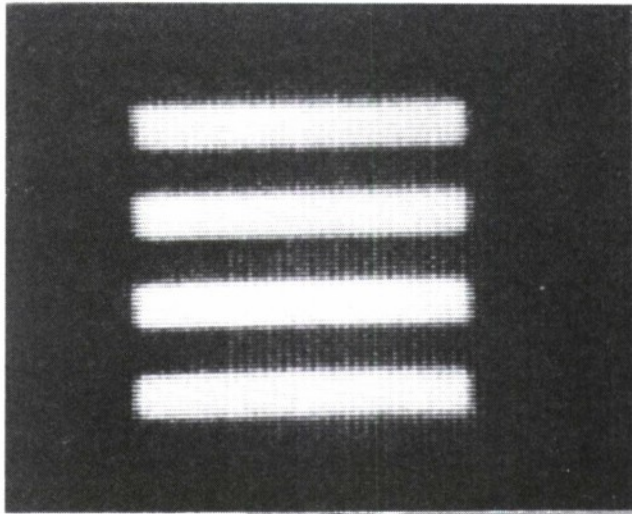
(a)

(b)

Figure 3-7.   Thermal images obtained with 128 × 128 IrSi imager array: (a) 10-K test pattern, (b) human features. The imager was operated with a 7.2-μm long-pass filter and a one-point offset-type uniformity correction was made.

40

The quantum efficiency Q of a Schottky-barrier detector, defined as the ratio of the number of electrons collected to the number of incident photons with energies exceeding the barrier height ψ, is related to the wavelength λ by the expression $Q(\lambda) = C_1 Q'(\lambda)$, where C_1 is the wavelength-independent emission coefficient and $Q'(eV) = [1.24/\lambda(\mu m)] [1 - \psi(eV)\lambda(\mu m)/1.24]^2$ (Reference 12). Thus, $C_1 = Q/Q'$. The value of C_1 for the detectors in an array was found by measuring the number of electrons collected per pixel when only 298-K background radiation was incident on the array, then taking the ratio of this number to the calculated number of electrons per pixel that would have been collected if the quantum efficiency were equal to Q'. Under the operating conditions described, the measured number was 3.13×10^5 electrons/pixel. The calculated number was found by integrating the product of Q' and the photon emission curve for a 298-K blackbody over the range from 7.2 μm, the filter cutoff wavelength, to 9.4 μm, the detector cutoff wavelength, and taking account of the frame rate and the parameters of the optical system. The value of C_1 obtained is 0.04 eV^{-1}, corresponding to a quantum efficiency of 0.014 percent at 8 μm. This C_1 value is much lower than the value of 0.096 eV^{-1} measured for individual IrSi detectors that we have fabricated previously,[4] presumably as a result of deficiencies in the IrSi processing for the arrays. The arrays are able to yield high-quality thermal imagery, in spite of their relatively low quantum efficiency, because of their excellent uniformity. Still better performance should be achieved by improving processing to increase detector cutoff wavelength and quantum efficiency, as well as by incorporating the arrays in an infrared camera to reduce noise.

B-Y. Tsaur
R.W. Mountain
R.F. Murphy, Jr.

REFERENCES

1. C.A. Wang, S. Patnaik, J.W. Caunt, and R.A. Brown, J. Cryst. Growth **93**, 228 (1988).

2. M. Druminski, R. Gessner, F. Kappeler, H. Westermeier, H-D. Wolf, and K-H. Zschauer, Jpn. J. Appl. Phys. **25**, L17 (1986).

3. F.D. Shepherd and A.C. Yang, in IEDM Tech. Dig., 1973, p. 310.

4. W.F. Kosonocky, F.V. Shallcross, T.S. Villani, and J.V. Groppe, IEEE Trans. Electron Devices **ED-32**, 1564 (1985).

5. P.W. Pellegrini, A. Golubovic, C.E. Ludington, and M.M. Weeks, in IEDM Tech. Dig., 1982, p. 157.

6. B-Y. Tsaur, M.M. Weeks, R. Trubiano, and P.W. Pellegrini, IEEE Electron Device Lett. **EDL-9**, 650 (1988).

7. M.J. McNutt, R.B. Mattson, and A.N. Vu, submitted to IEEE J. Solid-State Circuits.

8. M.J. McNutt, IEEE Electron Device Lett. **EDL-9**, 394 (1988).

9. S.M. Sze, *Physics of Semiconductor Devices*, 2nd edition (Wiley, New York, 1981), Chap. 5.

10. J.E. Carnes and W.F. Kosonocky, Appl. Phys. Lett. **20**, 261 (1972).

11. M. Kimata, M. Denda, N. Yurtani, N. Tsubouchi, and S. Uematsu, Jpn. J. Appl. Phys. **22**, 975 (1983).

12. V.L. Dalal, J. Appl. Phys. **42**, 2274 (1971).

4. SUBMICROMETER TECHNOLOGY

4.1 PLASMA DEPOSITION OF AMORPHOUS CARBON LAYERS FOR DRY RESIST AND PLANARIZATION APPLICATIONS

Films of amorphous carbon (a-C:H) have been plasma-deposited from organic precursors and used both as imaging and planarization materials. When used as an imaging layer, the carbon film is self-developed during exposure in an air ambient to 193-nm radiation from an ArF excimer laser, and a key requirement is the ability to pattern the layer with a low fluence of laser energy.[1] For the planarization application, sensitivity to light is not a requirement, but a film which smooths existing topography on the wafer and is easily etched [e.g., by reactive-ion etching (RIE)] is desired. A promising material for both applications is a-C:H.

The a-C:H was deposited under a variety of conditions. Substrates were placed on either the powered or grounded electrode of a parallel-plate RF plasma reactor. A variety of hydrocarbon source gases such as methane (CH_4), 1,3-butadiene (C_4H_6), and benzene (C_6H_6) were investigated. Other process variables included RF power (10 to 300 W), dc self-bias (V_{dc}) of the powered electrode (0 to 500 V), pressure (2 mTorr to 2 Torr), flow rate (10 to 100 scm^3/min), substrate temperature (25° to 350°C), and deposition time.

The a-C:H films were characterized with respect to their adhesion, deposition rate, index of refraction, etch rate during O_2 RIE, and self-development threshold E_{th} for pulsed 193-nm radiation. Adhesion was monitored by microscopically examining both patterned and unpatterned substrates for any cracking or peeling. Deposition rate was calculated from profilometer measurements of film thickness divided by run time. Index of refraction at 633-nm wavelength was measured using an automated ellipsometer. Oxygen etch-rate was calculated from profilometer measurements of etch craters after O_2 RIE performed at 250-V self-bias. Self-development thresholds for exposure to 193-nm pulsed laser radiation from an ArF excimer laser were extrapolated from plots of thickness of material removed per pulse vs fluence per pulse. The threshold fluence is the extrapolation of this curve to zero removal rate. The rate was measured by counting the number of pulses necessary to remove the entire film; this process was repeated over a range of pulse fluences. The laser pulses were ～ 15 ns in duration.

Films deposited on the grounded electrode were usually soft as determined by a scratch test. This is probably due to the low energy of ions bombarding the film during deposition. When reactive-ion etched in O_2, these films etch at a rate of over 500 Å/min, which is comparable to soft-baked Shipley AZ 1450J photoresist. Increasing the substrate temperature during deposition decreased the deposition rate but did not affect the O_2 etch rate.

Figure 4-1 shows some general trends observed for a-C:H deposited on a substrate placed on the powered electrode. The data shown are for films deposited from 1,3-butadiene at a flow rate of 25 scm^3/min and at a pressure of 20 mTorr, and serve as representative examples. As can be seen from the figure, E_{th} increases and O_2 etch rate decreases for films deposited under conditions of increasing V_{dc}. The energy of ions bombarding the film during growth increases with V_{dc}. The index of refraction varied from 1.7 to 2.1 with increasing V_{dc}, and an increase in depo-
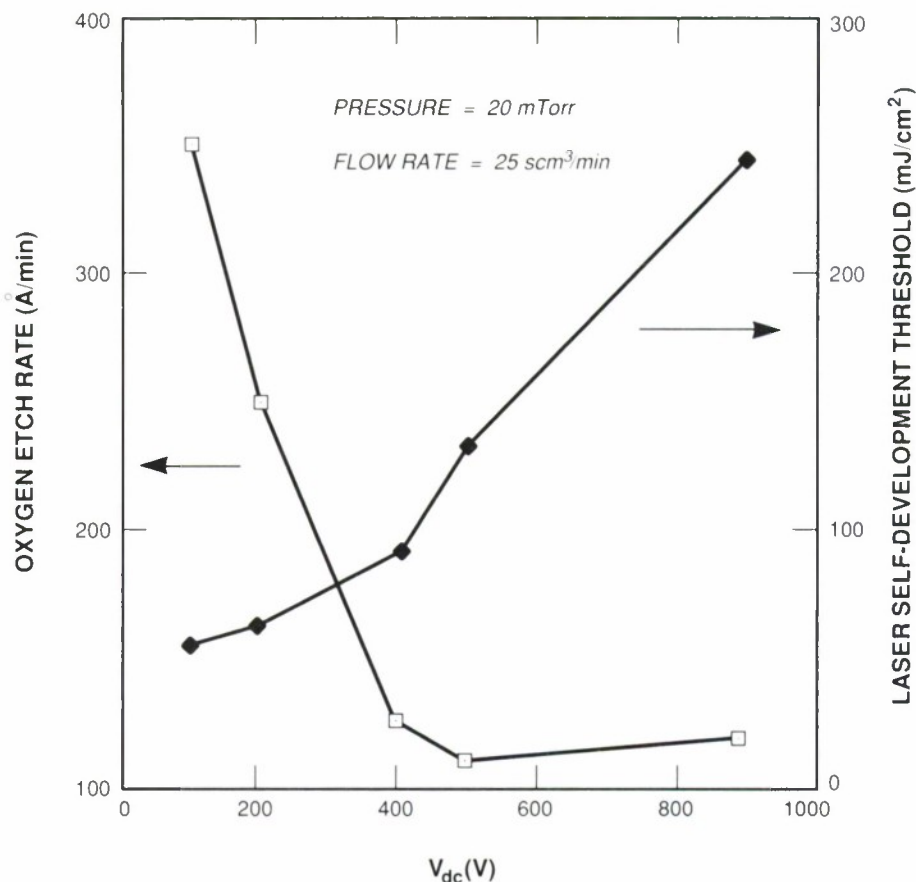
Figure 4-1.   Oxygen etch rate and laser self-development threshold as a function of dc self-bias (V_{dc}) for a-C:H films plasma deposited from 1,3-butadiene at a pressure of 20 mTorr and a flow rate of 25 scm^3/min.

sition rate due to the increasing RF power was also observed. In general we observed that films prepared with $V_{dc} > 200$ V exhibited poor adhesion on patterned substrates with $\sim$ 1-μm-high steps due to film stress induced by the energetic ion bombardment.

Figure 4-2 depicts the changes observed in deposition rate and E_{th} as a function of pressure for films deposited from 1,3-butadiene at a self-bias of 100 V and a flow rate of 25 scm^3/min. The residence time of the gas increases as the pressure increases. The longer residence time in the chamber and higher RF power needed to maintain the same self-bias may explain the higher deposition rates at higher pressures. The a-C:H deposited at higher pressures is softer and has a lower E_{th} and a lower index of refraction than material deposited at lower pressure.

Other workers[2] have found that hydrocarbons with larger molecular weights or larger carbon-to-hydrogen ratios (e. g., more double bonding) deposit at higher rates. We deposited films using three different hydrocarbons with progressively increasing carbon/hydrogen ratios and
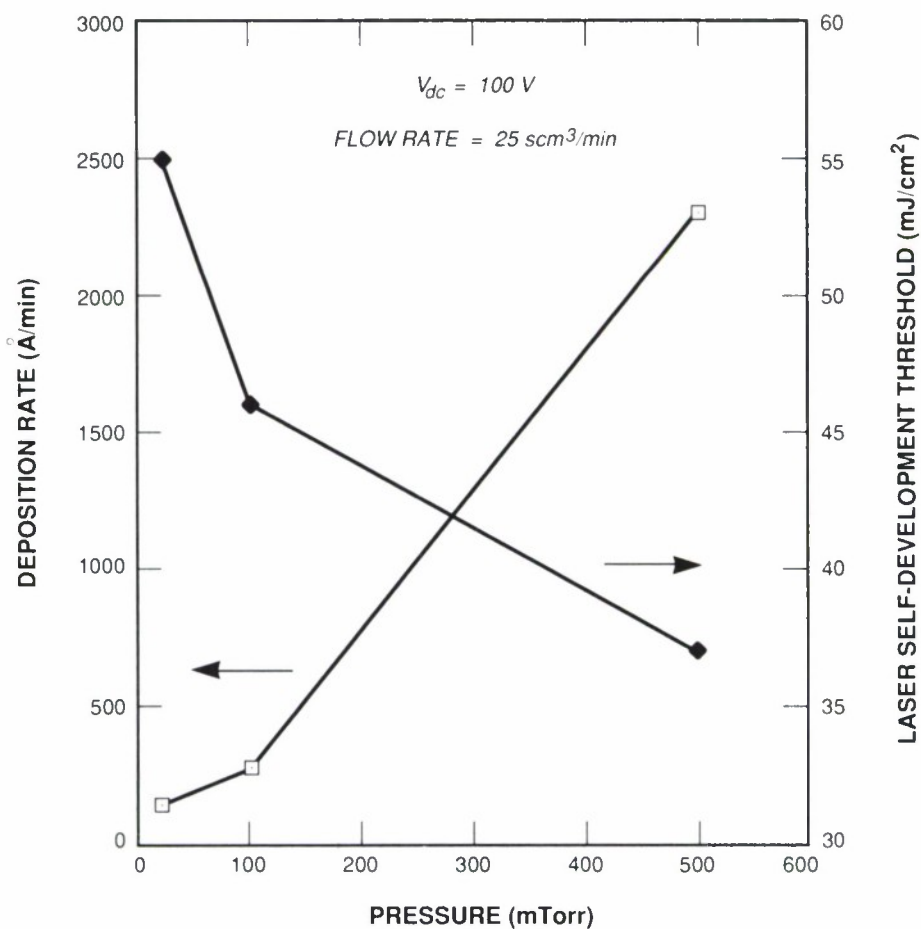
Figure 4-2. Deposition rate and laser self-development threshold as a function of pressure for a-C:H films plasma deposited from 1,3-butadiene at a dc self-bias of 100 V and a flow rate of 25 scm³/min.
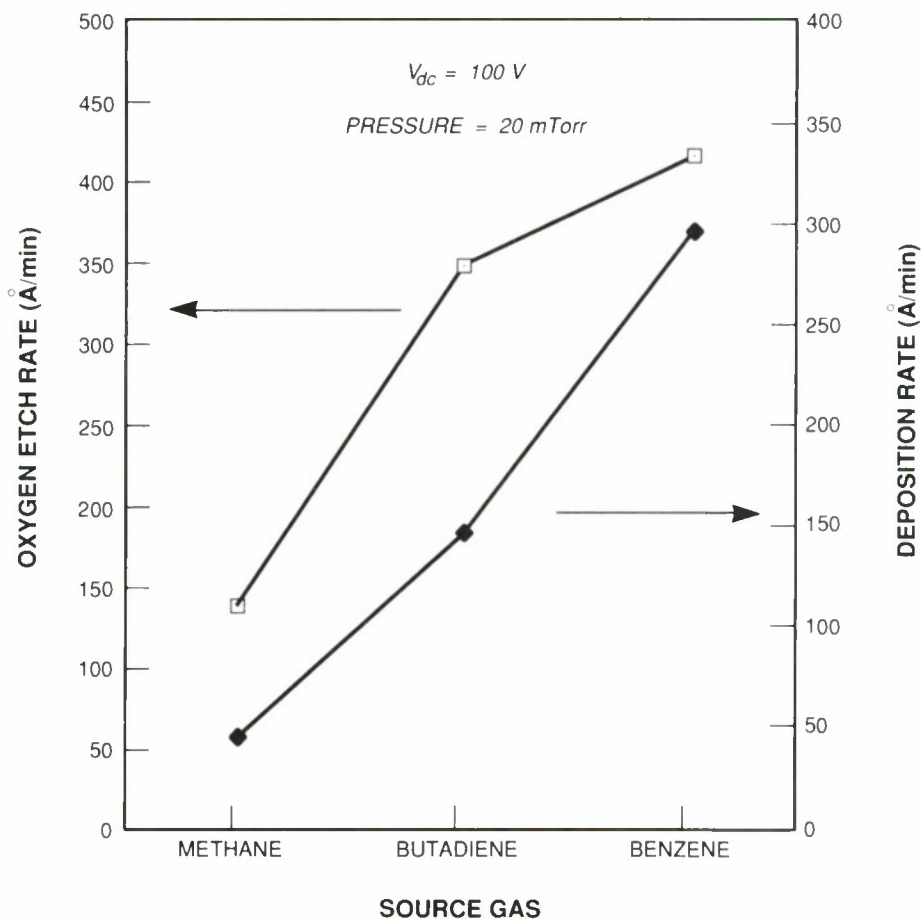
Figure 4-3. Oxygen etch rate and deposition rate for a-C:H films plasma deposited from three different source gases at a dc self-bias of 100 V and a pressure of 20 mTorr.

increasing molecular weights, expecting considerable differences in the growth rate. At higher growth rates the films would be expected to receive less ion bombardment, with corresponding changes in their properties. Figure 4-3 shows the trends exhibited as the saturation and molecular weight of the hydrocarbon molecule were varied. The runs using methane, 1,3-butadiene, and benzene shown in the figure were all made at similar flow rates, at a pressure of 20 mTorr, and at 100-V self-bias. Note that the O_2 etch rate and the deposition rate both increase as saturation decreases and molecular weight increases.

Earlier work has shown that amorphous carbon can be patterned with 0.25-μm-period gratings[3] using 193-nm-wavelength excimer laser projection lithography at pulse fluences of 0.1 to 1 J/cm^{2} per pulse. We have shown that the threshold fluence can be varied by varying the plasma deposition conditions.

<div align="right">

M.W. Horn
S.W. Pang
R.R. Kunz

</div>

4.2 LASER-DIRECT-WRITE REPAIR OF DIGITAL INTEGRATED CIRCUITS

The development of new microcircuits for VLSI systems is often an iterative process. After the initial specification and layout of a chip, the design is verified by simulation using software running on a general-purpose computer. When the simulation results agree with the performance specification, the design is submitted to a silicon foundry (e.g., MOSIS) for fabrication. After a typical two- to three-month delay, an actual circuit is delivered for testing. Frequently, a number of minor design errors are uncovered during testing, which may result from deficiencies in the simulation, from the inability to run a complete simulation in a reasonable time, or from conceptual problems with the initial specification. In any event, the chip must be resubmitted for fabrication, resulting in a long delay. For particularly complex systems, several iterations may be required.

Recently, we have begun to apply our expertise in laser-direct-write techniques to making small modifications to digital CMOS circuits, used as components of wafer-scale systems, which have minor, but fatal, design flaws. Three separate operations are possible, with the process details depending upon the materials and geometries encountered. First, polysilicon and aluminum lines can be severed by either excimer- or argon-ion-laser cutting. Second, holes through the passivation and intermetal dielectric layers can be opened by excimer-laser ablation. Finally, new interconnections can be directly deposited using polysilicon degenerately doped with boron.

Where necessary, passivation layers were removed by using 193-nm-wavelength, 15-ns-duration pulses from an ArF excimer laser, focused by reflective optics to a 5- to 10-μm-diam. spot. The cutting of conductors was performed using two different laser systems. Large (> 5-μm width) metal and polysilicon lines could be cut by 193-nm laser ablation. Smaller metal and polysilicon features were more easily cut by thermal melt-back using 488-nm CW radiation from an argon-ion laser, mechanically shuttered to give 10- to 100-ms pulses. The excimer ablative cutting was accomplished at a pulse fluence on the order of 1 J/cm^2, while the visible-laser cutting required $\sim 10^6$ W/cm^2. Opening of vias was also performed by excimer ablation, using parameters similar to those used for cutting.

The writing of conductors was performed using pyrolytic direct-write deposition of degenerately p$^+$-doped polysilicon. A 400-Torr, 9:1 SiH$_4$:B$_2$H$_6$ mixture was pyrolyzed at the 2-μm-diam. focus of a 488-nm argon-ion laser beam with a power of ~ 1 W. This process was chosen because of the excellent adhesion of the polysilicon to the PSG passivation layer. With typical linewidths of 4 μm, a relatively high resistance is obtained (200 Ω/mm), but this is generally sufficiently conductive to allow functioning of the chip, albeit at reduced clock rates. The conductivity can be enhanced by 35 to 1000 percent by selective cladding with tungsten in a subsequent process step. To date, direct metal deposition processes have not matched the speed obtainable with polysilicon deposition and have not provided the adhesion to glass required for this repair application.

Over the past few months, several chips have been successfully repaired and we have developed guidelines for the practical limits of the current process. An example of a repaired chip is shown in Figure 4-4. Contact openings can be made to either polysilicon or metal layers with
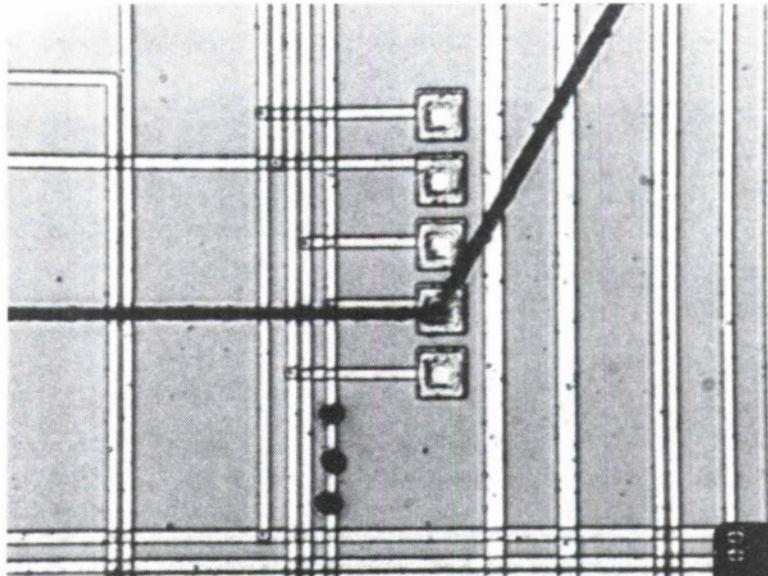
(a)
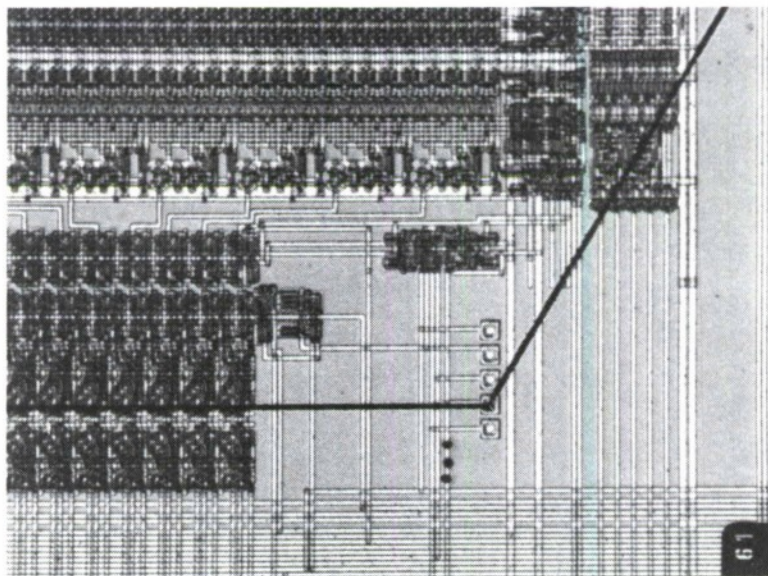
(b)

Figure 4-4. (a) Region of CMOS cell (memory fetch buffer) where an incorrectly placed line was cut (three black dots) and reconnection (horizontal and diagonal lines) with p^+ polysilicon was performed by laser-direct-writing. (b) A large-area view showing that the interconnect can be written over distances of several millimeters.

48

sizes ranging from 2 to 100 μm square. A separation of about 2 μm between the edge of the via and the nearest feature is necessary. Lines from 4- to 100-μm width can be cut if the cuts can be placed at least 5 μm from other circuit features. Directly written interconnections are typically 5 to 10 μm wide and can be written with any pitch of >15 μm. A resistance of $\leqslant 200$ Ω/mm and a contact resistance of < 1 Ω can be expected.

The repair procedure can often be accomplished in less than an hour, given appropriate defect information and equipment availability. The actual time to achieve the disconnections and reconnections is measured in seconds; sample handling and setup represent the largest delays. In difficult cases, trial runs may be necessary to ensure that satisfactory repairs are achieved. Nonetheless, the turnaround time for circuit development can be shortened by months with a session of laser processing which can be done in an afternoon. This capability has already been used to speed the development of complex wafer-scale architectures under development at the Laboratory. This work also exemplifies the flexibility of laser-direct-write processing; arbitrary disconnections and reconnections can be made on circuits with no prior provision for laser processing.

<div align="right">
J.G. Black
S.P. Doran
</div>

REFERENCES

1. M. Rothschild and D.J. Ehrlich, J. Vac. Sci. Technol. B **6**, 1 (1988).

2. J.C. Angus, P. Koidl, and S. Domitz, in *Plasma Deposited Thin Films*, edited by J. Mort and F. Jansen (CRC Press, Boca Raton, Fla., 1986), pp. 89-126.

3. M. Rothschild and D.J. Ehrlich, J. Vac. Sci. Technol. B **5**, 389 (1987).

5. MICROELECTRONICS

5.1 THE EFFECT OF DOPING-PROFILE VARIATIONS ON THE COLLECTOR-BIAS DEPENDENCE OF f_T FOR THE Si PBT

CANDE, a two-dimensional simulation program, has been used to calculate the small-signal unity-current-gain frequency f_T as a function of collector bias for two etched-emitter Si permeable base transistors (PBTs) with different vertical doping profiles. Here f_T is defined as $g_m/2\pi C_{TOT}$, where g_m is the transconductance and C_{TOT} is the total device capacitance of the base terminal. As shown in Figure 5-1 for a uniformly doped (4×10^{16} cm^{-3}) PBT, the f_T reaches a maximum (32 GHz) at a collector bias of 5 V and decreases significantly for larger collector biases. By contrast, the asymmetrically doped profile (highly doped emitter, lightly doped collector) shows an f_T that is nearly independent of collector bias. In addition, the breakdown voltage V_B of the asymmetrically doped device is nearly 50 percent higher. Because the f_T V_B product of the asymmetrically doped device is nearly twice that of the uniformly doped device, significant advantages are anticipated for large-signal operation.
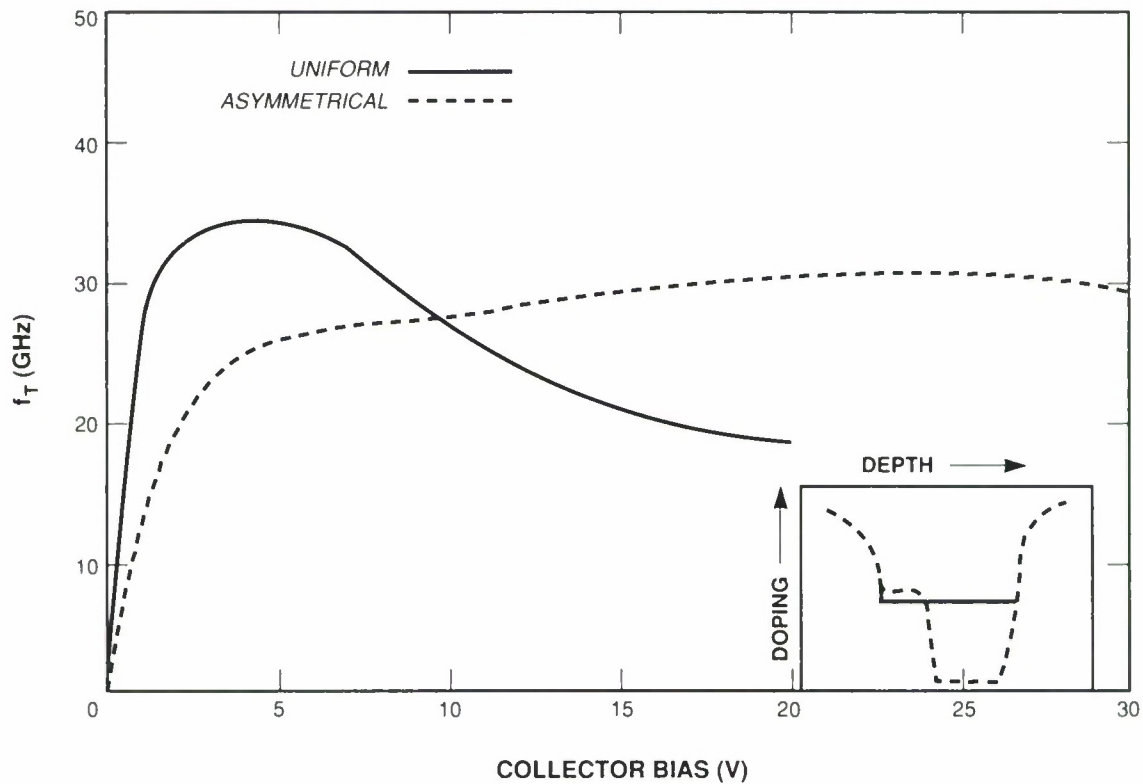
Figure 5-1. Dependence of f_T on collector bias for a uniformly doped and a highly asymmetrically doped etched-emitter Si PBT. The doping profiles are shown schematically in the inset. Emitter doping level is ~ 100 times that of the collector doping for the asymmetrically doped device.

The dependence of f_T on collector bias can be explained from transit-time arguments as follows. The uniformly doped PBT is similar in operation to a vertical FET where the effective channel length L_{eff} of the device is determined by the length of the control region of the device. For the uniformly doped PBT, this length is identical to the physical extent of the high field region of the device (see Figure 5-2). The effective channel length also corresponds, approximately, to the length of the depletion channel region as shown in Figure 5-3. Because this length increases with collector bias, the transit time increases and f_T decreases. If one approximates L_{eff} in this manner and assumes that the average velocity for electrons in Si is equal to 1×10^7 cm/s, very good agreement with the calculated f_Ts can be obtained from the following relations:

$$\frac{L_{eff}}{v_{avg}} = \tau \quad \text{and} \quad f_T = \frac{1}{2\pi\tau} \quad .$$
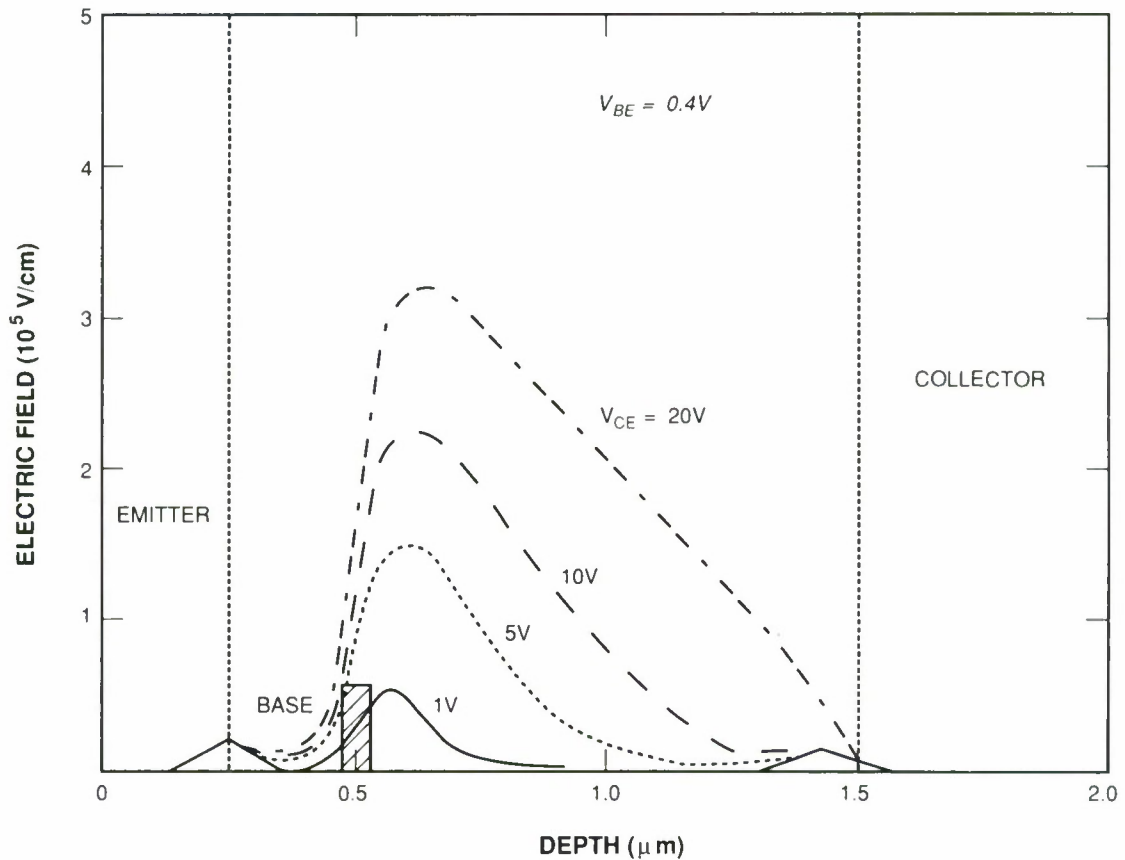
Figure 5-2. Electric field magnitude along the channel center for the uniformly doped Si PBT for different collector-to-emitter biases.

52

119340-23
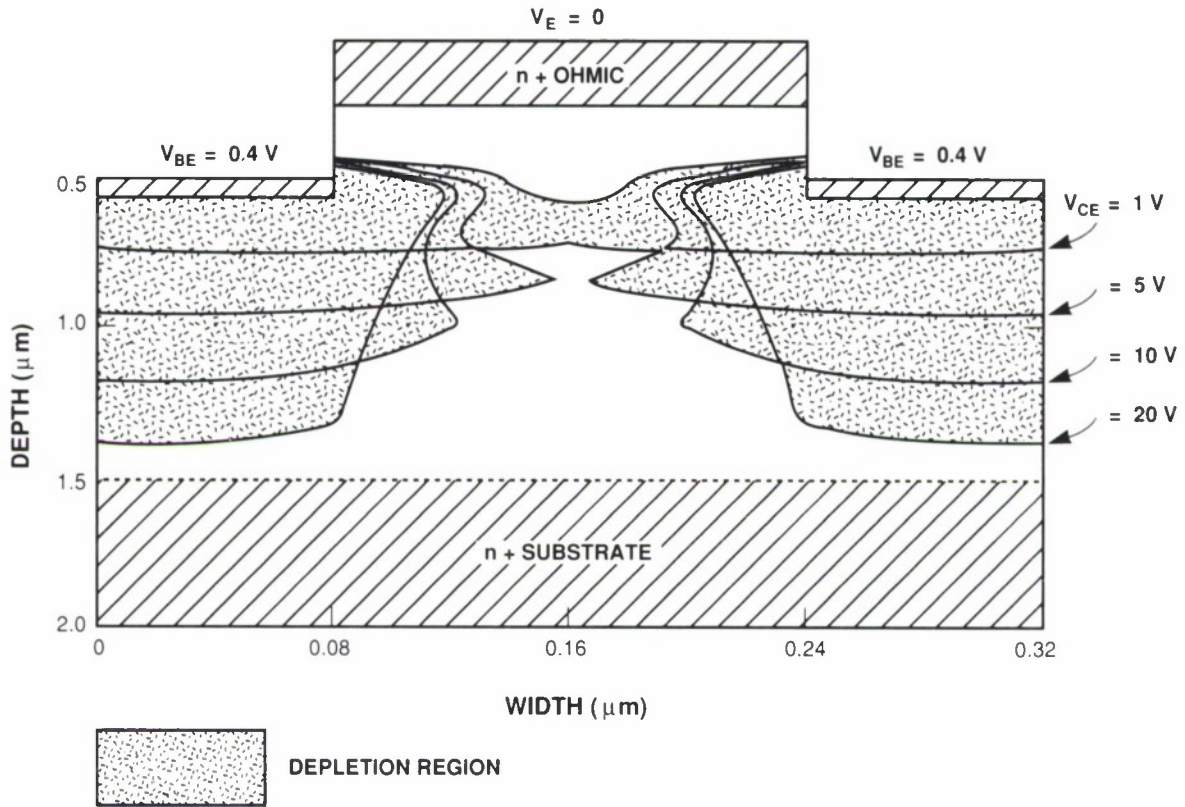
Figure 5-3. Depletion region for the uniformly doped Si PBT for the same collector-to-emitter biases of Figure 5-2.

For the asymmetrically doped PBT, the physical extent of the high electric field region (Figure 5-4) extends from the base electrode to the collector contact and is independent of collector bias. In addition, the depletion region between adjacent base electrodes (Figure 5-5) does not change significantly with collector bias. This is consistent with the fact that the effective transit time, and therefore f_T, is independent of collector bias. The reason for this behavior is related to the formation of a large negative space charge in the collector body, which can be observed from the plots of electron concentration vs depth in Figure 5-6. This space charge, whose magnitude is determined by both the emitter doping level and the applied voltage, prevents the control region (approximately equal to the depletion region) from expanding with increasing collector bias.

The effective transit time for this device actually is a sum of the delay times for transit through the control region and for transport through the space charge or drift region. The delay associated with transit through the space charge is half the transit time for the individual carriers. This is a consequence of the induction of charge on the base and collector electrodes by the charge in transit and is identical to the effect noted in the transport of charge through the collector depletion layer of bipolar transistors. If one approximates L_{eff} as the control-region length

plus one-half the space-charge region extent in the above equations, good agreement with the calculated f_T curves of Figure 5-1 is obtained.

D.D. Rathman
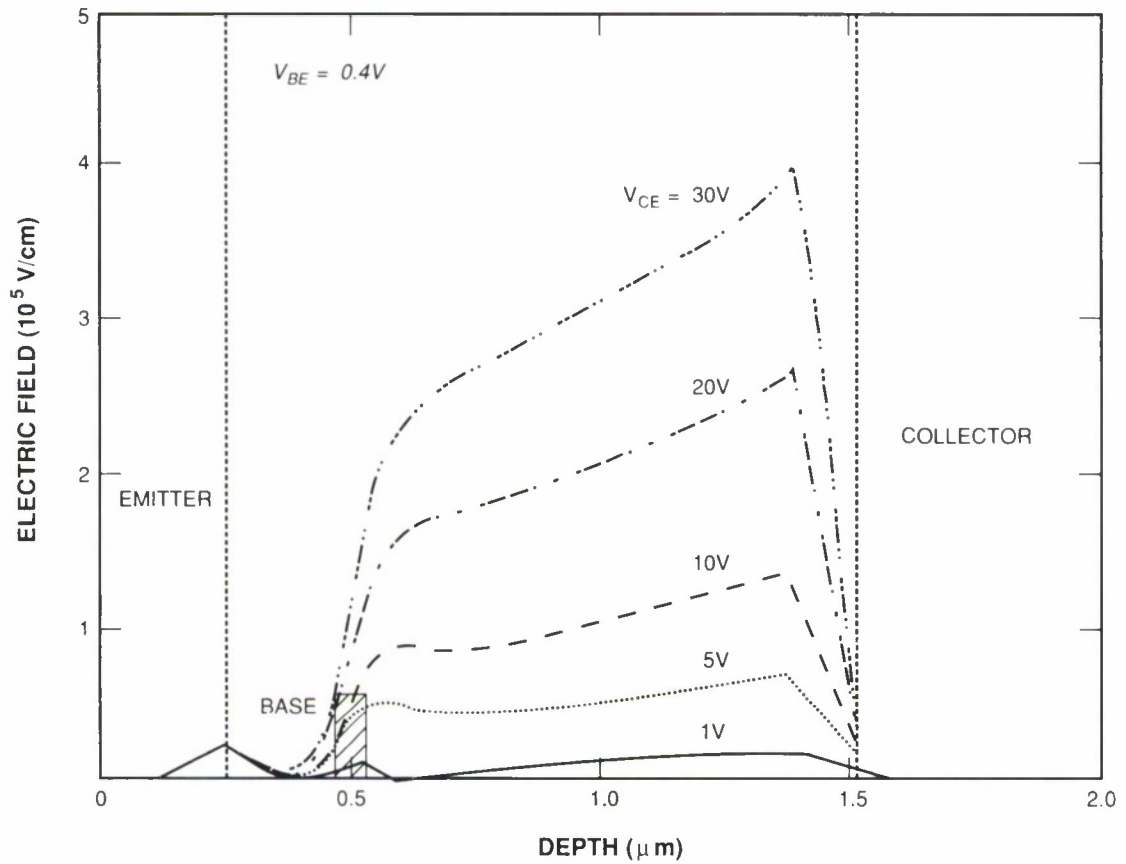
Figure 5-4. *Electric field magnitude along the channel center for the asymmetrically doped Si PBT for different collector-to-emitter biases.*

Figure 5-5.   Depletion region for the asymmetrically doped Si PBT for the same collector-to-emitter biases of Figure 5-4.
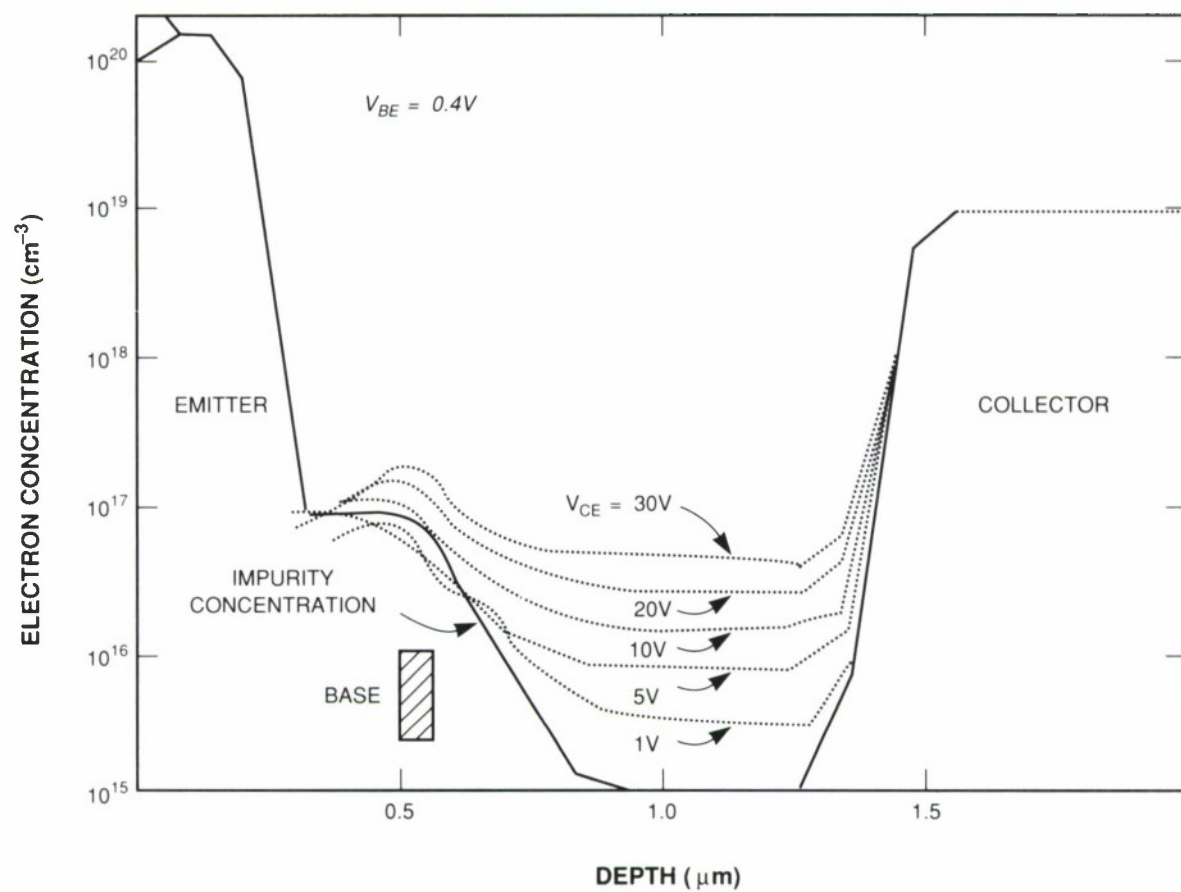
Figure 5-6. Electron concentration along the channel center for the asymmetrically doped Si PBT for the same collector-to-emitter biases of Figure 5-4. Also indicated is the background impurity concentration.

5.2 LARGE-SIGNAL CHARACTERIZATION OF MILLIMETER-WAVE TRANSISTORS USING AN ACTIVE LOAD-PULL MEASUREMENT SYSTEM

A comprehensive characterization of the large-signal properties of high-speed transistors is indispensable for the development of efficient solid state power sources at millimeter-wave frequencies. Here we describe a measurement system that addresses this requirement at extremely high frequencies (EHF). This method has been applied to the GaAs PBT in the frequency band from 33 to 50 GHz and has been verified with the design of a prototype amplifier at 40.1 GHz.

The measurement system employs an "active" load-pull concept[1] in which a variable load termination is presented at the transistor output port and the corresponding power into the load is measured. Unlike conventional load-pull measurements employing circuit tuners, this method induces an "equivalent" output load termination by the boundary conditions between incident and reflected power waves at the transistor output port. Consequently, the measurement does not suffer the large inaccuracies that can result from tuner circuit losses at EHF.

Figure 5-7 shows the block diagram of the active load-pull system. Two reflectometers are positioned at the input and output ports of the active PBT transistor to measure the corresponding terminating impedances. The amplitude and phase of a second injected signal P_2 at the output port of the transistor, applied simultaneously with the conventional input drive signal, establishes the power wave boundary conditions corresponding to an equivalent output load impedance. The device output power P_{out}, bias, and terminating impedances are adjusted and monitored by a controller which calculates the resulting gain and efficiency.

This system has been used to characterize the large-signal performance of an 8×20-μm PBT fabricated on a semi-insulating GaAs substrate. Figure 5-8 illustrates the EHF test fixture in which the device was mounted for measurement. The fixture uses wideband MIC-to-waveguide transitions which typically exhibit a minimum input return loss of 15 dB and a maximum back-to-back insertion loss of 1.25 dB in the frequency band from 34 to 48 GHz. The packaging of the device is similar to that described in Reference 2.

The constant output power contours for a fixed frequency and input power level are shown in Figure 5-9 (solid curves). The constant P_2 contours (dashed curves) indicate ranges of output impedances achieved by varying the relative phase between two incident powers. An input matching network was used to maximize the power delivered to the device. The input return loss associated with this matching network is shown in the inset. The data points were generated automatically by utilizing algorithms designed to induce selected regions of output load impedances. Results of the characterization are tabulated in Table 5-1. An output power of 30 mW with 3 dB of associated gain and 12.8-percent power-added efficiency was predicted.

Data from large-signal characterization were applied to the design of a moderate-power PBT amplifier at 40 GHz. The device structure was not optimized for power applications. Narrowband impedance-matching networks were designed and fabricated on a 250-μm alumina MIC substrate. The output power and associated gain with circuit losses removed are shown in Figure 5-10. Approximately 27 mW of output power with 2.6-dB associated gain was measured at 40.1 GHz.
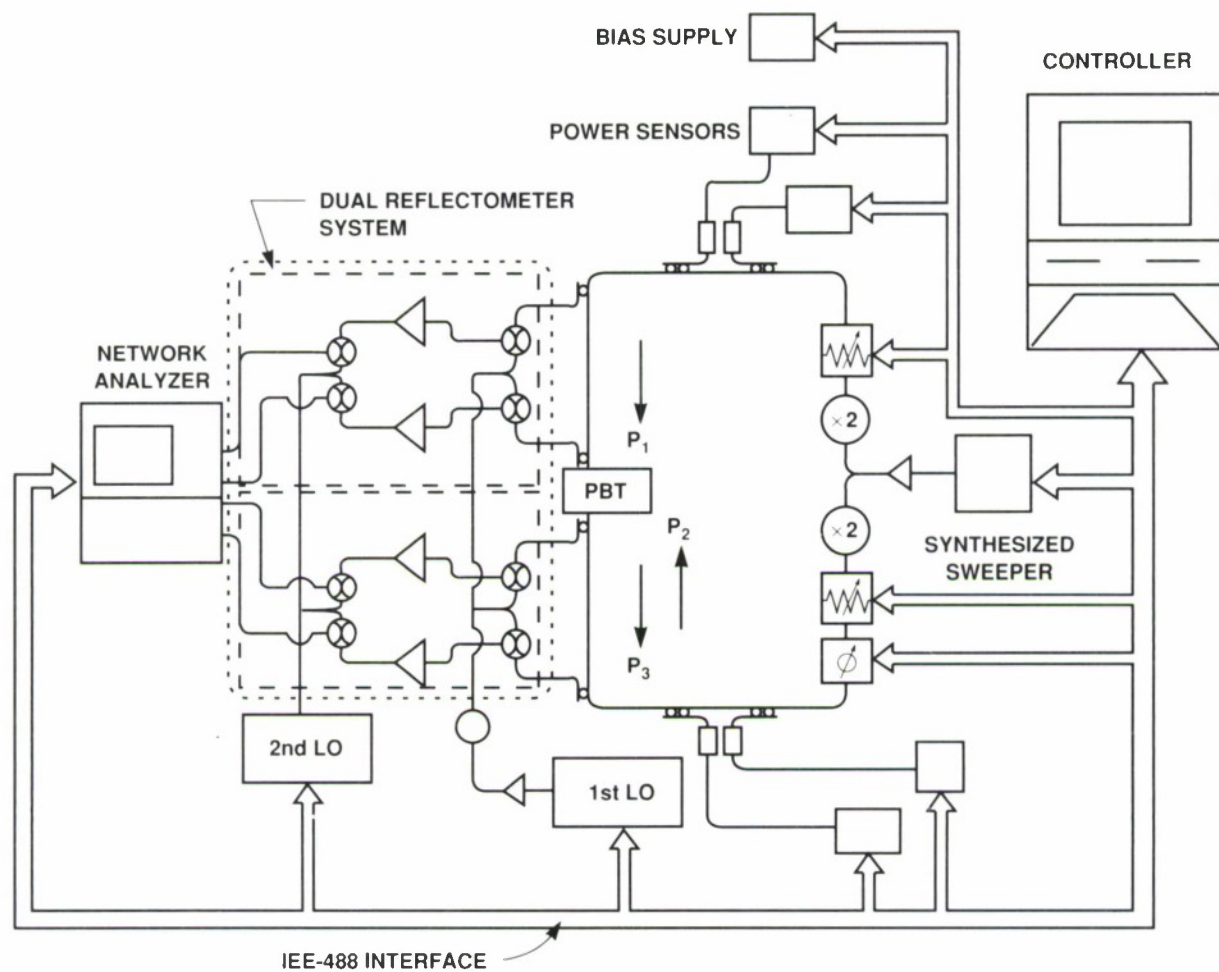
Figure 5-7.   *Block diagram of the EHF active load-pull measurement system.*

58

The power-added efficiency was 12 percent. This result is in good agreement with the load-pull prediction of 30 mW with 3 dB of gain and 12.8-percent power-added efficiency.

Additional measurements for a more optimal efficiency of another device from this same wafer have resulted in 16.8-percent power-added efficiency with a gain of 2.8 dB and 14.5 mW of output power at 40 GHz.

R. Actis   R.W. Chick
R.A. McMorran   C.O. Bozler
R.A. Murphy   K.B. Nichols
M.A. Hollis
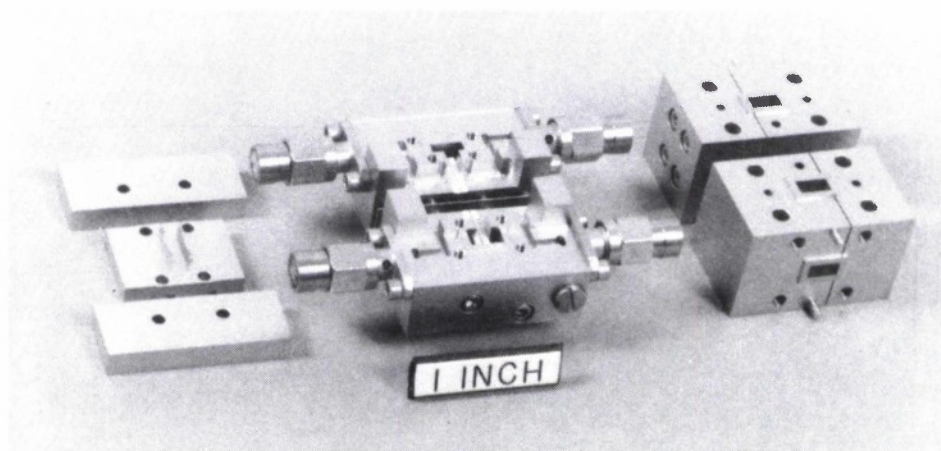
Figure 5-8.   EHF test fixture used for testing the PBT.

59
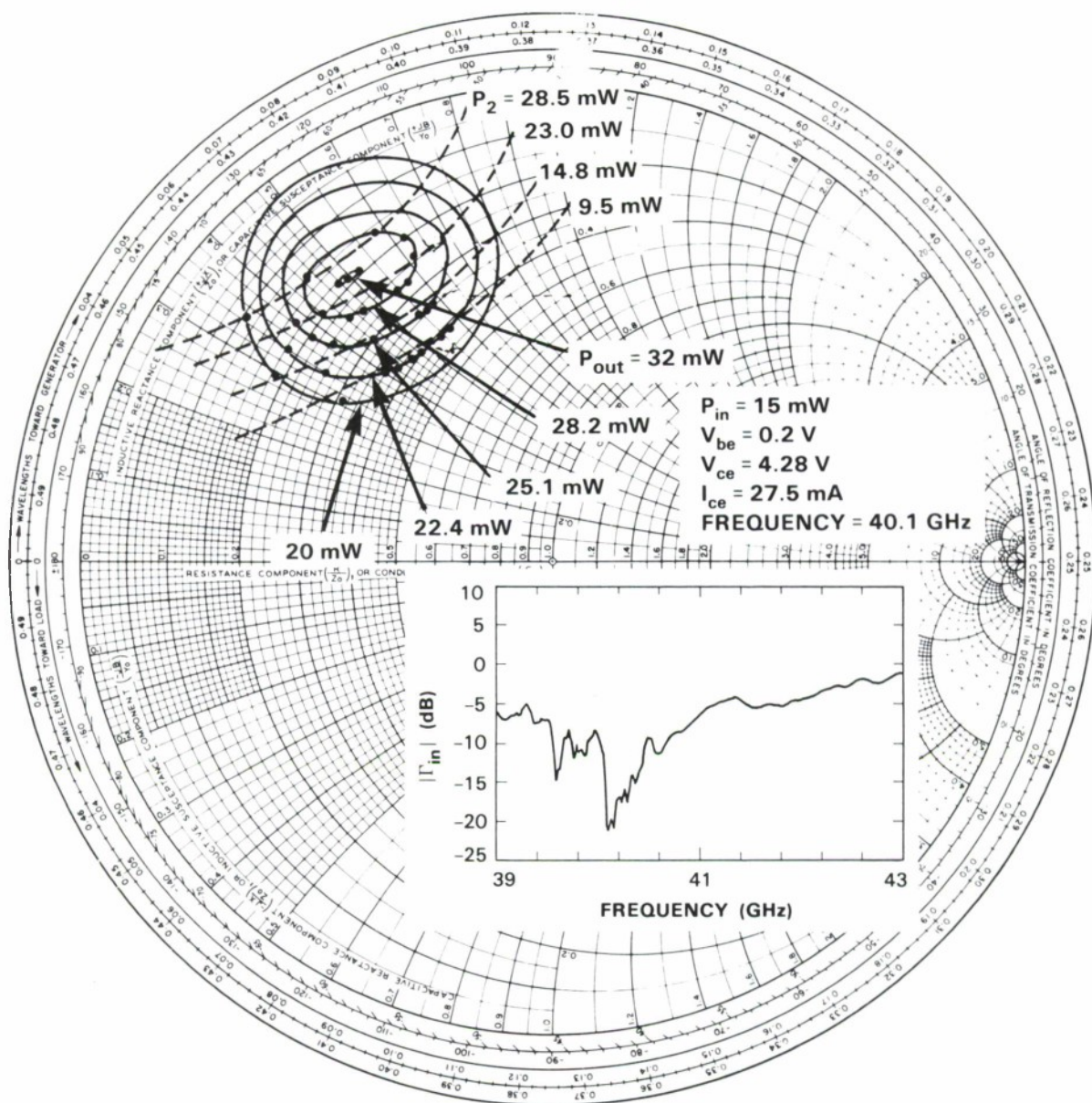
Figure 5-9.   Load-pull measurement data in the output-impedance plane. Contours (solid lines) of constant output power at 40.1 GHz and 15 mW input drive are shown for an 8 × 20-μm PBT. The constant P_2 contours (dashed curves) indicate ranges of output impedances achieved by varying the relative phase between the two incident powers. The reflection coefficient magnitude associated with the input matching network is shown in the inset.

60

TABLE 5-1								
Results from Active Load-Pull Characterization of an $8 \times 20\text{-}\mu m$ PBT								
P_{in} (mW)	Gain (dB)	P_{out} (mW)	V_{ce} (V)	I_{ce} (mA)	V_{be} (V)	P_{dc} (mW)	Power-Added Efficiency	Collector Efficiency
3.92	6.08	15.89	3.43	47.9	0.88	164.3	7.3%	9.7%
4.92	5.66	18.11	3.90	41.8	0.60	163.1	8.1%	11.1%
6.24	4.84	19.01	3.91	41.8	0.65	163.5	7.8%	11.6%
8.00	3.76	19.01	3.75	36.1	0.42	135.3	8.1%	14.0%
10.02	3.41	21.96	4.08	30.7	0.28	125.2	9.5%	17.6%
12.39	3.24	26.12	4.22	29.7	0.25	125.3	11.0%	20.9%
15.38	2.96	30.41	4.33	27.2	0.19	117.8	12.8%	25.8%
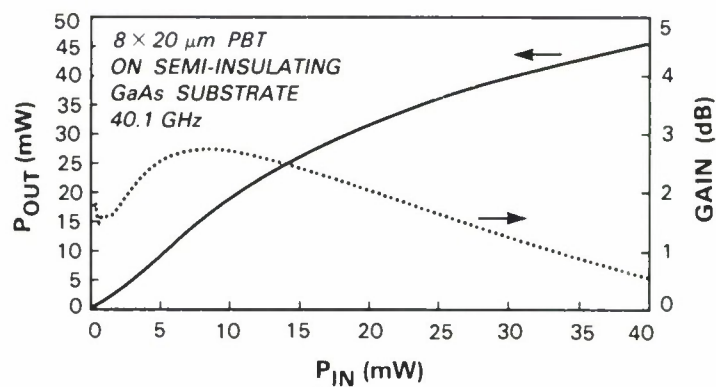
Figure 5-10. Measured gain and output power of the prototype PBT amplifier. Circuit losses have been removed from the data.

119340-31

5.3 OXIDE IMPROVEMENT USING EXPERIMENTAL DESIGN

Stress testing of some Al-gate MOS capacitors under negative applied bias and at an elevated temperature resulted in a shift of the flat-band voltage V_{FB} by 2 or 3 V in the negative direction. This shift, which is called negative bias-temperature instability (NBTI), was observed for oxides grown in a new cantilever-based furnace system and is accompanied by an increase in interfacial state density. Although the NBTI and increased state density were not observed using standard polysilicon gates, removal of these effects was considered desirable.

With the traditional approach of varying one process parameter at a time, no clear trend in reduction of NBTI was apparent. Therefore, an experiment was designed to determine systematically which factors would minimize it. Eight factors were included in a linear model to generate a matrix of process conditions and runs. These conditions included trichlorethane (TCA) cleaning of the oxidation tube before insertion of the samples, temperature ramp-up and ramp-down rate, oxidation temperature, oxygen flow, TCA flow during oxidation, and annealing time after oxidation. All oxidations were performed in dry $O_2$ with TCA added for some runs, and N_2 was used as a purge gas. Including replicates and test points, the linear model required only 19 experimental runs. The results of this round of matrix testing indicated that the induced charge would be minimized by using the following conditions:

TCA clean	No
TCA clean temperature	N/A
Temperature ramp-up	5°C/min
Oxidation temperature	1000°C
TCA flow	No
O_2 flow	5 l/min
N_2 annealing time	30 min
Temperature ramp-down	5°C/min

The model also predicted that the shift in V_{FB} would be decreased by a factor of 10, that is, to −0.2 or −0.3 V. Implementation of these conditions reduced the shift in V_{FB} only by a factor of 3 to about −0.9 V, suggesting that the linear model used in the matrix was not strictly correct. The matrix did, however, result in a larger improvement than was achieved by varying one factor at a time in previous oxidation experiments. A second matrix of conditions was generated, contrasting dry and wet oxidation and lowering both the oxidation temperature and the O_2 flow rate further. The results of this second matrix of seven runs suggested that the V_{FB} shift could be lowered by another factor of 3 by continuing to use dry oxidation, but with an oxidation temperature of 950°C and an O_2 flow rate of 4 l/min. These conditions will be tested.

In summary, the results of one round of experiments has allowed the shift in V_{FB} to be decreased a factor of 3 in MOS structures and a second round has suggested conditions that will reduce this shift even further.

<div style="text-align: right">

J.A. Gregory
R.W. Mountain
C.L. Doherty

</div>

REFERENCES

1. Y. Takayama, in *Proc. IEEE G-MTT International Microwave Symp.* (1976), pp. 218-220.

2. R. Actis, R.W. Chick, M.A. Hollis, B.J. Clifton, K.B. Nichols, and C.O. Bozler, IEEE Electron Device Lett. **EDL-8,** 66 (1987).

6. ANALOG DEVICE TECHNOLOGY

6.1 PATTERNING OF SUPERCONDUCTING YBa$_2$Cu$_3$O$_x$ THIN FILMS

Superconducting YBa$_2$Cu$_3$O$_x$ thin films with zero-resistance transition temperature of 90 K have been deposited on yttria-stabilized zirconium oxide substrates by sequential RF diode sputtering from Y$_2$O$_3$, BaF$_2$ and CuO targets.[1] For the fabrication of microwave devices employing YBa$_2$Cu$_3$O$_x$ thin films, it is necessary to develop a technique for patterning these films. As the superconducting properties of YBa$_2$Cu$_3$O$_x$ films deteriorate after exposure to water, wet etching in dilute acids is not desirable. Dry etching processes such as reactive-ion etching in Cl$_2$ gas and ion-beam milling have been reported recently.[2,3]

We have developed a patterning process using either a positive or a negative photoresist for line definition followed by ion-beam milling. The film surface is sufficiently smooth to clearly define linewidths of 5 μm. The film is removed at the rate of 33 nm/min by ion-beam milling in an Ar+ beam. In order to prevent the resist from reacting with the film during ion-beam milling, the sample is attached to a water-cooled table with the help of thermal grease to keep its temperature from rising above ~100°C.

A scanning electron micrograph of a 10-μm-wide line is shown in Figure 6-1. The film was 1 μm in thickness. The surface morphology as seen in the micrograph (micrometer-size crystallites on a smooth background) is typical of the YBa$_2$Cu$_3$O$_x$ thin films deposited by this process. The transition temperature of a YBa$_2$Cu$_3$O$_x$ film before and after patterning a 40-μm-wide line is shown Figure 6-2. A small tail in the resistance vs temperature curve has developed after patterning, reducing the zero-resistance critical temperature from 90 to 85 K. This film was patterned using an aqueous-base positive photoresist. A similar trend was seen in films patterned with a non-aqueous-base negative photoresist. The decrease in critical temperature was very significant for linewidths of <10 μm, which may be caused by nonuniformities in the film and/or chemical reactions at the exposed edges during photolithography.

The critical current density of a patterned 40-μm-wide YBa$_2$Cu$_3$O$_x$ film was measured to be 4×10^4 A/cm^2 and 2×10^3 A/cm^2 at 4.2 and 77 K, respectively. These values are comparable to critical current densities of bulk polycrystalline YBa$_2$Cu$_3$O$_x$.

M. Bhushan

6.2 RESIDUAL NOISE OF SUPERCONDUCTING NIOBIUM RESONATORS

We have previously[4] reported a preliminary measurement of residual noise of a niobium, superconducting stripline resonator. The measurement showed the expected 1/f dependence on offset frequency at frequencies close to the carrier. We have extended these measurements to include a number of resonators and have now measured the residual noise as a function of Q_L, the loaded Q.

65
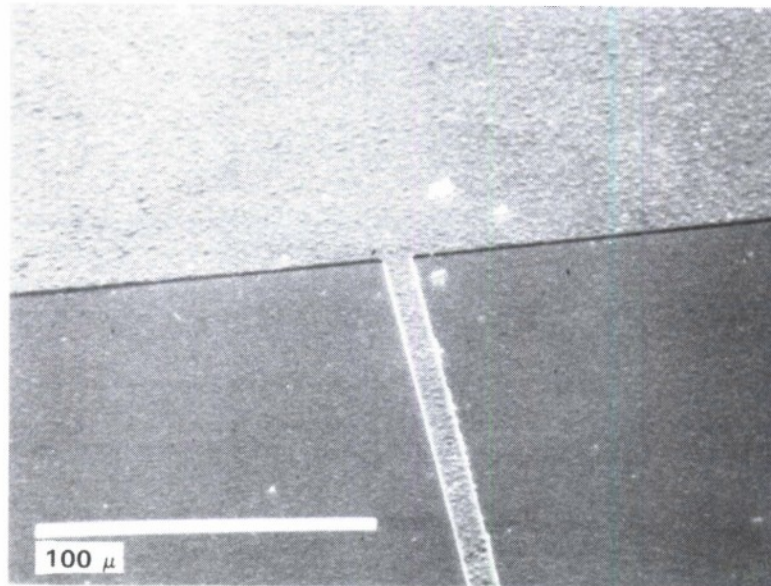
(a)
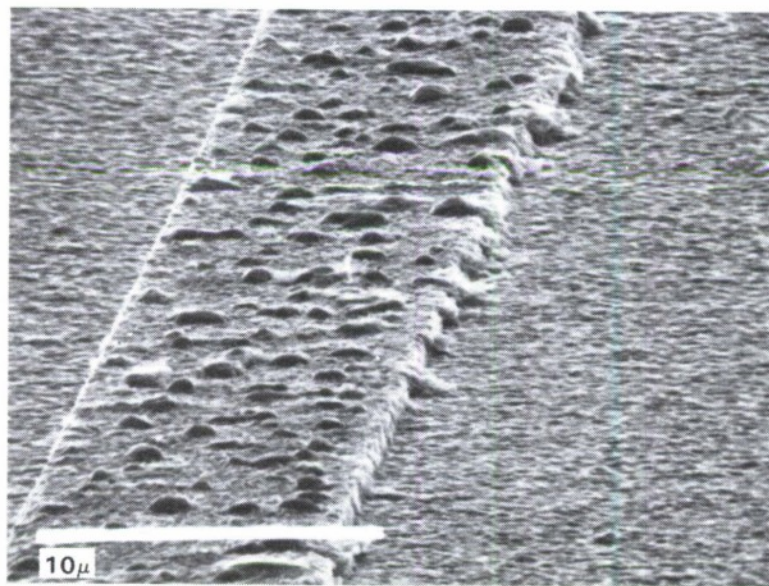
(b)

Figure 6-1. (a) Scanning electron micrograph of a 10-μm-wide patterned $YBa_2Cu_3O_x$ thin film; (b) close-up view of the line.
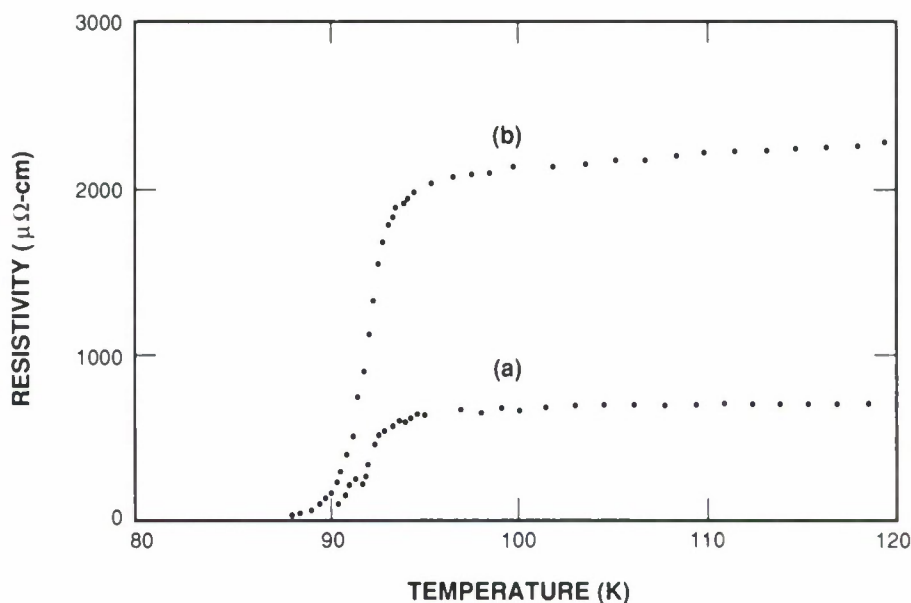
Figure 6-2.   Resistance vs temperature plot of a $YBa_2Cu_3O_x$ film (a) before and (b) after patterning.

The devices used are the same as those described in an earlier report.[4] The stripline structure is shown schematically in Figure 6-3. The substrates for these devices are silicon (p-type, 30 Ω-cm) and the conductors are deposited niobium. The resonator is made from an isolated length of stripline one-half wavelength ($\lambda/2$) long at the fundamental resonant frequency. The gaps in the stripline determine the coupling of the resonator to the external circuit, so that Q_L can be varied by changing the size of the gaps. Figure 6-4 shows an equivalent circuit for the resonator including the coupling gap which is modeled accurately as a series coupling capacitor. The fundamental resonant frequency of these devices is 1.1 GHz. The gap size has been varied from 150 to 500 μm. This range of gap sizes gives a Q_L which varies from 23,000 to 300,000. The largest Q_L is very close to the intrinsic Q for the niobium-on-silicon resonators. Table 6-1 summarizes the devices used in the measurements.

Measurements of the residual noise are shown in Figure 6-5. Plotted is the single-sideband phase noise £(f) in dBc/Hz as a function of the offset frequency from the carrier for each of the devices measured. The data exhibit the expected behavior for a resonator, namely, a flat region dominated by the system noise floor at large offset frequencies, joined to region of 1/f slope at small offset frequencies extending to <1 Hz. As can be seen from the data, the noise increases with increasing Q_L. The 1/f noise is often characterized by the value of the noise at 1 Hz offset from the carrier. This parameter, £(f = 1 Hz), is shown in Table 6-1 and is plotted vs Q_L in Figure 6-6.

A useful model of 1/f noise in acoustic resonators has been developed[5] which assumes that the source of the 1/f noise is fluctuations of the center frequency of the resonator. Let $S_{\Delta f}(f)$ and
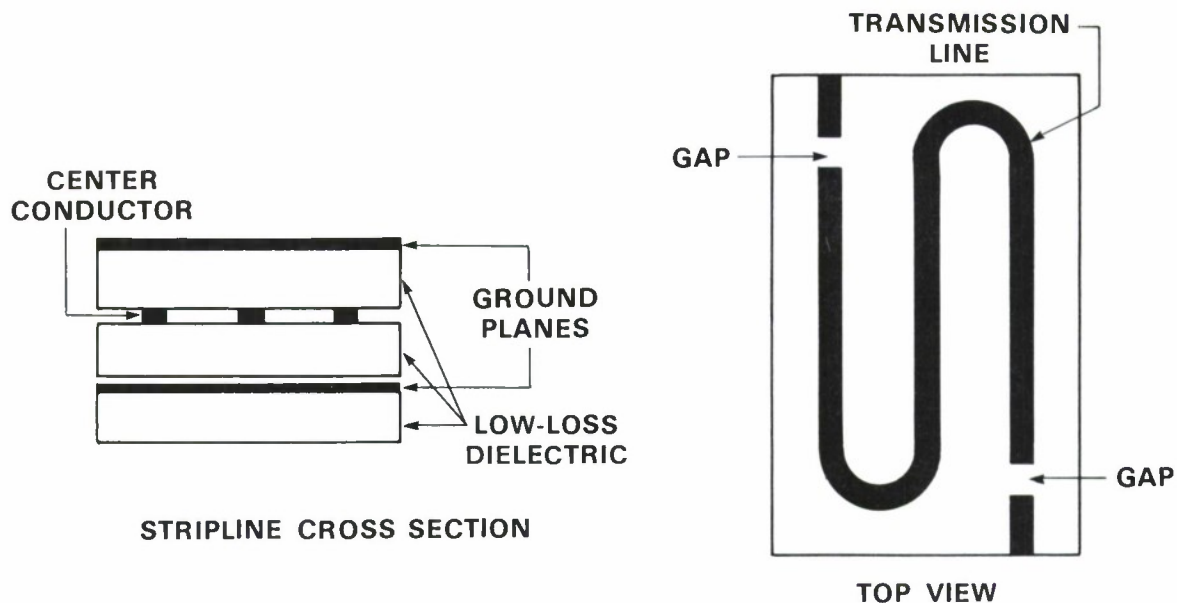
Figure 6-3. Schematic view of the stripline resonator. On the left is a cross section showing dielectrics and conductors. On the right is a top view of the center section showing the center conductor which has been patterned photolithographically. The gap shown determines the coupling to the resonant section of line.
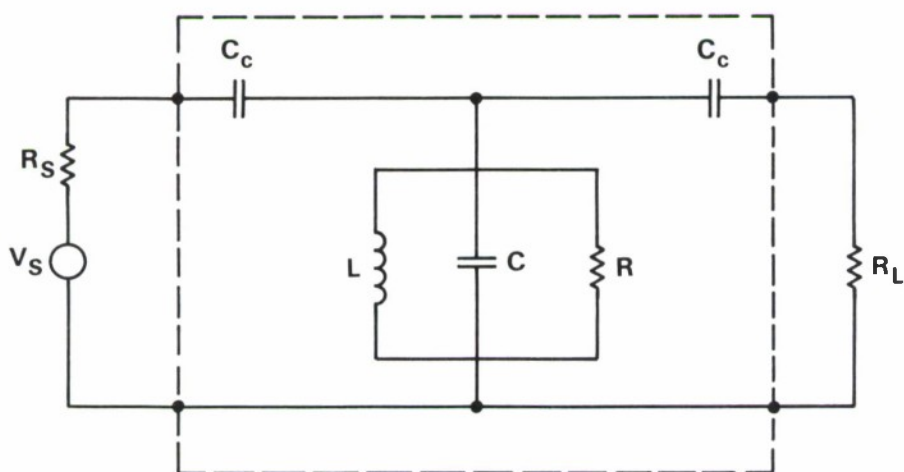
Figure 6-4. Equivalent circuit of the transmission-line resonator. R_s and R_L are source and load resistances. C_c represents the coupling capacitance and is determined by the gap shown in Figure 6-3.

68

TABLE 6-1		
Capacitive Coupling Gap, Loaded Q, and Residual Phase Noise of Niobium Resonators		
Gap (μm)	Q_L	$\pounds$ (f = 1 Hz) (dBc/Hz)
150	23,000	–120
300	80,000	–110
400	200,000	–100
500	250,000	–90

$S_\varphi(f)$ be the power spectral densities of center frequency and phase fluctuations, respectively. The Q_L of the resonator is related to the phase slope at center frequency f_o by

$$Q_L = \frac{1}{2} f_o \left. \frac{d\varphi(f)}{df} \right|_{f_o},$$ (6-1)

where $\varphi(f)$ is the phase response of the resonator vs frequency. If we assume that the center frequency of the resonator changes a small amount because of some small parametric change in the resonator (e.g., a temperature fluctuation which perturbs the dielectric constant of the substrate), and we assume that nothing else in the resonator changes, we can write

$$\Delta f_o = (f_o/2Q_L)\Delta\varphi.$$ (6-2)

Remembering that $S_{\Delta f}(f)$ and $S_\varphi(f)$ scale as the squares of the fluctuations $\Delta f_o(t)$ and $\Delta\varphi(t)$, respectively, we find that

$$S_\varphi(f) = (2Q_L/f_o)^2 S_{\Delta f}(f).$$ (6-3)

Thus, according to this model, 1/f noise should increase as the square of Q_L if $S_{\Delta f}$ is independent of Q, as is, for example, the power spectral density of the frequency fluctuations caused by temperature-dependent effects. The result derived in Equation (6-3) agrees well with our data, as can be seen in Figure 6-6.

The measured 1/f noise of these niobium resonators at 1-Hz offset from the carrier is larger than the measured values for good-quality surface-acoustic-wave resonators, which have a value of –130 dBc/Hz at 1-Hz offset.[6] The measured values are large enough to limit the performance of oscillators stabilized with these resonators. Sources of 1/f noise are being investigated. Temperature fluctuations, vibration sensitivity, and conduction processes in the film are possible causes.

One of the resonators which had been characterized in 1/f noise was used to stabilize an oscillator whose active circuitry was at room temperature. The phase noise of this oscillator was
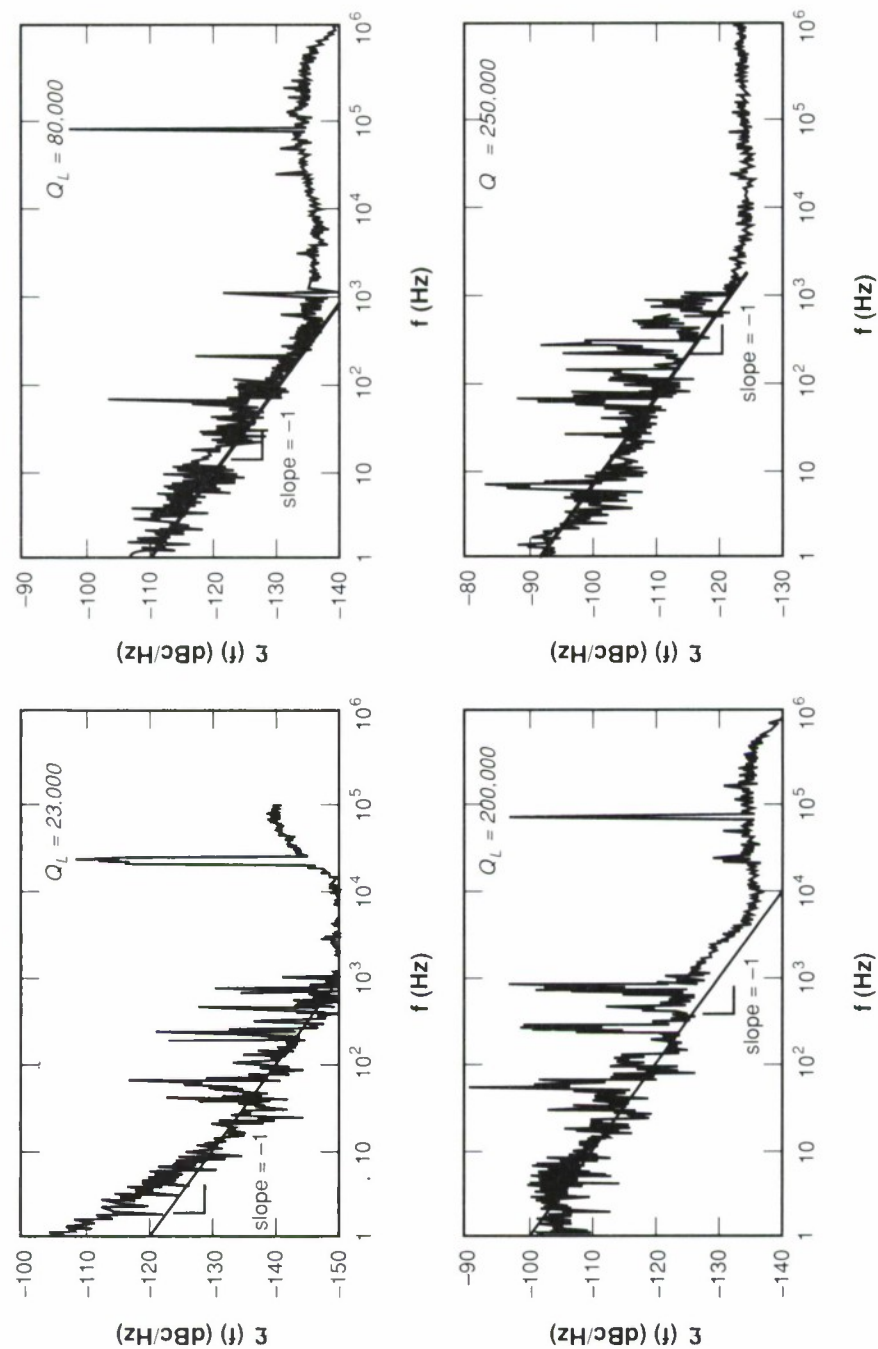
Figure 6-5. Set of four residual-noise measurements in Nb resonators with the indicated values of Q_L, the loaded Q. Plotted is £(f), the single-sideband phase noise, vs offset frequency from the carrier. At low offset frequencies, the noise follows the expected $1/f$ frequency dependence indicated by the straight lines.

70
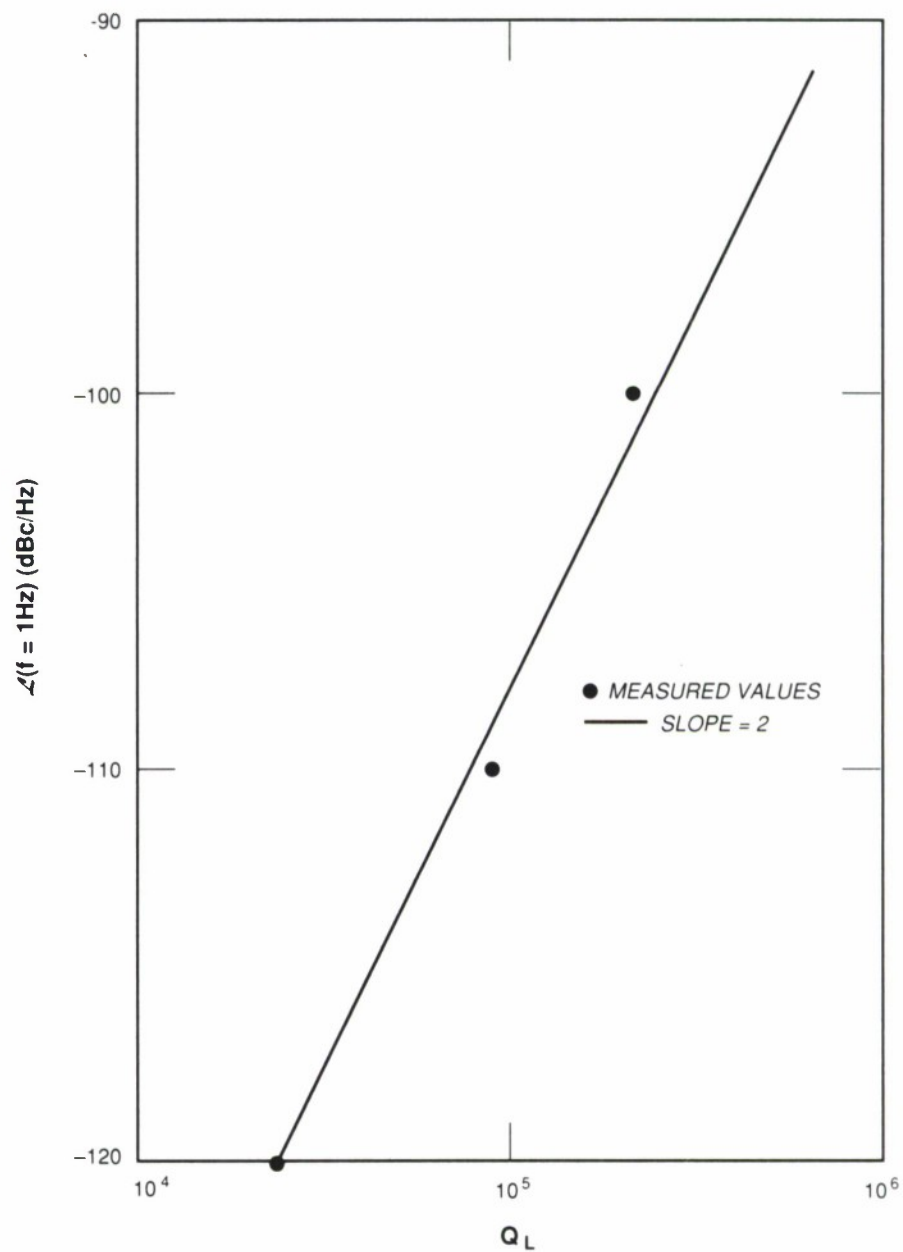
Figure 6-6. Plot of £(f) at 1-Hz offset frequency vs Q_L for the four resonators measured. Solid line of slope 2 corresponds to a Q_L^2 dependence.

measured using a commercial low-noise synthesizer as the reference oscillator. The results are shown in Figure 6-7. The calculated curve was derived from the standard Leeson model for the phase noise of feedback oscillators.[7] From this model, the single-sideband noise power in a 1-Hz bandwidth, relative to the carrier power, is given by

$$\pounds(\omega) = 10 \log \left\{ (1 + \omega_o^2/4Q^2\omega^2) \, (\alpha/\omega + GFkT/P_c) \right\}, \tag{6-4}$$

where $\pounds(\omega)$ is in dBc/Hz; P_c is the oscillator power; G is the loop gain; F is the amplifier noise figure; ω is the offset frequency in rad/s; Q is the resonator quality factor; ω_o is the oscillator center frequency; α is the flicker-noise constant, which must be empirically determined from the 1/f measurements; T is the absolute temperature; and k is Boltzmann's constant.

Equation (6-4) is plotted in Figure 6-7 for a Q of 80,000, G of 12 dB, F of 3 dB, P_c of 17 dBm, $\alpha = 1.6 \times 10^{-12}$, and an oscillator center frequency of 1.057 GHz to gain some insight into our measurements. As can be seen in the figure, the agreement for small offset frequencies is very good. At offset frequencies > 1 kHz, the noise of the synthesizer becomes larger than the noise of the superconducting-resonator-stabilized oscillator, and thus the measured phase noise reflects the phase noise of the synthesizer.

The superconducting resonator has not been designed for optimum phase noise performance. These measurements demonstrate that the resonator is well behaved and can be simply and effectively incorporated in an oscillator feedback loop as the stabilization element.

D.E. Oates
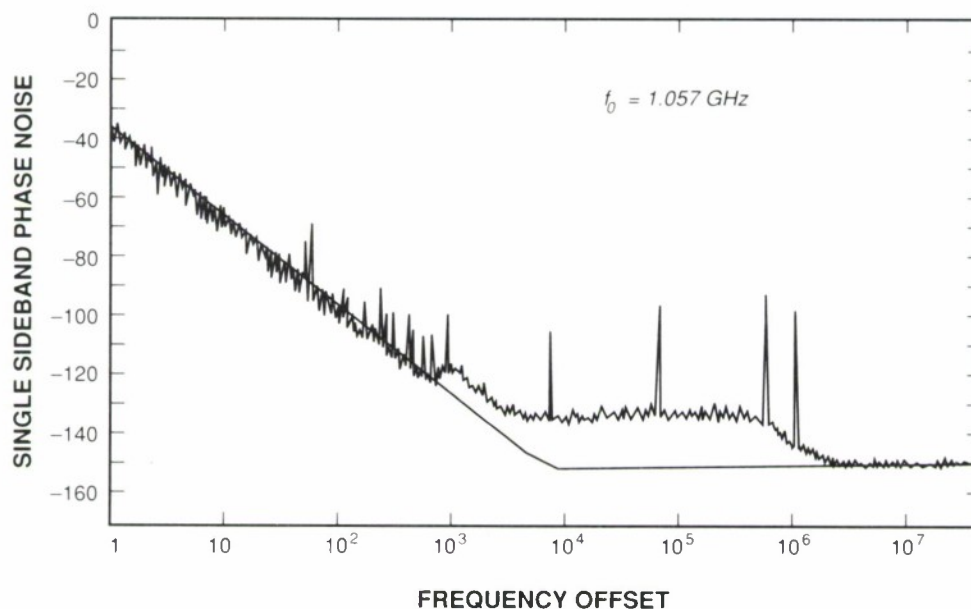
Figure 6-7. Measured phase noise of an oscillator stabilized with a superconducting resonator. The solid line is calculated from the Leeson model. See text for parameters used.

6.3 HIGH-SPEED ANALOG-TERNARY CCD CORRELATOR

A second generation of a four-channel analog-ternary correlator has been designed, fabricated, and tested. (Details of the first-generation device are contained in a previous report.[8]) A photomicrograph of the chip, designated the 4ABC-2, is shown in Figure 6-8. The high level of integration is evident in this figure. All required support circuitry is on chip, including clock drivers, track-and-hold circuits, buffer amplifiers, etc.

The design is based upon a self-contained, 64-sample, 32-tap cascadeable core block. With this approach chip layout is simplified, and future correlators, longer or shorter, can be rapidly implemented using the same basic building block.

A second iteration of this four-channel correlator was undertaken to improve linearity and output offsets for a critical application. The results of the modifications were extremely successful. Nonlinearity has been reduced to below –50 dB for a full-scale input signal. Since the distortion is dominated by the third harmonic, halving the input signal amplitude results in nonlinearities which are at least 60 dB below the fundamental. Similarly, output offset voltages have been reduced below 40 mV across all four channels. This maximum offset represents $<$ 2 percent of the output signal range and was achieved without resorting to on-chip trimming. At the same time, this second-generation device preserves the high dynamic range of the first version. Up to 10 Ms/s the dynamic range is 66 dB; thereafter it decreases slowly to 60 dB at 40 Ms/s.
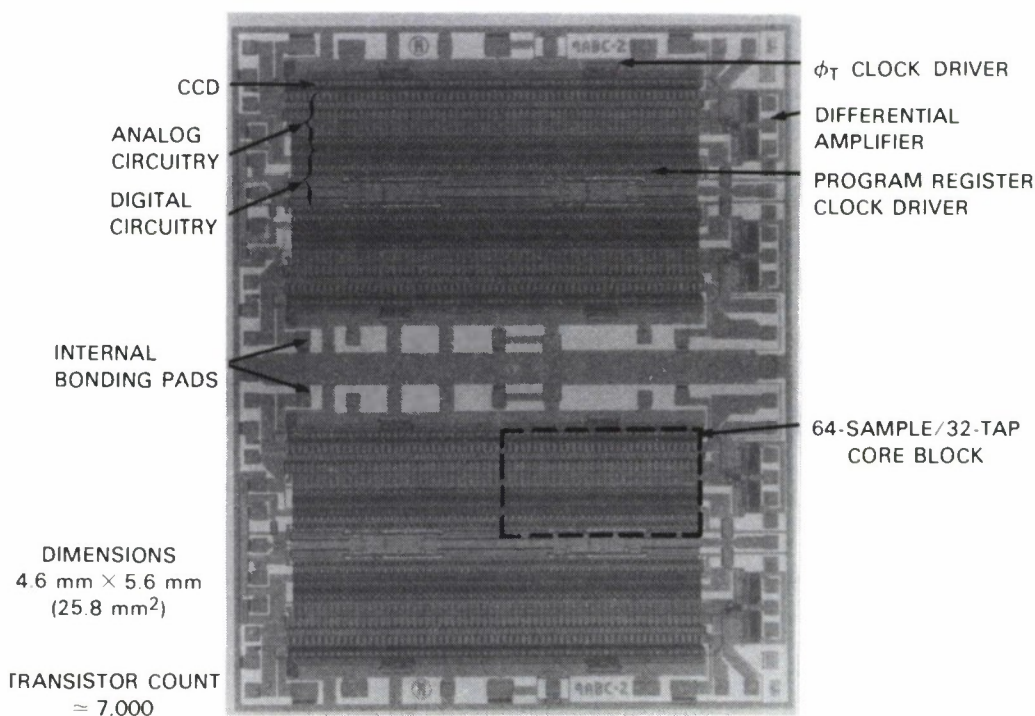

Figure 6-8. Photomicrograph of the 4ABC-2 second-generation four-channel analog-ternary correlator.

Figure 6-9 illustrates the performance of which this device is capable. It compares actual vs calculated device performance for the autocorrelation of a particular 63-bit aperiodic m-sequence. Note the extremely close agreement.

Additional evidence of excellent performance is shown in Figure 6-10. Here the 4ABC-2 is operated in a fast-in, slow-out mode (possible for codes no longer than half the maximum correlator length, because part of the correlator is required for buffer storage of the signal). The top traces are the input signals, which are read into the device at 20 times the readout rate. (The code structure in the high-speed burst is not visible on this time scale.) The bottom traces are the correlation outputs for the aperiodic inputs. The high linearity of the 4ABC-2 is evident in the case of the 8-cycle square wave, where the output approaches the textbook diamond-shaped envelope characteristic of the autocorrelation of a square wave pulse.

Figure 6-10 also illustrates a unique and very useful feature of the 4ABC-2: the output amplitude is independent of the code length. This characteristic, achieved by means of a constant-voltage summing network, eliminates the need to externally normalize outputs in systems in which code lengths change. It also maintains the large output dynamic range even for short codes.

Specifications for the 4ABC-2 correlator are given in Table 6-2. In every case except "channel gain matching," the design goals were exceeded.

S.C. Munroe
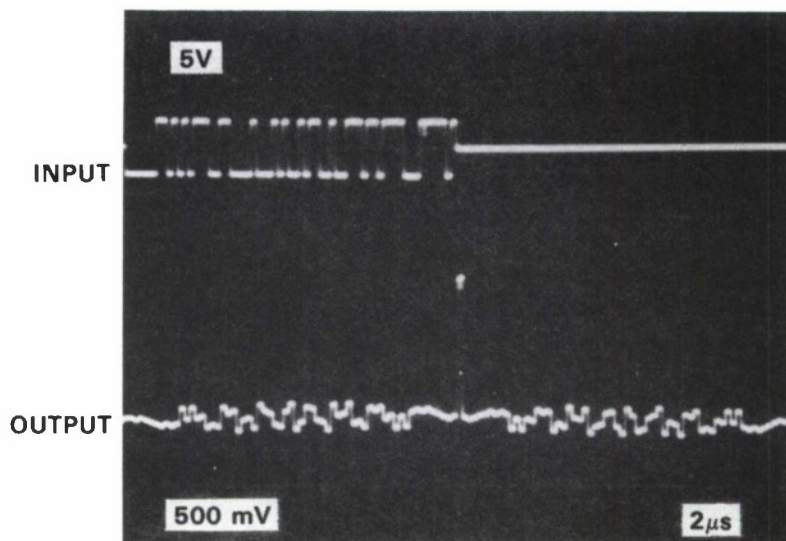
DEVICE PERFORMANCE
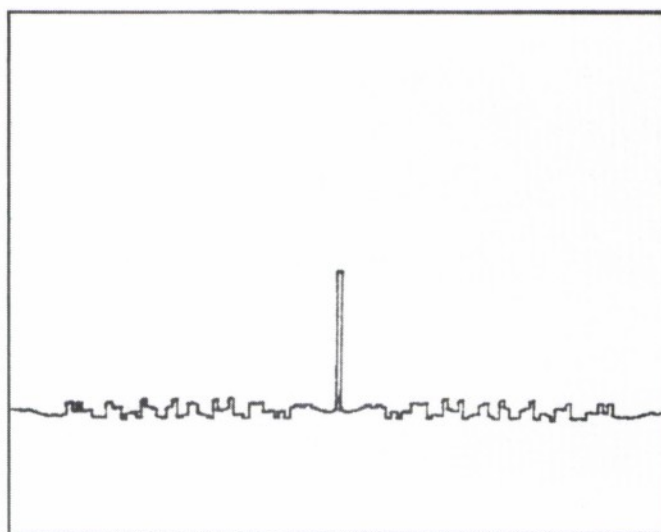
CALCULATED CORRELATION

Figure 6-9. Autocorrelation of an aperiodic 63-bit m-sequence by the 4ABC-2 correlator.
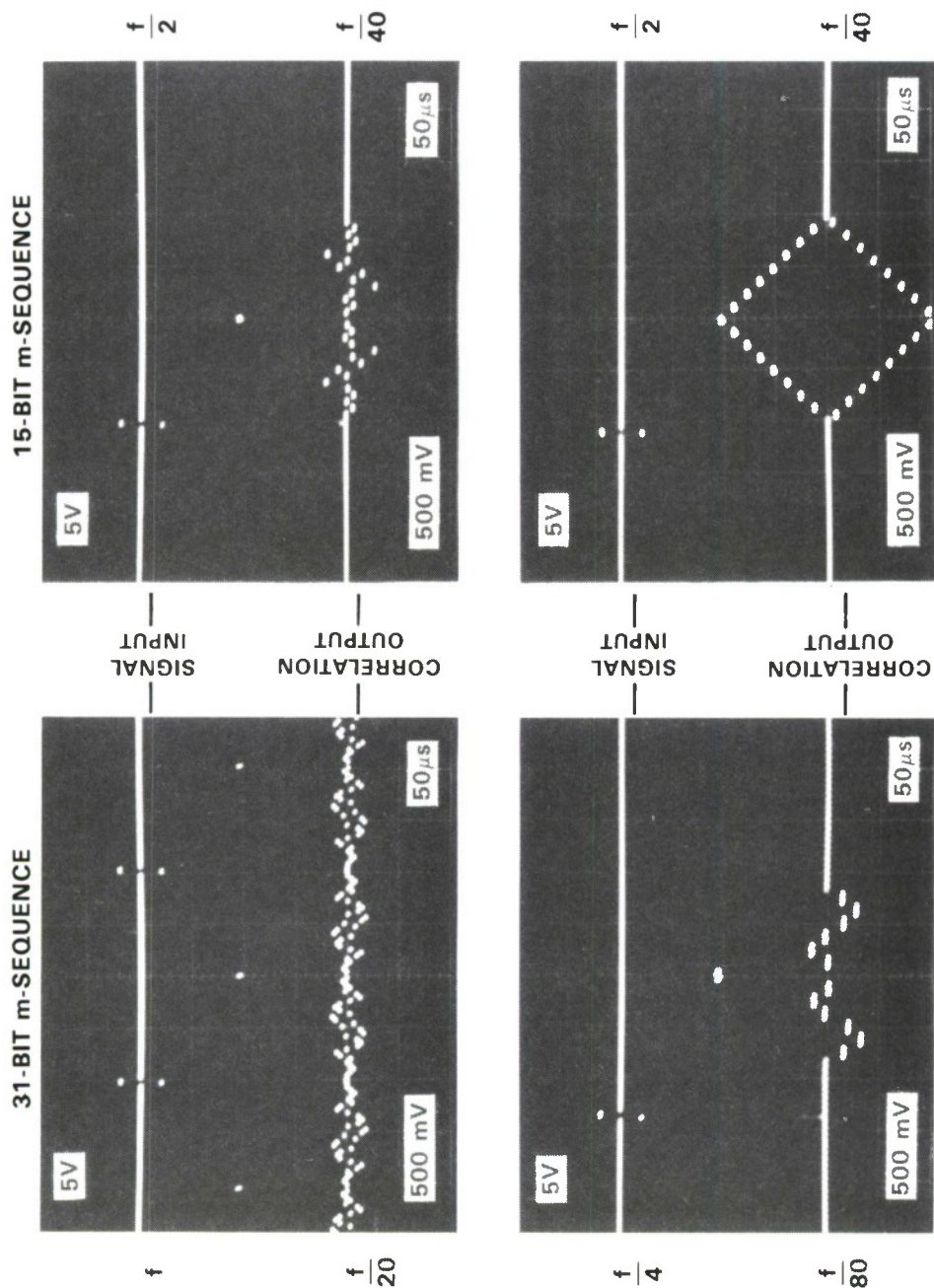
Figure 6-10. Correlation of aperiodic waveforms by the 4ABC-2 correlator in a fast-in/slow-out mode. The input signal (top trace) is captured at the frequency shown on the upper trace, stored in the forward half of the CCD cells, and then clocked by the reference code in the later half of the CCD at one-twentieth the capture frequency, thereby producing the outputs shown in the lower traces. The reference frequency is f = 12.5 MHz.

TABLE 6-2		
4ABC-2 CCD Correlator Specifications		
Parameter	Design Goal	Measured Performance
Max Sample Rate	15 Msps	40 Msps
Dynamic Range	$\geqslant$ 66 dB	66 dB ($<$ 10 Msps) 60 dB (40 Msps)
Channel Gain Matching	$\leqslant$ 3%	$\leqslant$ 5%
Nonlinearity	$\leqslant$ –46 dB	–50 dB at Full Scale (1.5 V_{pp})
Output Offset Voltage	$\leqslant$ 40 mV	$\leqslant$ 40 mV
Channel-to-Channel Isolation	$>$ 50 dB	$>$ 70 dB
Power Dissipation	$\leqslant$ 1 W	0.9-1.0 W
Max Programming Rate	15 MHz	$>$ 50 MHz

REFERENCES

1. Solid State Research Report, Lincoln Laboratory, MIT (1988:4), pp. 59-60.

2. J.W.C. de Vries, B. Dam, M.G.J. Heijman, G.M. Stollman, M.A.M. Gijs, C.W. Hagen, and R.P. Griessen, Appl. Phys. Lett. **52**, 1904 (1988).

3. S. Matsui, N. Takado, H. Tsuge, and K. Asakawa, Appl. Phys. Lett. **52**, 69 (1988).

4. Solid State Research Report, Lincoln Laboratory, MIT (1988:2), p. 60, DTIC AD-A204718.

5. T.E. Parker, *Proc. of the 41st Annual Symp. on Frequency Control* (IEEE, New York, 1987), p. 99.

6. M.J. Laboda, T.E. Parker, J.A. Greer, and G.K. Montress, 1987 *Ultrasonics Symp. Proc.* (IEEE, New York, 1987), p. 43.

7. D.B. Leeson, Proc. IEEE **54**, 329 (1966).

8. Solid State Research Report, Lincoln Laboratory, MIT (1988:1), p. 68, DTIC AD-A201044

REPORT DOCUMENTATION PAGE

1a. REPORT SECURITY CLASSIFICATION Unclassified			1b. RESTRICTIVE MARKINGS			
2a. SECURITY CLASSIFICATION AUTHORITY			3. DISTRIBUTION/AVAILABILITY OF REPORT Approved for public release; distribution is unlimited.			
2b. DECLASSIFICATION/DOWNGRADING SCHEDULE						
4. PERFORMING ORGANIZATION REPORT NUMBER(S) 1989:1			5. MONITORING ORGANIZATION REPORT NUMBER(S) ESD-TR-89-087			
6a. NAME OF PERFORMING ORGANIZATION Lincoln Laboratory, MIT	6b. OFFICE SYMBOL (If applicable)		7a. NAME OF MONITORING ORGANIZATION Electronic Systems Division			
6c. ADDRESS (City, State, and Zip Code) P.O. Box 73 Lexington, MA 02173-0073			7b. ADDRESS (City, State, and Zip Code) Hanscom AFB, MA 01731			
8a. NAME OF FUNDING/SPONSORING ORGANIZATION HQ AF Systems Command	8b. OFFICE SYMBOL (If applicable) AFSC/XTKT		9. PROCUREMENT INSTRUMENT IDENTIFICATION NUMBER F19628-85-C-0002			
8c. ADDRESS (City, State, and Zip Code) Andrews AFB Washington, DC 20334-5000			10. SOURCE OF FUNDING NUMBERS			

10. SOURCE OF FUNDING NUMBERS			
PROGRAM ELEMENT NO. 63250F	PROJECT NO. 221	TASK NO.	WORK UNIT ACCESSION NO.

11. TITLE (Include Security Classification)

Solid State Research

12. PERSONAL AUTHOR(S)
Alan L. McWhorter

13a. TYPE OF REPORT Quarterly Technical Report	13b. TIME COVERED FROM 1 Nov 88 TO 31 Jan 89	14. DATE OF REPORT (Year, Month, Day) 1989, February 15	15. PAGE COUNT 105

16. SUPPLEMENTARY NOTATION

None

17.	COSATI CODES		18. SUBJECT TERMS (Continue on reverse if necessary and identify by block number)
FIELD	GROUP	SUB-GROUP	electrooptical devices · analog device technology · integrated circuit repair quantum electronics · lasers · microwave semiconductor materials research · optical modulators · devices submicrometer technology · infrared detectors · superconductors microelectronics · dry resist · charge-coupled devices

19. ABSTRACT (Continue on reverse if necessary and identify by block number)

This report covers in detail the research work of the Solid State Division at Lincoln Laboratory for the period 1 November 1988 through 31 January 1989. The topics covered are Electrooptical Devices, Quantum Electronics, Materials Research, Submicrometer Technology, Microelectronics, and Analog Device Technology. Funding is provided primarily by the Air Force, with additional support provided by the Army, DARPA, Navy, SDIO, NASA, and DOE.

20. DISTRIBUTION/AVAILABILITY OF ABSTRACT ☐ UNCLASSIFIED/UNLIMITED ☒ SAME AS RPT. ☐ DTIC USERS	21. ABSTRACT SECURITY CLASSIFICATION Unclassified	
22a. NAME OF RESPONSIBLE INDIVIDUAL Lt. Col. Hugh L. Southall, USAF	22b. TELEPHONE (Include Area Code) (617) 981-2330	22c. OFFICE SYMBOL ESD/TML

DD FORM 1473, 84 MAR   83 APR edition may be used until exhausted.   UNCLASSIFIED
                              All other editions are obsolete.

SECURITY CLASSIFICATION OF THIS PAGE